HERON is jointly edited by:
STEVIN-LABORATORY of the department of Civil Engineering, Delft University of Technology, Delft, The Netherlands
and
TNO-INSTITUTE FOR BUILDING MATERIALS AND STRUCTURES.
Rijswijk (ZH), The Netherlands.
HERON contains contributions based mainly on research work performed in these laboratories on strength of materials, structures and materials science.

ISSN 0046-7316



HERON vol. 32 1987 no.3

**Contents**

# EXAMPLES OF NON-LINEAR ANALYSIS OF REINFORCED CONCRETE STRUCTURES WITH DIANA

*J. G. M. van Mier*
Stevin Laboratory
Department of Civil Engineering
Delft University of Technology
Delft, The Netherlands



CUR

*This publication has been issued in close co-operation with the Centre for Civil Engineering Research, Codes and Specifications*

# EXAMPLES OF NON-LINEAR ANALYSIS OF REINFORCED CONCRETE STRUCTURES WITH DIANA*

## Preface

Under the Marine Technological Research (MaTS) of the Industrial Council for Oceanology (IRO), an extensive research program on Concrete Mechanics has been carried out. This research was guided by CUR-Committee A 26 "Concrete Mechanics", of which the present constitution is as follows: Prof. Ir. B. W. van der Vlugt (chairman), Ir. A. W. F. Reij (secretary), Prof. Dr. Ir. J. Blaauwendraad, Prof. Ir. A. L. Bouma, Prof. Dr. Ir. A. S. G. Bruggeling, Dr. Ir. H. J. Grootenboer, Prof. Ir. J. W. Kamerling, Ir. G. M. A. Kusters, Prof. Ir. H. Lambotte, Prof. Dr.-Ing. G. Mehlhorn, Ir. Th. Monnier, Prof. Dr.-Ing. H. W. Reinhardt, Prof. Ir. J. Witteveen, Prof. Dr. F. H. Wittmann (corresponding member), Ir. H. P. J. Vereijken (coordinator CUR), Ir. H. A. van Dijk (mentor).

In 1986, Ir. H. A. van Dijk and Ir. H. P. J. Vereijken succeeded respectively Ir. W. Stevelink and Ing. A. C. van Riel.
The main purpose of this study is to narrow the gap between consulting engineers and the researchers, who are responsible for the development of the numerical program and the underlying material models. In the present report, eight examples of non-linear analysis of reinforced concrete structures with the finite element package DIANA are discussed.
This study has been directed by a working group, in which the following persons contributed: Ir. J. Saveur (chairman), Prof. Dr. Ir. J. Blaauwendraad, Prof. Dr. Ir. A. S. G. Bruggeling, Ir. F. F. M. de Graaf, Ir. G. M. A. Kusters, Ir. S. E. van Manen, Ir. Th. Monnier, Ir. B. J. G. van der Pot, Ir. A. W. F. Reij, Prof. Dr.-Ing. H. W. Reinhardt and Ing. A. C. van Riel.
The analyses were all carried out at the Institute TNO for Building Materials and Structures (TNO-IBBC) by, Ir. C. R. Braam (example 6), Ir. H. Groeneveld (example 7), Ir. J. F. Marcelis (examples 2, 3 and 5b), Prof. Chr. Meyer (example 8), Dr. Ir. J. G. M. van Mier (examples 1, 5a), Ir. J. G. Rots (example 4).
The relevant chapters in this report have been written by the same persons. Dr. Van Mier wrote the introductory and final chapters, and acted as general Editor. Prof. Meyer made his contribution during his sabatical leave from Columbia University, NY, USA.
Financial support was provided by the Ministry of Economic Affairs, Rijkswaterstaat (a division of the Ministry of Transport and Public Works), TNO-IBBC and the CUR (Centre for Civil Engineering, Research, Codes and Specifications).
This report is based on CUR/IRO/MaTS report 134 "Betonmechanica - Voorbeelden van Niet-Lineaire Berekening met DIANA".

August 1987

Prof. Ir. B. W. van der Vlugt
Chairman of the CUR Committee A 26
"Concrete Mechanics"

---

* DIANA is a trade mark of TNO-IBBC.

# Examples of non-linear analysis of reinforced concrete structures with DIANA

## 0 Introduction

### 0.1 *General*

The Netherlands Concrete Mechanics project is an on-going cooperative research program between the Technical Universities of Delft and Eindhoven, the Rijkswaterstaat, a division of the Netherlands Ministry of Transport and Public Works, and the Institute for Applied Scientific Research on Building Materials and Structures (TNO-IBBC). The first phase of the project, which ended in 1981, was subdivided into four sub-projects as indicated in Fig. 0.1. Sub-projects 1, 2 and 4 are related to modelling of the material behaviour: concrete cracking, bond-slip behaviour between reinforcement and concrete, and aggregate interlock (i.e. stress transfer in cracks). This investigation was carried out by "materials scientists", and the results served as input for sub-project 3, global models. The global models were developed by specialists in numerical modelling and applied mechanics, and are used for describing the global (overall) behaviour of (reinforced) concrete structures.

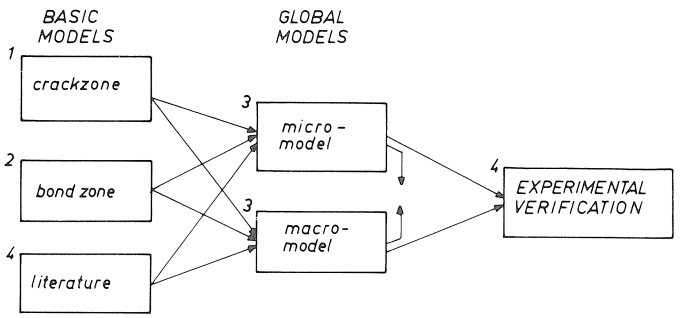


Fig. 0.1. Concrete Mechanics Project.

The basic principle of the "concrete mechanics project" is to analyse structural behaviour of reinforced concrete members by "adding up" effects from cracking, bond-slip behaviour and aggregate interlock into a numerical scheme which accounts for the geometry of the structure under consideration. The first phase, mentioned above, was concerned mainly with the development of material models for use in numerical models with the restriction of short-term (static) loading. In the second phase, which is in progress at present, emphasis is placed on off-shore applications (cyclic and sustained loading).

Three numerical models have been developed: DIANA, a general-purpose finite element code for the analysis of three-dimensional structures taking into account physical nonlinear material behaviour (De Borst et al. 1983), MICRO, a numerical model suitable for analysing two-dimensional and axi-symmetrical structures (Grootenboer 1979), and MACRO, a two-dimensional beam model (Grootenboer et al. 1981).
In the present report, eight examples of non-linear numerical analysis of reinforced concrete structures with DIANA are shown. The examples include the simulation of three construction details (tooth structure of the metro viaduct in Rotterdam, a corbel and a beam-column connection), three global structures (a reinforced concrete panel (subdivided in two variants, a single-span deep beam and a panel on three supports), a numerical simulation of a tunnel section, and an analysis of an LNG tank subjected to a "fire load"), and two dynamic analyses (viz. a beam falling on a shock absorbing element, and a numerical simulation of an explosion in a tunnel). All simulations are two-dimensional except for the simulation of the LNG tank, which is treated as an axi-symmetric problem. Several types of loads are considered, i.e. static loading, fire loading, and dynamic loading. A general introduction on modelling with DIANA is given in this chapter. Typical problems encountered in the analysis for a certain problem are discussed separately for that particular example.
In general a choice has to be made as to whether for solving a complex structural problem an experimental model study is required or whether a non-linear finite element analysis will suffice. The examples have been chosen in order to demonstrate the current possibilities of numerical analysis of reinforced concrete structures. The numerical simulation technique seems to be applicable in certain practical situations, but it should be mentioned that the analyses should be carried out by experienced engineers who are familiar with the programs and the underlying material models. Furthermore, also for research purposes, the numerical models provide a new and powerful instrument, which, in combination with experiments, may lead to a better understanding of the behaviour of reinforced concrete structures.

## 0.2 *Modelling with DIANA*

### 0.2.1 General

In a numerical analysis based on finite elements, a structure is divided into a large number of "elements", which are interconnected by nodes. The nodes are generally situated in the corners, but also may appear along the edges (Fig. 0.2). Loads and supports are specified, and for the system a set of equilibrium and compatibility equations is set up, which can be solved numerically. Several numerical solution techniques are available in DIANA, and have been treated extensively by De Borst 1986.
Results are given at so-called integration points, which do not coincide with the nodes. The element shown in Fig. 0.2 is an eight-noded quadratic iso-parametric (i.e. with curved boundaries) element with nine-point (Gaussian) numerical integration. This element has been used in several examples that appear in this report.

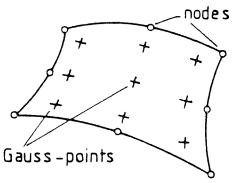


Fig. 0.2. Eight-noded isoparametric element for plane stress analysis.

Material properties are defined for these "concrete" elements, and in contrast to a linear elastic analysis, where only the Young's modulus $E$ and the Poisson's ratio $\nu$ have to be specified, a non-linear analysis will require knowledge of several more parameters. These parameters and the related material models are discussed shortly in the next section. The parameters used in the examples are summarized in four tables.
Reinforcement is modelled as bar elements and the stiffness of the reinforcement is simply added to the stiffness of the elements in which the bar is "embedded". When full bond between reinforcement and concrete is assumed, the reinforcement may be contained within a "concrete" element. In this case, the nodes of the reinforcing bar do not necessarily coincide with the nodes of the concrete elements. In contrast, when bond-slip between reinforcement and concrete is modelled, special interface elements are used which are placed between the "bar-nodes" and the "concrete-nodes".

## 0.2.2 Material models in DIANA

The material models that are available in DIANA, and are used in the examples, are discussed in the following sections. The behaviour of the "material" concrete is modelled by means of two models: a crack model which is valid for loading combinations in which at least one tensile component is involved, and a plasticity model for describing the behaviour of concrete under (multiaxial) compressive stress states. The crack model is based on a strength criterion, and is valid also in the tension-compression regions. The crack model is discussed in Section 0.2.2.1 for the special case of direct tension. In Section 0.2.2.2 attention is paid to the plasticity model and the strength criteria for failure in compression and tension.
For the reinforcing steel a plasticity model is used, which is described shortly in Section 0.2.2.3. The model for bond-slip (by means of interface elements between the concrete and the steel reinforcement) is discussed in Section 0.2.2.4.

### 0.2.2.1 Crack model for concrete in tension

*Direct tension*
In Fig. 0.3, a stress-displacement diagram obtained from a direct tension test on a plain concrete plate is shown.
In a stable displacement controlled experiment it is possible to measure the residual strength of the specimen after the peak stress has been exceeded (e.g. Reinhardt 1984).

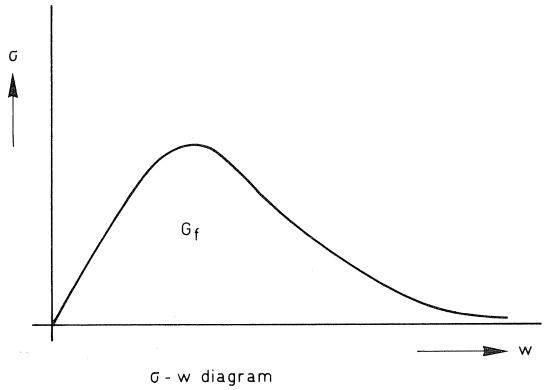


Fig. 0.3. Stress-displacement (crack width) diagram for plain concrete in direct tension.

While only a single macrocrack develops through the specimen it is customary to define the results in terms of a stress-displacement (crack width) diagram. The falling branch beyond the peak is called the softening branch, and the surface under the stress-crack width diagram is the amount of energy needed for fracturing the specimen, and is called the fracture energy $G_f$.
In DIANA, a smeared crack concept is used and the stress-crack width diagram has to be translated into a stress-crack strain diagram. In this case, a certain length over which the crack is smeared out, i.e. the crack band width has to be defined.
When a non-linear analysis of an *unreinforced* concrete structure is carried out, the $G_f$ concept is used, and the stress-crack strain diagram is schematized to a bilinear diagram (Fig. 0.4). The value for $\varepsilon_u$ for this linear softening case can be calculated using

$$\varepsilon_u = 2 \frac{G_f}{f_{ct} h} \tag{1}$$

In this equation, $h$ is the crack band width, i.e. the width over which the crack is smeared out, and in an analysis this is usually taken as the size of a typical element. This implies that for estimating $h$, one should have a rough idea of the direction in which the tensile crack will propagate.
It should be mentioned that in the analysis, the tensile strength is used as a criterion for crack initiation; the $G_f$ concept is used to describe crack propagation. For more information regarding this subject, refer to Rots et al. 1985.
The $G_f$ concept is useful for analyzing those structures in which the structural behaviour is determined completely by the behaviour of a single macrocrack. If this is not the case, for example when many closely spaced cracks develop due to the presence of a dense net of steel reinforcement, the average effect of all cracks is taken into account via the so-called "tension stiffening" concept.
Of course one might decide to use the $G_f$ concept in combination with the bond slip interface elements (Section 0.2.2.3) for the analysis of a *reinforced* concrete structure, but this will generally lead to an exceedingly large number of elements. Such an ana-

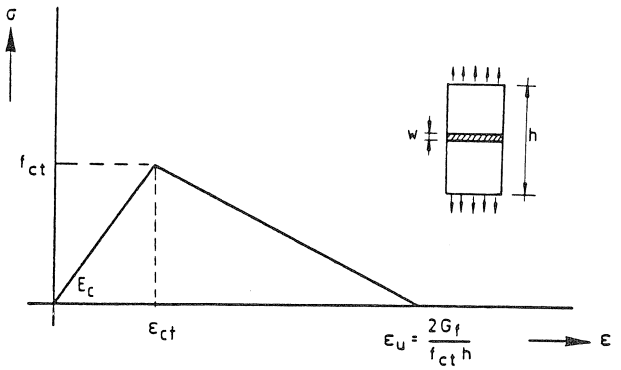


Fig. 0.4. Linear softening model.

lysis will require a vast amount of computer capacity, and does not seem very realistic at present. Only in cases where a considerable influence of bond slip is expected might one decide to use the interface elements, but only when the element-mesh does not become too large.

As already mentioned, when a *reinforced* concrete structure is analyzed, the tension stiffening concept is used. The principle is explained in Fig. 0.5. Due to stress-transfer between cracks in a reinforced member, a higher "stiffness" of this member is observed as compared with the behaviour of the reinforcement only. An estimate for the maximum tensile strain is derived from the yield-strain of the reinforcement

$$\varepsilon_s = \varepsilon_{us} = \frac{f_{sy}}{E_s} \tag{2}$$

where $f_{sy}$ is the yield stress of the reinforcing steel, and $E_s$ is Young's modulus of the steel. The tension-stiffening concept is applicable for the analysis of a reinforced concrete structure with uniform distributed reinforcing bars, and when cracks are expected to develop perpendicular to the direction of the bars.

This is a rather severe restriction: in general cracks do not intersect the reinforcement perpendicularly, but more likely under a certain angle. Also, the assumption of uniformly distributed reinforcing bars generally does not apply in structures. Note that average steel stresses are computed, not the maximum steel stresses that occur in the cracks. This is a direct consequence of the smeared crack approach.

Several factors will affect the rate of macrocrack growth in a reinforced concrete structure: spacing of reinforcing bars, diameter of reinforcing bars, angle between the bars and the macrocrack, etc. The multitude of these factors makes it rather difficult to give a "watertight" method of determining $\varepsilon_{us}$, but in general the value obtained from equation (2) has to be adjusted. However, the magnitude of the correction factor has to be estimated, usually by means of a parameter study. Estimating the value of the reduction factor will be easier for experienced engineers, who are familiar with these types of analysis.

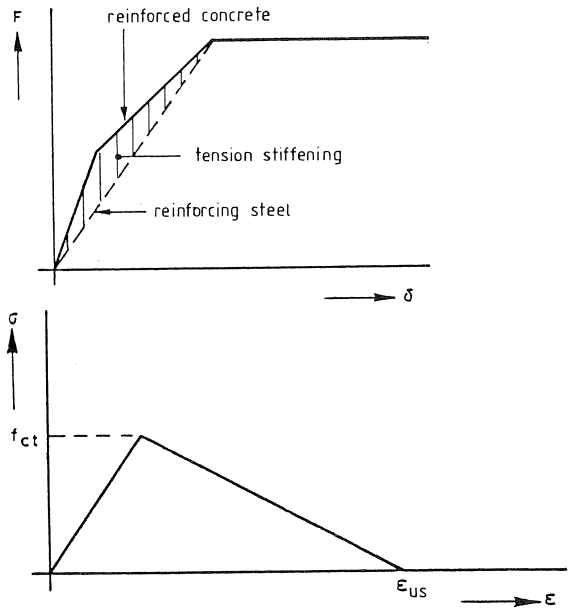


Fig. 0.5. Tension stiffening concept for reinforced concrete.

*Shear transfer in cracks*

Another input parameter related to concrete cracking is the shear retention factor $\beta$, which takes into account a reduction of the shear stress that can be transferred through cracked concrete. In Fig. 0.6, this so-called aggregate interlock mechanism is explained. For *unreinforced* concrete, and for *reinforced* concrete, $\beta = 0.20$ will lead to appropriate results in most cases. This value is based on experience. A more theoretical background is currently being developed. The parameters for modelling tensile cracking in concrete are summarized in Table 0.1.

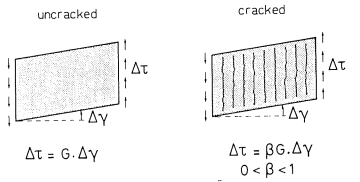


Fig. 0.6. Reduction factor $\beta$ for modelling aggregate interlock.

Table 0.1 Parameters for modelling tensile cracking

| unreinforced concrete (direct tension) | | reinforced concrete | |
|---|---|---|---|
| fracture energy $G_f$ | 60 N/m | tension stiffening $\varepsilon_{us}$ | $f_{sy}/E_s$ |
| tensile strength $f_{ct}$ | problem related | shear retention factor $\beta$ | 0.20 |
| crack band width $h$ | depends on the element mesh | | |
| shear retention factor $\beta$ | 0.20 | | |

0.2.2.2 Plasticity model for concrete in compression

An elasto-plastic model is used for modelling the behaviour of concrete in compression (Fig. 0.7). The uniaxial compressive stress-strain curve is characterized by Young's modulus $E_c$ and the uniaxial compressive cylinder strength $f_{cc}$. It should be mentioned that also a non-linear variant is available. Recently, the model was extended in order to take into account softening of concrete in compression (Vermeer and De Borst 1984).

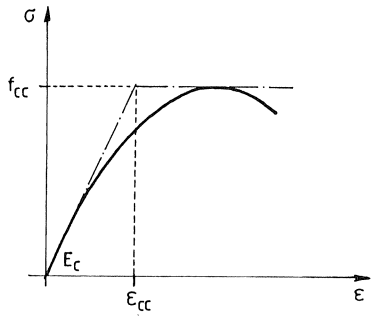


Fig. 0.7. Elasto-plastic stress-strain relation for concrete in compression.

In all the examples the Mohr-Coulomb yield criterion is applied for taking account of multiaxial states of stress. A cross-section of this criterion with the biaxial principal stress plane is shown in Fig. 0.8. The criterion is characterized by the angle of internal friction $\varphi$ and cohesion $c$. By choosing $\varphi = 30°$, the fit between the Mohr-Coulomb criterion for stress combinations $\sigma_1 < \sigma_2 = \sigma_3 < 0$ (i.e. stress-combinations in the triaxial compressive region, compressive stresses are negative), is satisfactory. The cohesion $c$ depends on the uniaxial cylinder strength $f_{cc}$ in accordance with

$$c = \frac{f_{cc}(1 - \sin \varphi)}{2 \cos \varphi} \tag{3}$$

The Mohr-Coulomb criterion considerably underestimates the strength of concrete under biaxial ($\sigma_1 \neq \sigma_2 < 0$, see Nelissen 1972) and triaxial compression ($\sigma_1 \neq \sigma_2 \neq \sigma_3 < 0$, see Van Mier 1984). Yet, the results obtained with the model are generally a safe lower bound, but may lead in some of the examples to discrepancies between the numerical and experimental results.
When the above values for $\varphi$ and $c$ are used, the tensile strength of the material is overestimated. Therefore, but also for optimizing the fit between experimental results and the Mohr-Coulomb model, several "tension cut-off" criteria are available. Two of these "tension cut-off" criteria that are used in the examples are shown in Fig. 0.8. Note that the fit between the Mohr-Coulomb criterion and experiments in the tension-compression regions also may be obtained by choosing a higher value of $\varphi$. However, the tension cut-off criteria are needed also for deciding when the crack model should be used (see previous section for uniaxial tension).

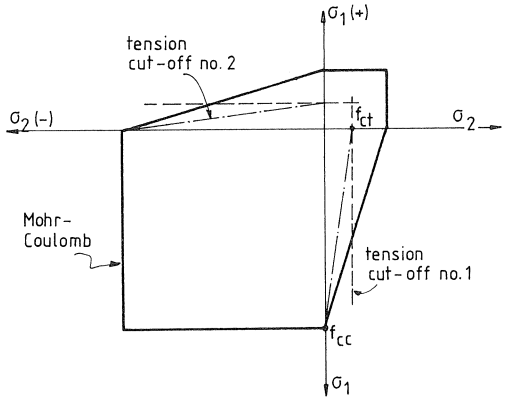


Fig. 0.8. Mohr-Coulomb yield criterion with "tension cut-off" in the biaxial principal stress plane.

Table 0.2 Parameters for the concrete plasticity model

| compression | |
|---|---|
| yield criterion | Mohr-Coulomb |
| internal friction angle $\varphi$ | 30° |
| cohesion $c$ | problem related |
| tension cut-off criterion | Fig. 0.8 |
| uniaxial compressive strength $f_{cc}$ | problem related |
| Young's modulus $E_c$ | problem related |

The parameters needed for modelling the compressive behaviour of concrete are summarized in Table 0.2.

### 0.2.2.3 Plasticity model for the reinforcing steel

For the reinforcement an elasto-plastic model can also be adopted (Fig. 0.9). The two parameters that must be defined are shown in Table 0.3.

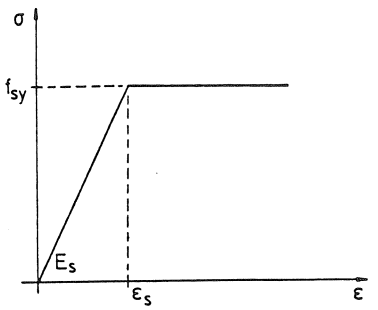


Fig. 0.9. Elasto-plastic stress-strain relation for the reinforcing steel.

Table 0.3 Parameters for the reinforcing steel

| reinforcing steel | |
|---|---|
| yield stress $f_{sy}$ | problem related |
| Young's modulus $E_s$ | problem related |

### 0.2.2.4 Bond between steel and concrete

As was mentioned in the general introduction to this chapter, bond between steel and concrete can be modelled using two different approaches.
If full bond between steel and concrete is assumed, the reinforcement is modelled by bar elements which are "embedded" in the concrete elements.
However, if relative displacements between reinforcing steel and concrete are allowed, special slip elements (two-dimensional springs) can be placed between the bar elements that represent the reinforcing steel and the concrete elements (see Fig. 0.10). The consequence of this approach is that the element mesh must be adjusted to the "reinforcement grid", and when numerous reinforcement bars are present in a structure, this may lead to an exceedingly large number of elements. It is very important to decide at an early stage if a detailed analysis, taking bond-slip into account, is needed.
The behaviour of the slip elements is described by means of two constitutive equations. The first relates the bond shear stress $\tau_z$ to the slip $\Delta u$ along the bar, the second relation describes the relation between the radial component of the bond stress $\tau_r$ and the radial displacement $\Delta v$. The first relationship $(\tau_z - \Delta u)$ is conceived as a bi-linear diagram. The stiffness of the first branch is defined by the slip modulus $S^z$. The radial relation $\tau_r - \Delta v$ is assumed to be linear with stiffness $S^r$. The $\tau_r - \Delta v$ becomes important when radial confinement is present. In the current examples this factor is not taken into account, only the axial component $\tau_z - \Delta u$ is used. For details regarding the bond-slip

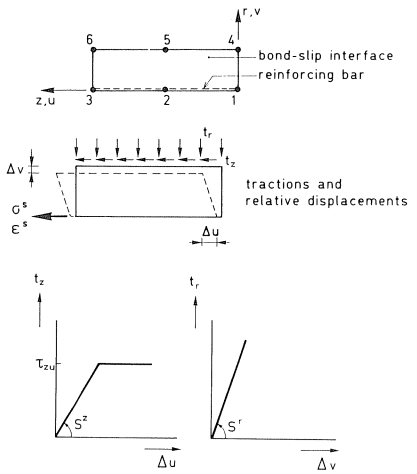


Fig. 0.10. Slip element and assumed stiffness relations.

model the reader is referred to (De Groot et al. 1981, and Rots 1985). The parameters used in the current examples are summarized in Table 0.4. Two parameters are important, namely, the slip modulus $S^z$ and the maximum bond shear stress $\tau_{zu}$. The value for these parameters are taken from (De Groot et al. 1981).

Table 0.4 Parameters for modelling bond-slip

| bond-slip | |
|---|---|
| slip modulus $S^z$ | 200 N/mm$^3$ |
| maximum bond stress $\tau_{zu}$ | 5 N/mm$^2$ |

## 0.3 *Graphical representation of the results*

The results of the analyses are discussed in the following chapters (1–8). In all the examples the graphical facilities of DIANA are used. In general, a load-displacement diagram of the analysis is compared with the experimental results (if available). As mentioned before, principal stresses, cracks, etc. are represented at the integration points. The symbols used are listed below.

- When *(principal) stresses* are shown, solid lines refer to tensile stresses, whereas dotted lines refer to compressive stresses. The direction of the line segments for the stresses represents the direction in which the particular stress component is acting; the length of the line segment is an indication of the "intensity".
- *Cracks* are shown as line segments. In most cases only the contours of the element mesh, or a part of the element mesh, are shown. In some of the analyses, only those cracks, with a "crack strain" exceeding a certain value are shown. This is always mentioned, for example cracks with "crack strains" greater than $\varepsilon_u$ may be plotted, which are then referred to as "open cracks".
- Either *total deformations* or *incremental deformations* are shown. The incremental deformations are the deformations that occur in the preceding load-step only. Because deformations are generally quite small in comparison with the dimensions of the element mesh, they are shown on a larger scale. The multiplication factor may be specified, but in most cases the largest possible magnification is chosen and no value is mentioned.
- *Plasticity,* either in concrete (in compression) or in the reinforcing steel, is visualized by means of small triangles at the integration points. The relative size of the triangle is a measure of the plastic strain.

Finally it should be mentioned that each example has its specific problems which may require a special presentation.

# 1 Metro viaduct Rotterdam

## 1.1 *Introduction*

In 1965, the structural behaviour of a beam of the metro viaduct in Rotterdam was determined in a full-scale experiment. In this experiment attention was given to the

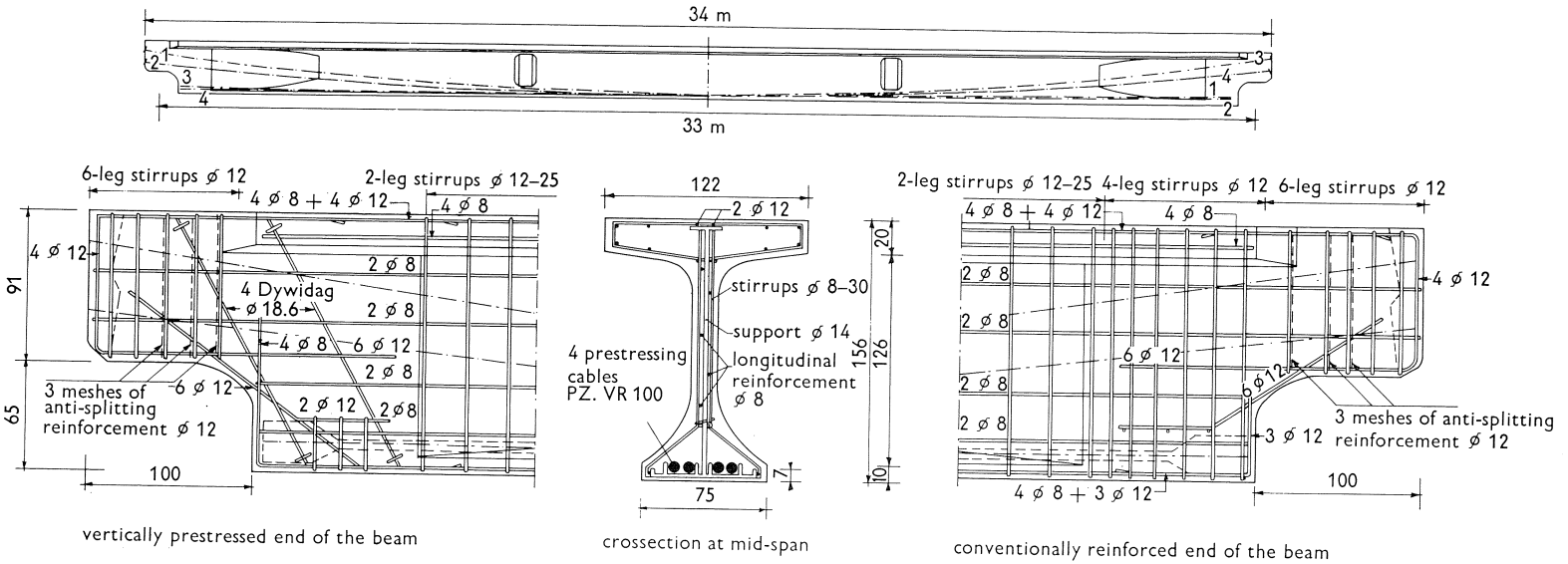


Fig. 1.1. Elevation of the beam, showing prestressing cable profiles and details of both tooth structures.

flexural behaviour of the beam, as well as to the behaviour of the tooth structures at both ends of the beam. In those days, experimental analysis was the only available method for determining the behaviour of complex structures. Analytical methods could only provide a rough estimate and were sometimes inadequate. The subsequent development of numerical tools now offers the possibility of studying the structural mechanism of both the prestressed concrete beam as well as the tooth structures in detail, taking into account physical non-linearities.
In this first example, the flexural experiment as well as the experiment on the "conventionally" reinforced tooth structures is simulated numerically and compared with the experiments. This example was chosen while relatively abundant experimental information was available, but also in order to demonstrate the insight into structural behaviour which can be obtained from a non-linear numerical simulation.

## 1.2 *Description of the problem*

The experiments carried out in 1965 have been reported in detail (CUR 1969). The overall structure is shown in Fig. 1.1. The total span of the beam is 33 m; four prestressing tendons are placed as indicated. The tooth structure at the right-hand end of the beam was conventionally reinforced; some additional vertical prestressing was provided in the tooth on the left-hand end of the beam. All dimensions as well as the reinforcement details are shown in Fig. 1.1.

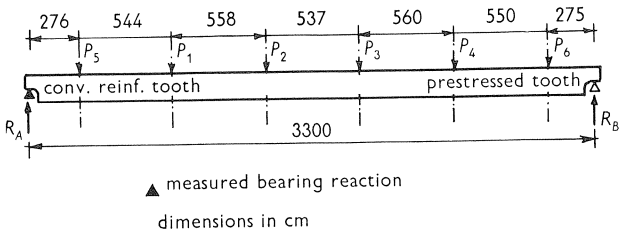


Fig. 1.2a. Loading procedure in the first flexural test.

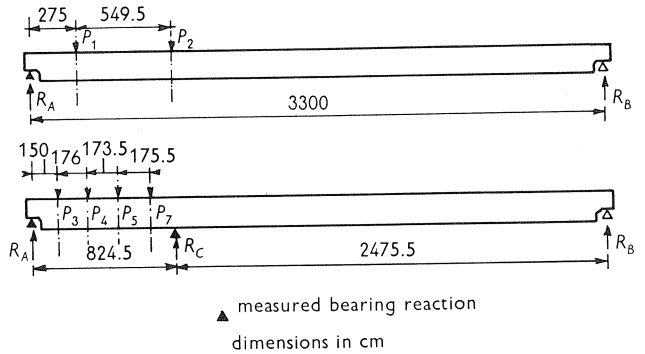


Fig. 1.2b. Loading procedure for the experiment on the conventionally reinforced tooth structure.

In a first flexural experiment, the beam was loaded up to 90% of the analytically determined failure load. The loading procedure is indicated in Fig. 1.2a. Loading was applied by six hydraulic actuators in an almost symmetrical arrangement. In the experiment on the conventionally reinforced tooth structure, the loading procedure was more complicated (see Fig. 1.2b). Initially, the structure was loaded by two concentrated loads $P_1$

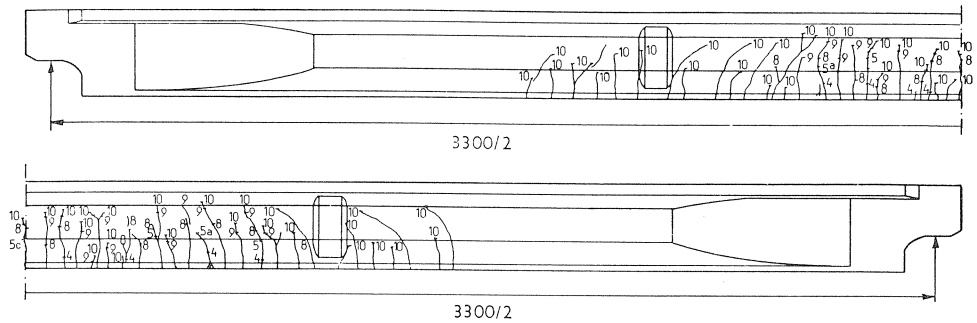


Fig. 1.3. Cracking in the first flexural test.

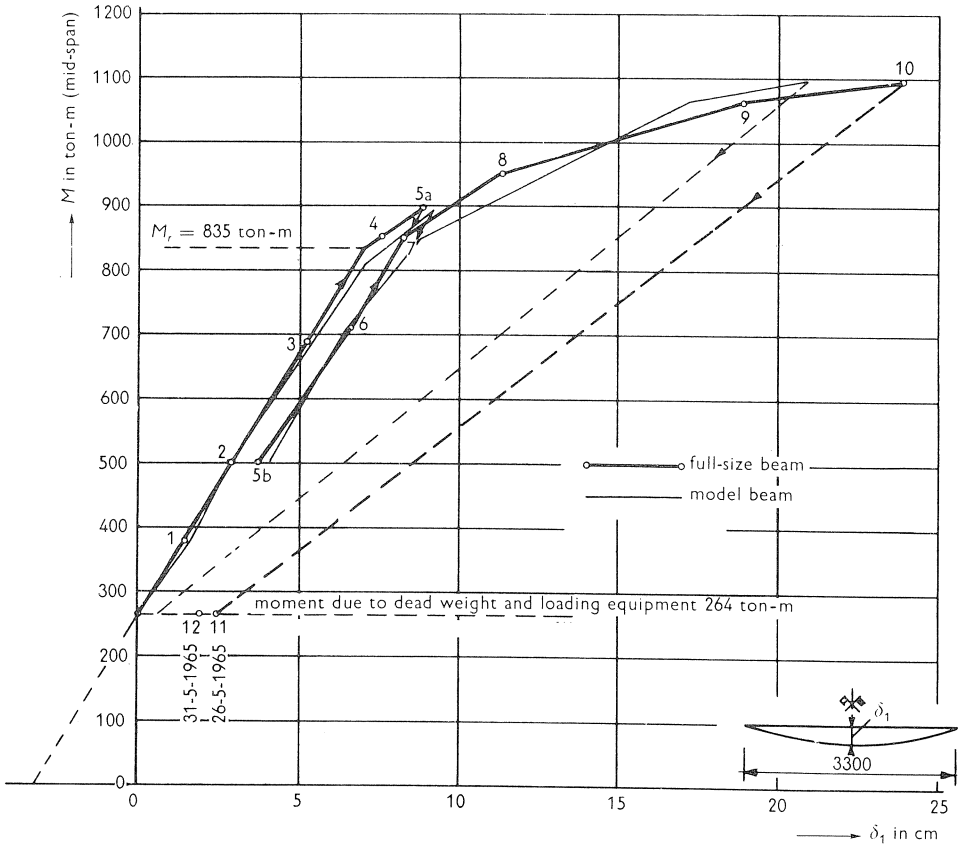


Fig. 1.4a. Load-deflection curves at mid-span for the first flexural test.

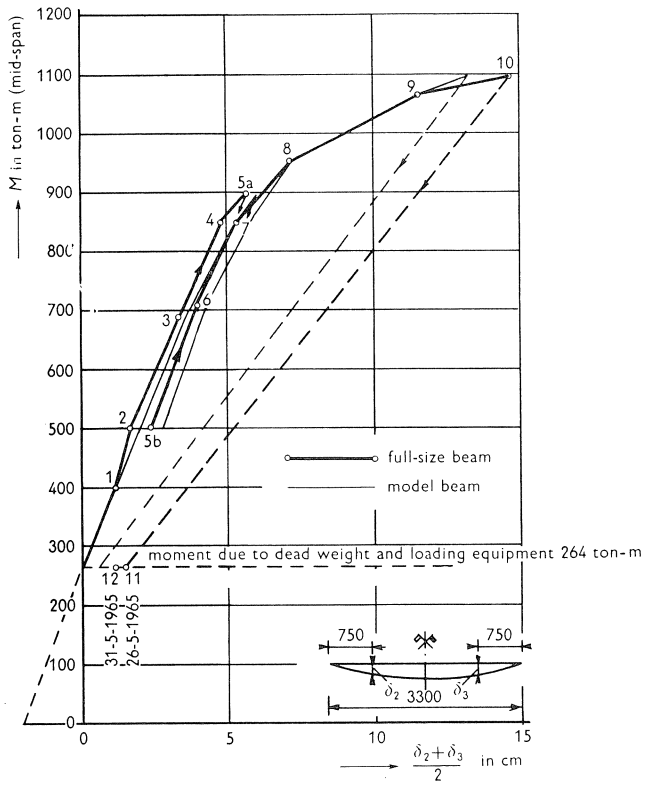


Fig. 1.4b. Load-deflection curves at 7.50 m from the supports for the first flexural test.

and $P_2$. After these loads had been increased to 700 kN, an additional support was placed ($R_c$) directly under load $P_2$. This was done in order to prevent fracture outside the end portion of the beam. Further loading was now applied by means of four concentrated loads ($P_3$, $P_4$, $P_5$ and $P_7$), while $P_1$ was kept constant at 700 kN. The load $P_2$, which was not subsequently adjusted, decreased from 700 to 290 kN during this loading process. Some of the experimental results are shown in Fig. 1.3 to 1.5. The observed crack pattern in the first flexural experiment is shown in Fig. 1.3. In Fig. 1.4, the load-deflection curves from the flexural experiment are given: at mid-span in Fig. a, and at 7.50 m from the supports in Fig. b.

In Fig. 1.5a, the load-crack width diagram as measured in the test on the conventionally reinforced tooth structure is shown. Also the result from the prestressed tooth structure appears in this diagram. In Fig. 1.5b, the crack pattern observed in the experiment on the conventionally reinforced tooth structure is shown. The numbers in Figs. 1.3 to 1.5 refer to the subsequent loading steps in the experiment. The tooth structure failed at a total bearing reaction $R_A = 2960$ kN (load step 21).

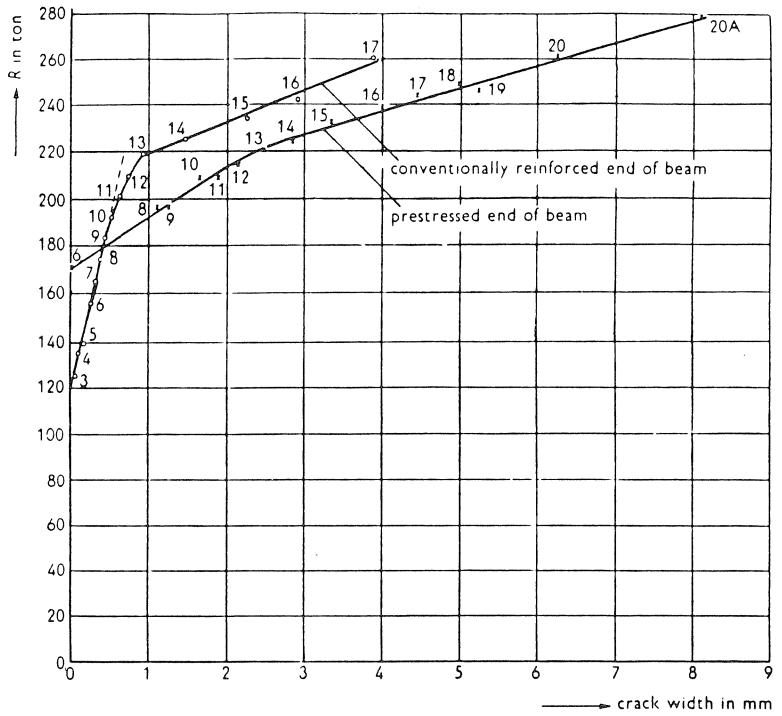


Fig. 1.5a. Crack width as a function of the total bearing reaction for both the conventionally reinforced tooth and the prestressed tooth structure.

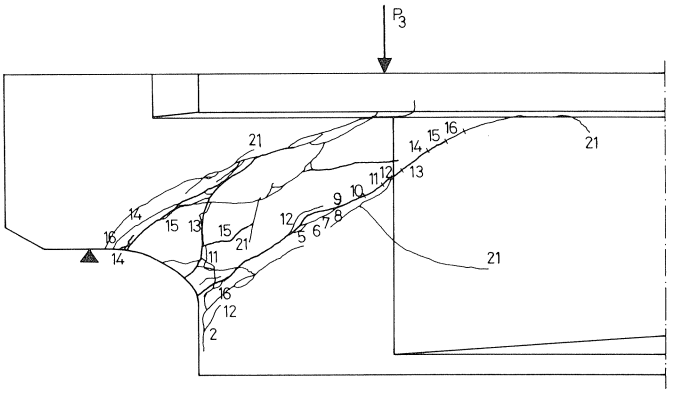


Fig. 1.5b. Cracking in the experiment on the conventionally reinforced tooth structure, numbers refer to the subsequent load steps.

## 1.3 *Parameters for the analysis*

In the numerical analysis, the beam structure has been schematized as a plane stress situation. In reality, the structure is three-dimensional, but a full three-dimensional analysis would require too much effort. It should be mentioned that some phenomena

cannot be simulated in the plane stress analysis (e.g. lateral splitting due to prestressing). Some of these modelling related problems will be discussed in the following sections.

### 1.3.1 Element discretization

The element mesh is shown in Fig. 1.6a. The mesh near the tooth structure is shown enlarged in Fig. 1.6b. As mentioned before, the beam has been schematized as a plane stress situation. Quadratic isoparametric elements with ninepoint Gaussian numerical integration, and triangular six-noded isoparametric elements were used. Three-noded numerical integrated bar elements were used for the reinforcement.
The reinforcement installed in the tooth structure is shown in Fig. 1.7. Perfect bond was assumed to exist between steel and concrete. Although the simulated crack growth will be influenced by this choice, this simplified approach has been adopted in the first instance. The use of bond-slip interface elements will be discussed in example 2 (corbel).
The prestressing tendons were assumed to have the shape of a second-order curve.

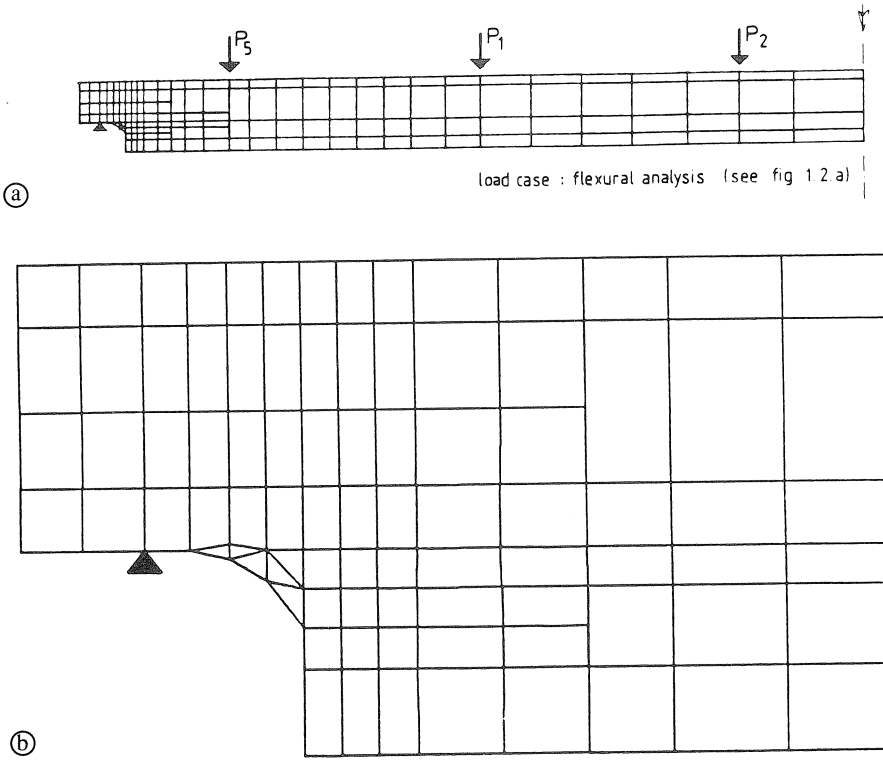


Fig. 1.6. Element mesh: overall view (a), and enlarged mesh near the support (b).

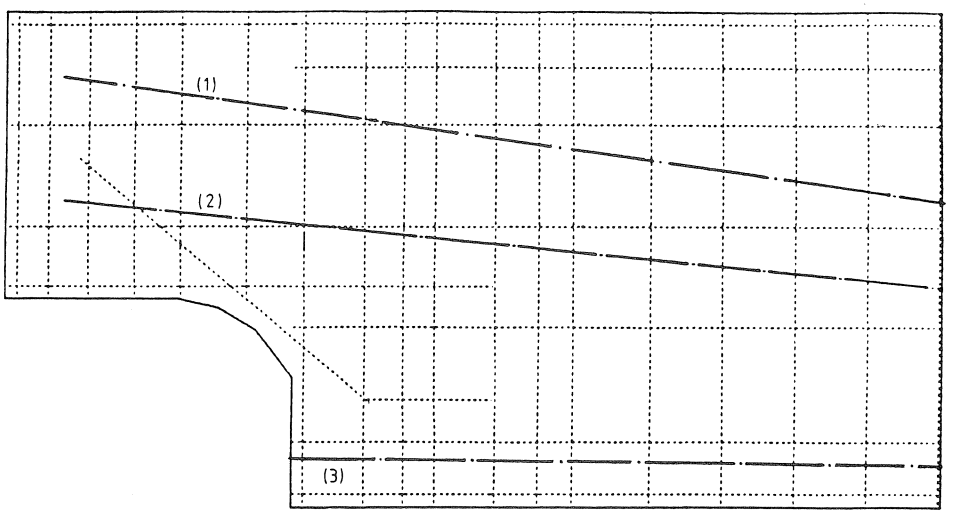


Fig. 1.7. Reinforcement in the tooth (dotted lines represent normal reinforcing bars, the dash dotted lines indicate the position of the prestressing strands).

Special attention was given to modelling the three-dimensional anchorage zone of the prestressing tendons in a plane stress situation; this will be discussed in Section 1.4. While the loading situation in the flexural experiment was almost symmetric, only half of the beam was considered. The element mesh was refined towards the tooth at the end of the beam, where also the triangular elements were used. This refinement was necessary because the same element mesh was adopted both for the overall flexural analysis and for the analysis of the conventionally reinforced tooth structure.
In the element mesh, the nodes of four elements are not directly connected to other nodes. This occurs when the mesh is refined. The "loose" nodes are tied to neighbouring nodes in order to maintain compatibility in the displacements.
The supports and concentrated loads were modelled according to the loading procedure in the experiments (see Fig. 1.2). In the experiment on the conventionally reinforced tooth structure, the beam was additionally supported under load $P_2$ after some load ($R_c = 1400$ kN) was applied. In the numerical simulation, this support had to be defined from the beginning of the analysis. The loading situation was so adjusted as to assure that the support did not "become active" before load $P_1$ and $P_2$ reached the required level.

### 1.3.2 Material parameters

The material parameters used in the analysis, both for the concrete and the reinforcing steel, are summarized below. The material models adopted have already been explained in the introductory chapter.

*Concrete*
$E_c = 42000$ N/mm$^2$
$\nu = 0.2$
$f_{ct} = 5.2$ N/mm$^2$
$f_{cc} = 79.9$ N/mm$^2$
tension cut-off 2
$\varepsilon_{us} = 0.0019$
$\beta = 0.2$

*Reinforcing steel*
$E_s = 200000$ N/mm$^2$
$f_{sy} = 475$ N/mm$^2$

*Prestressing steel*
$E_p = 212000$ N/mm$^2$
$f_{py} = 1700$ N/mm$^2$

In the analysis of the conventionally reinforced tooth structure, $\varepsilon_{us}$ was varied: a second analysis was performed using $\varepsilon_{us} = 0.0008$, which means a reduction of the fracture energy by a factor greater than two. It should be mentioned that $\varepsilon_{us}$ is rather difficult to determine if the structure is not "unreinforced" (i.e. when the $G_f$ concept can be adopted), and also if it is not reinforced to such an extent that the tension stiffening concept can be used (see Chapter 0).

### 1.3.3 Analyses performed

In this example, three analyses were carried out:

1. Linear elastic analysis.
   The purpose of this analysis was to investigate how the prestressing anchors could be modelled realistically in the plane stress situation. An indication for the expected stresses in the "throat" of the tooth structure was obtained in advance from a photoelastic experiment (see Chapter 8 in (CUR 1969)).
2. Non-linear flexural analysis, numerical simulation of the flexural experiment.
3. Non-linear analysis of the tooth structure:
   a. $\varepsilon_{us} = 0.0019$
   b. $\varepsilon_{us} = 0.0008$

## 1.4 *Results*

### 1.4.1 Prestressing anchors

Three prestressing tendons have been installed in the beam. Two tendons depart from the far end of the tooth structure where they were actually stressed in the experiment. The third tendon consists of two cables with a blind anchorage in the lower part of the beam. In order to avoid splitting of the concrete around the blind anchors of the two lower cables, a spiral reinforcement mesh was placed there in the experiment. In the analysis, the prestressing force in these lower cables was reduced linearly over the length of the spiral reinforcement mesh (i.e. the prestress was reduced over an effective length of 700 mm in the lower tendon). However, as a result of the lower (bottom) prestress only, a tensile stress $\sigma_{ct} = 4.85$ N/mm$^2$ was calculated in the throat. In the photoelastic experiment, a far lower tensile stress was found due to the lower prestress only ($\sigma_{ct} = 2.0$ N/mm$^2$). Yet, due to the distribution of the prestressing force over the length

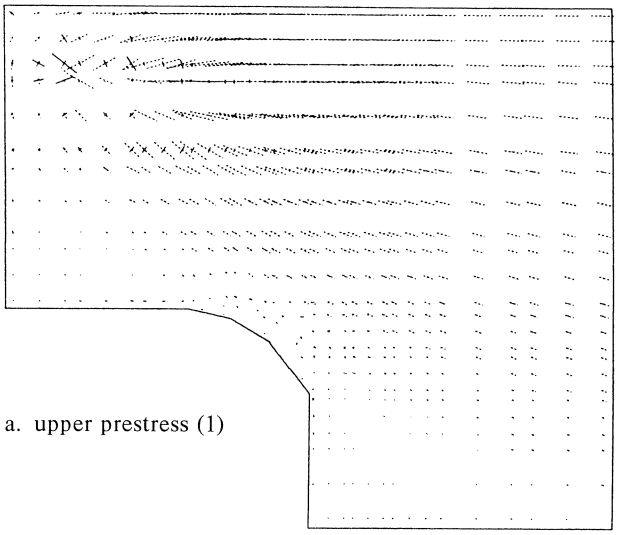

a. upper prestress (1)

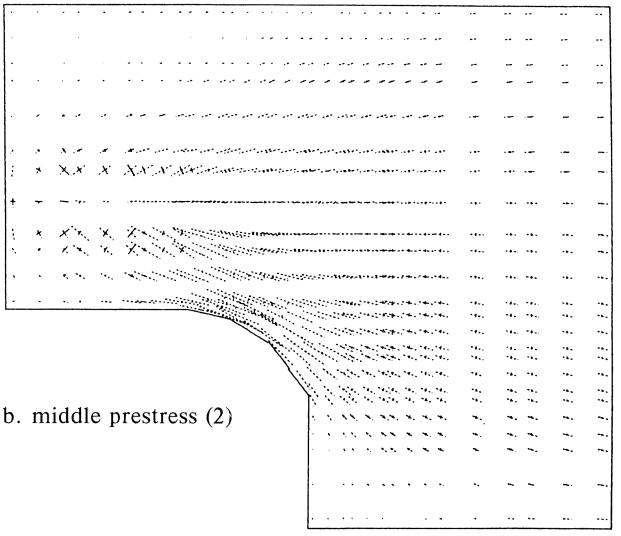

b. middle prestress (2)

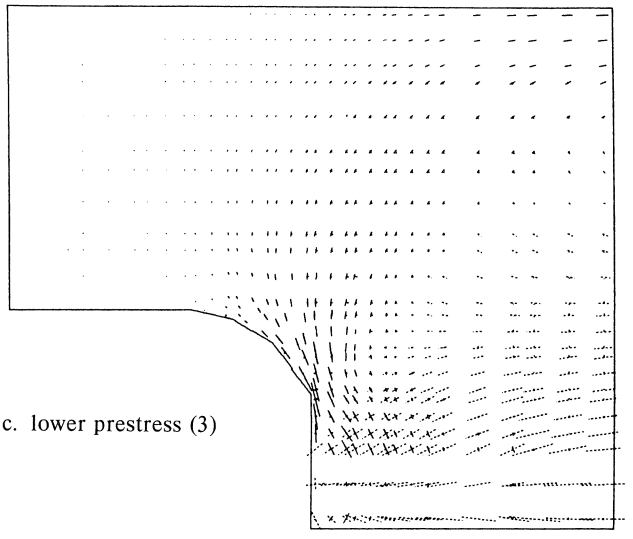

c. lower prestress (3)

Fig. 1.8.
Principal stresses in the tooth, due to prestressing only (dotted lines are compressive stresses, solid lines indicate tensile stresses).

of the spiral reinforcement a considerable reduction of tensile stresses in the throat was in fact obtained.
The principal stresses due to the separate prestressing cables are shown in Fig. 1.8. In these diagrams compressive stresses are indicated by dotted lines, tensile stresses by solid lines. The directions are the directions of the principal stresses.
The upper tendon (Fig. 1.8a) yields a compressive stress field in the upper part of the beam. Small tensile stresses appear where the tendon is fixed. Hardly any compressive stresses are generated in the throat due to the upper prestress only (i.e. $\sigma_c = -0.05$ N/mm$^2$).

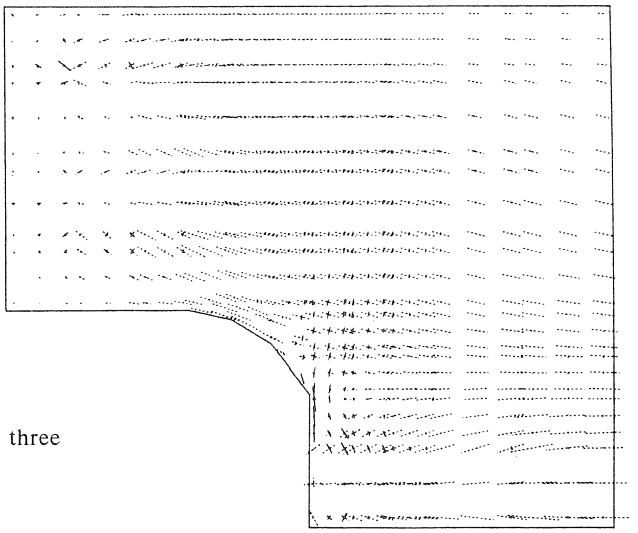

Fig. 1.9a. Combined effect of the three prestressing strands.

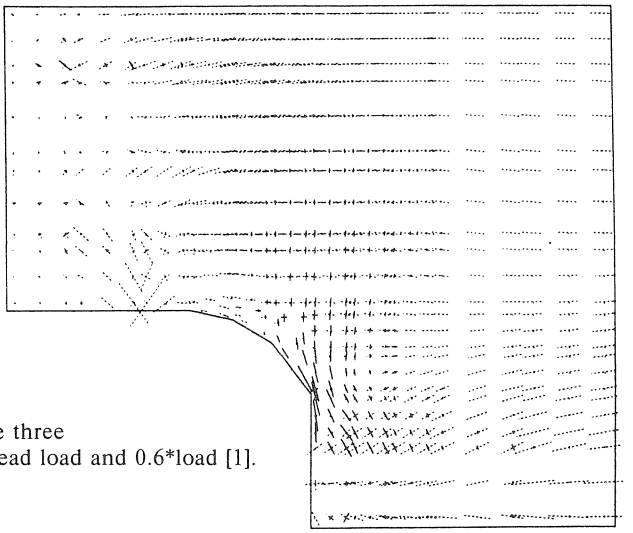

Fig. 1.9b. Combined effect of the three prestressing strands, dead load and 0.6*load [1].

Fig. 1.8b indicates that larger compressive stresses are generated in the throat due to the middle prestressing tendon.
Fig. 1.8c shows the principal stresses in the tooth due to the lower prestressing tendon only, and the extent of the tensile stressed region around the throat is clearly visible.
When the effects of the three prestressing tendons are combined, the principal stress distribution of Fig. 1.9 results. A tensile stress $\sigma_c = 3.75$ N/mm$^2$ remains in the throat. In the photoelastic experiment (CUR 1969), the resulting stress in the throat is compressive. In the analysis a compressive stress in the throat seems attainable only when the prestressing stresses in the upper and middle tendons are exaggerated or by further distributing the prestressing force in the lower tendon around the blind anchor.
It should be realised that in the actual experiment in the full-sized concrete beam the prestressing force around the anchor will be distributed three-dimensionally. At the moment, it does not seem fruitful to try to fit the results of the photoelastic experiment more closely in view of these modelling related problems.

### 1.4.2 Flexural analysis

The first non-linear analysis comprises the analysis of the complete prestressed beam in flexure. The loading was applied incrementally in steps just as in the flexural experiment.
The results of the flexural analysis are shown in Figs. 1.10 and 1.11. In Fig. 1.10, the moment-deflection diagrams, both at mid-span and at 7.50 m from the supports are shown. In these diagrams the results of the analysis are compared with the experimental results. The results show that a good numerical simulation of the flexural experiment is possible by using the non-linear numerical tool. The "cracking moment" is predicted

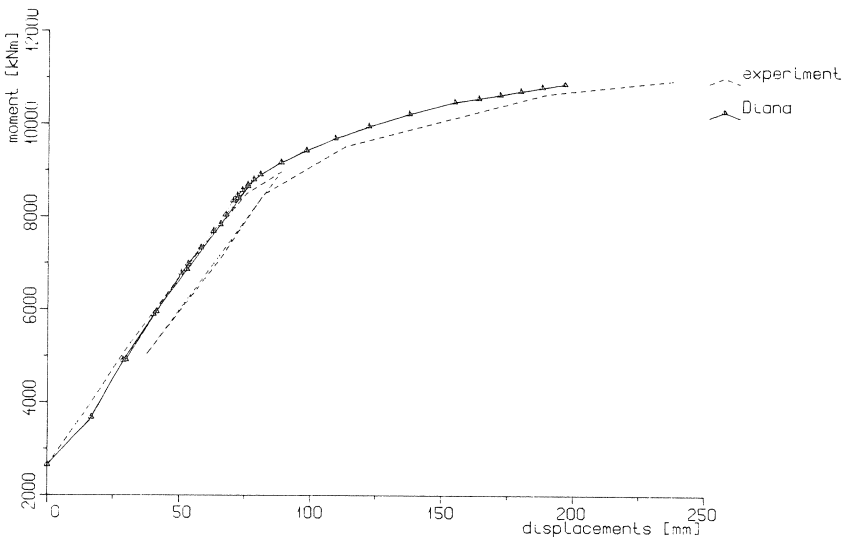


Fig. 1.10a. Calculated moment-deflection diagrams at mid-span (flexural analysis).

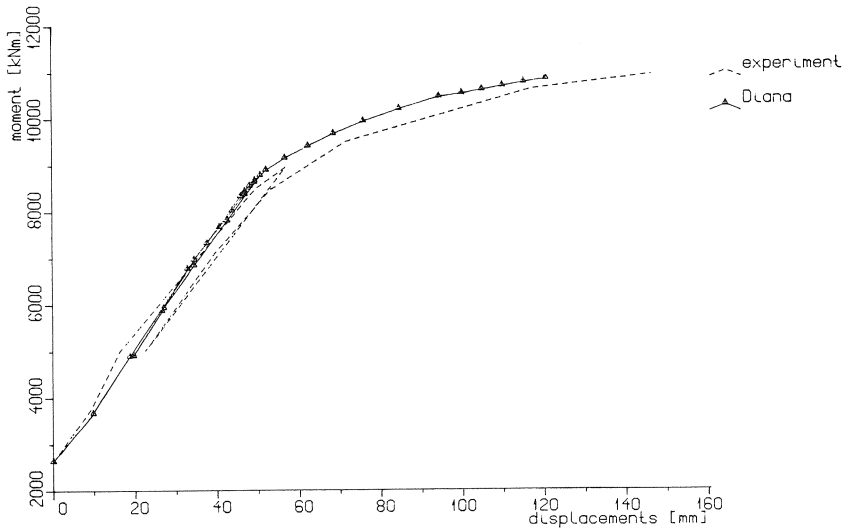


Fig. 1.10b. Calculated moment-deflection diagram at 7.50 m from the supports (flexural analysis).

between 8000 and 8500 kNm. The exact cracking moment cannot be determined more accurately because load step 4 was applied in one increment. The only significant difference between the analysis and the experiment is the amount of deformation during load step 5a. The deformations in the experiment are somewhat larger, probably due to creep at this relatively high loading level. Creep phenomena were not taken into account.

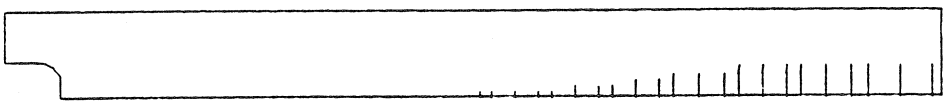

Fig. 1.11a. Cracking in the flexural analysis after load step [8], (total moment = 9500 kNm).

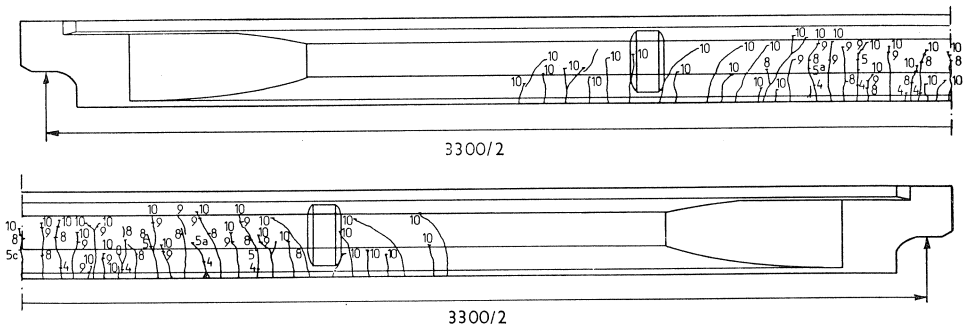


Fig. 1.11b. Cracking observed in the flexural test, the numbers indicate the subsequent load steps.

The calculated crack pattern after load step 8 is shown in Fig. 1.11. Comparison with the experimental results show that a fairly good prediction of cracking in the flexural analysis is possible.

### 1.4.3 Analysis of the conventionally reinforced tooth structure

The results of the analyses of the conventionally reinforced tooth are shown in Figs. 1.12 to 1.18. First, in Figs. 1.12 and 1.13 some results of the analysis with normal tension stiffening are shown ($\varepsilon_{us} = 0.0019$). While in the experiment mainly "crack data" were reported, emphasis is placed on these results. In Fig. 1.12, the calculated crack patterns after load steps 6, 8 and 12 are shown (bearing reaction $R_A$ is respectively 1541, 1741 and 2092 kN), and it can be seen that crack propagation is severely underestimated in the analysis. Using the tension stiffening concept, the localized character of the diagonal crack is not very well simulated either.

As can be seen from Fig. 1.13, a considerable amount of tensile stress is still transferred in the crack band. Only in load step 12 has part of the crack become almost "stress-free" and may be regarded as a true separation in the material.

The results of a second analysis, but now with a considerable lower fracture strain ($\varepsilon_{us} = 0.0008$), are shown in Figs. 1.14 to 1.18. For comparison with the previous analysis and in order to demonstrate the effect of reducing the tensile fracture strain, crack patterns and principal stress plots for step 6, 8 and 12 are shown in Figs. 1.14 and 1.15. The crack band develops considerably faster, and tends to be less wide, especially in the beginning of the analysis. Agreement between the computed crack patterns of Fig. 1.14 and the experiment is satisfactory. From Fig. 1.15, it can be seen that the transfer of tensile stresses in the crack band is small from the beginning of the analysis. Upon further increasing external load, the crack length develops in accordance with the experiment, yet the total width of the crack band clearly is overestimated (see Fig. 1.16, crack pattern for load steps 12, 14, 16 and 17 with $R_A = 2092$, 2258, 2421 and 2598 kN respectively). No localization was found when cracks exceeding a certain crack strain were plotted. In this case both the width and the length of the crack band were considerably reduced.

In step 16, a small branching crack developed in the vertical direction. This branching crack also was observed in the experiment. After load step 17, the analysis was terminated. At this point the crack band had become very wide, but did not exceed the crack band length calculated in step 16. In the experiment, at this stage of loading, a second diagonal crack started to propagate from the support and almost parallel to the first diagonal crack. This second crack was not observed in the analysis. One might suspect that the total crack band width in the analysis includes both cracks that were observed in the experiment. However, the second diagonal crack in the experiment forms an upper boundary for the crack band rather than being included in it. No satisfactory explanation can as yet be given.

At load steps 14 and 16, small bending cracks were observed in the beam. These cracks have not been reported in the experiment.

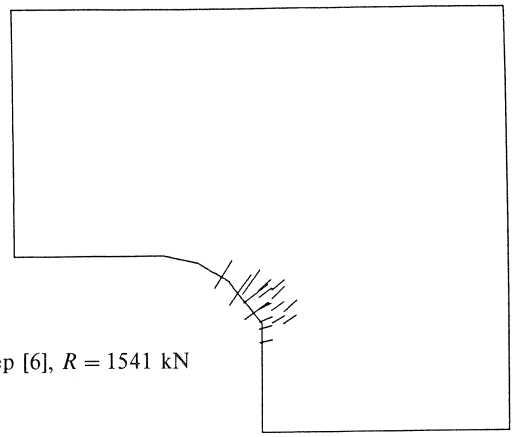

a. load step [6], $R = 1541$ kN

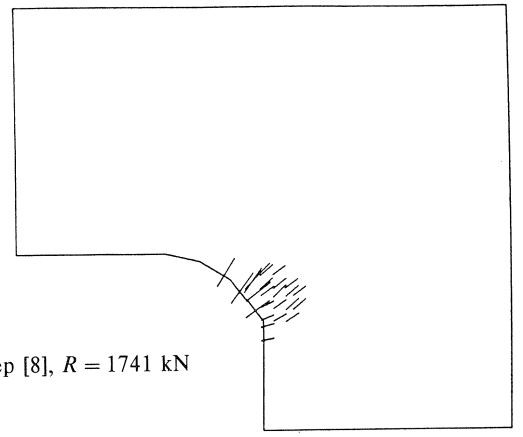

b. load step [8], $R = 1741$ kN

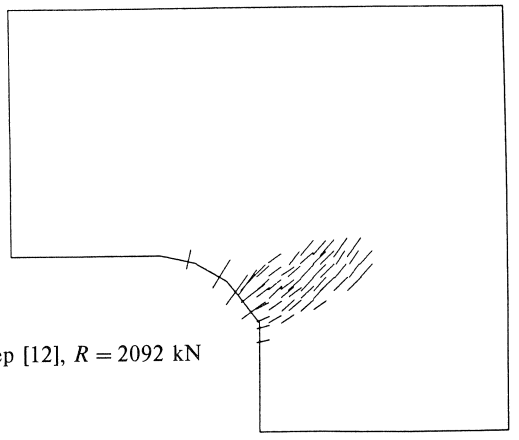

c. load step [12], $R = 2092$ kN

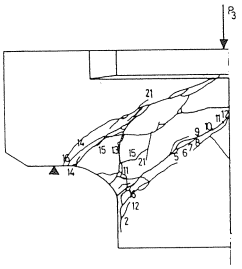

Fig. 1.12. Calculated crack patterns in the tooth (case $\varepsilon_{us} = 0.0019$).

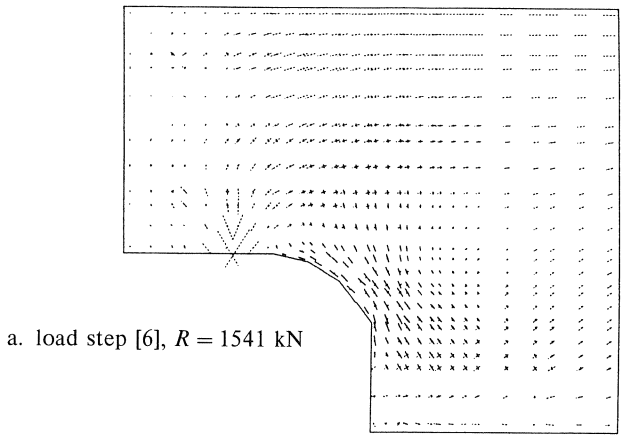

a. load step [6], $R = 1541$ kN

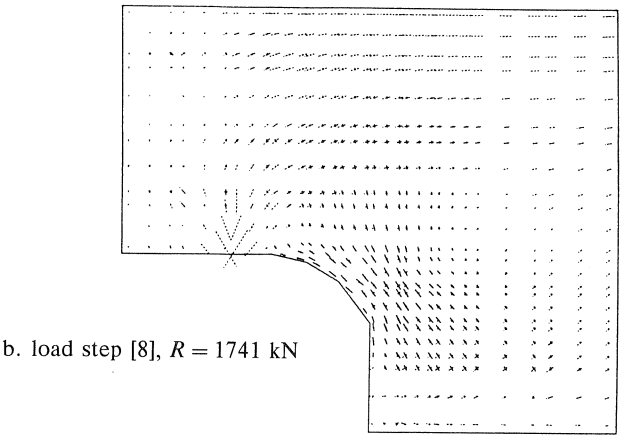

b. load step [8], $R = 1741$ kN

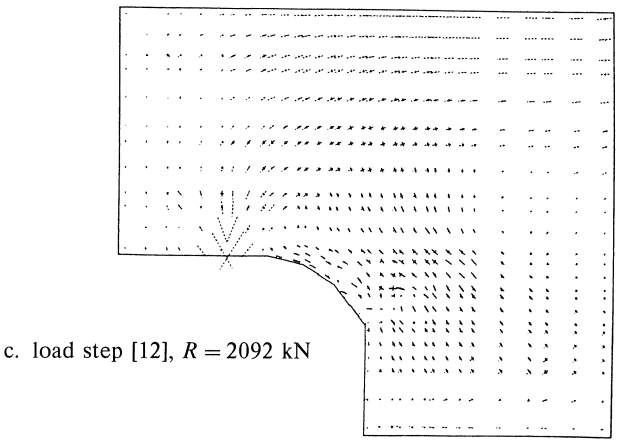

c. load step [12], $R = 2092$ kN

Fig. 1.13. Principal stresses in the tooth (case $\varepsilon_{us} = 0.0019$).

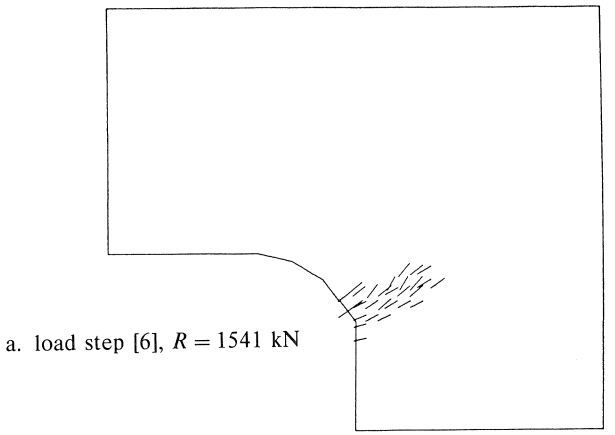

a. load step [6], $R = 1541$ kN

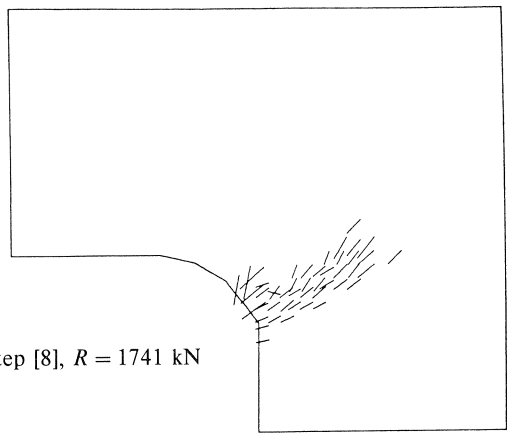

b. load step [8], $R = 1741$ kN

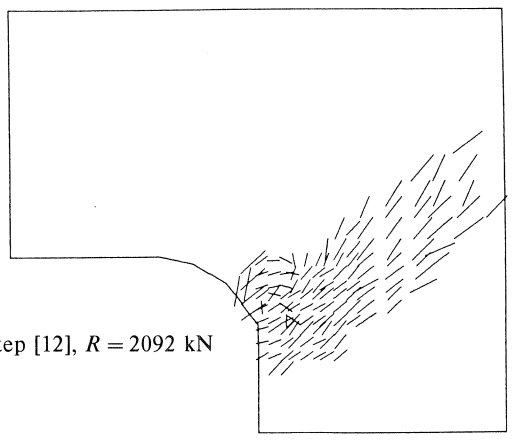

c. load step [12], $R = 2092$ kN

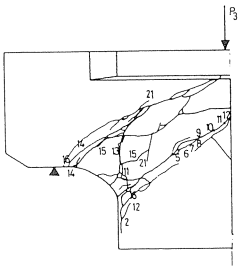


Fig. 1.14. Calculated crack patterns in the tooth (case $\varepsilon_{us} = 0.0008$).

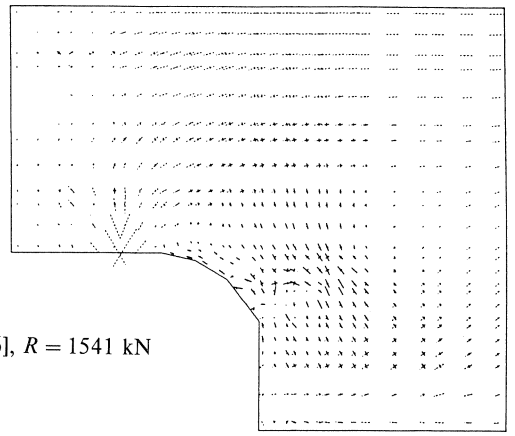

a. load step [6], $R = 1541$ kN

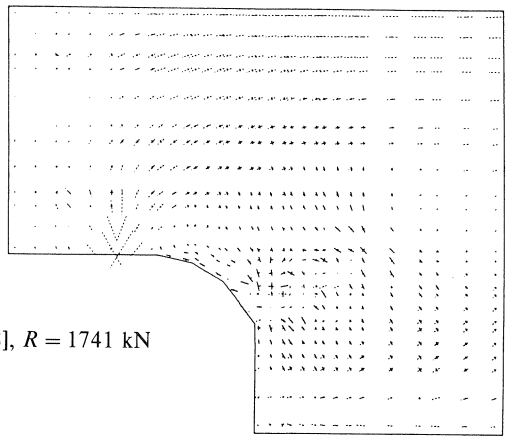

b. load step [8], $R = 1741$ kN

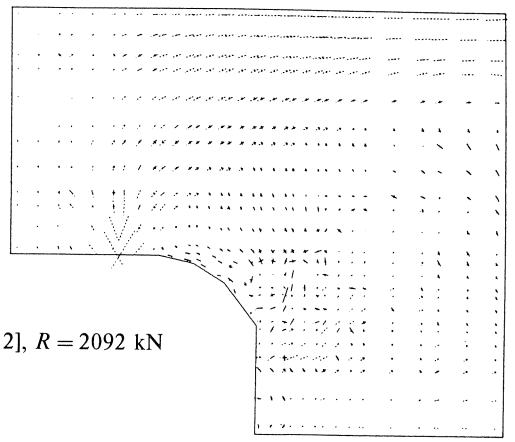

c. load step [12], $R = 2092$ kN

Fig. 1.15. Principal stresses in the tooth (case $\varepsilon_{us} = 0.0008$).

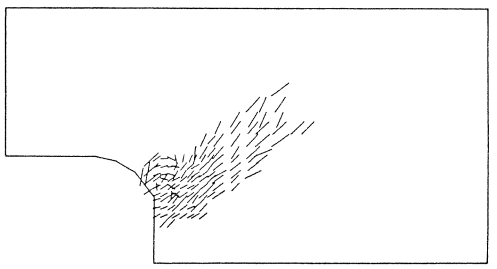

a. load step [12], $R = 2092$ kN

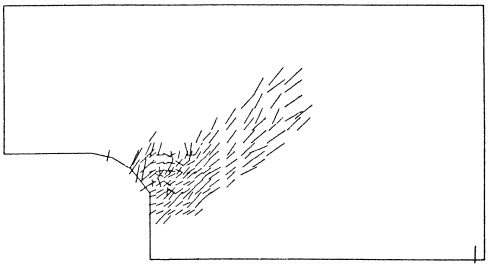

b. load step [14], $R = 2258$ kN

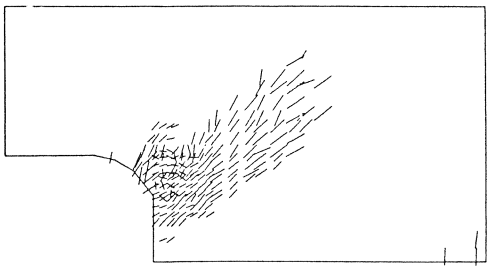

c. load step [16], $R = 2421$ kN

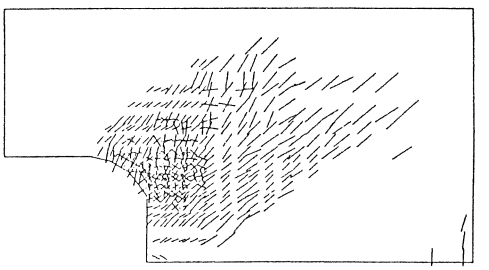

d. load step [17], $R = 2598$ kN

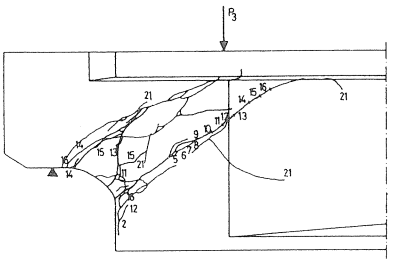

e. experimental results

Fig. 1.16. Calculated crack patterns in the tooth (case $\varepsilon_{us} = 0.0008$).

In Fig. 1.17, the computed total bearing reaction ($R_A$) has been plotted against the computed displacement of the lower edge of the beam (see inset). At a total bearing reaction $R_A = 2000$ kN a sudden increase in deformation occurs. At this point a pronounced increase in crack length is computed, and from Fig. 1.18 it can be seen that the increase in deformation is mainly determined by the increasing deformations in the cracked zone. Comparison with the experimental load-crack width diagram from Fig. 1.5a, shows a similar tendency. This may indicate that the onset and propagation of cracking in the throat is estimated rather well. Yet it should be mentioned that this could be obtained only by adjusting the $\varepsilon_{us}$ value. In comparison with the flexural analysis this value is rather small. A major problem remains as to what value for the fracture strain $\varepsilon_{us}$ should be adopted in practice.

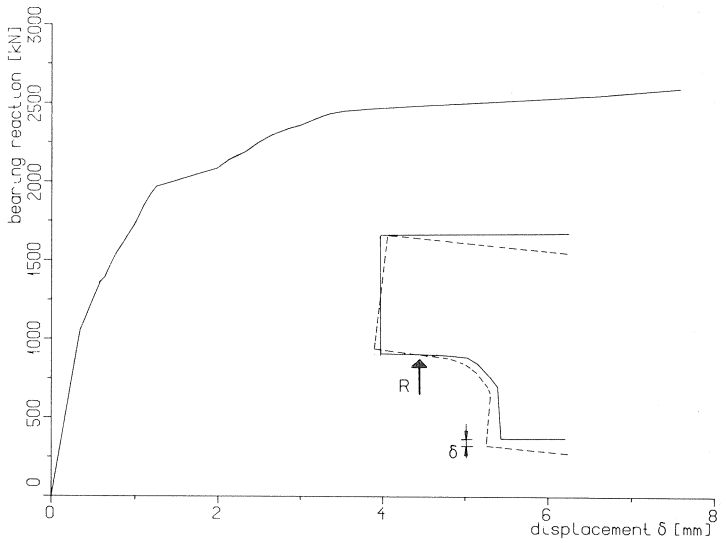


Fig. 1.17. Calculated load-deflection diagram for the analysis of the conventionally reinforced tooth structure.

## 1.5 *Discussion*

It has been shown that a reasonable numerical simulation of the flexural behaviour of a prestressed concrete beam is possible. Problems are encountered when a detailed analysis of the tooth structure is made. Especially the value for $\varepsilon_{us}$, which has to be used in the analysis is a major problem and seems to be not very clearly defined for different practical situations. The value of $\varepsilon_{us}$ needed for crack propagation clearly determines the rate at which the diagonal crack in the throat propagates. The dependency of the total structural behaviour on this "fracture energy parameter" is such that *prediction* of the structural response is hardly possible. In practice, this parameter should be varied, and it should be investigated if the structural mechanism of the tooth is influenced by

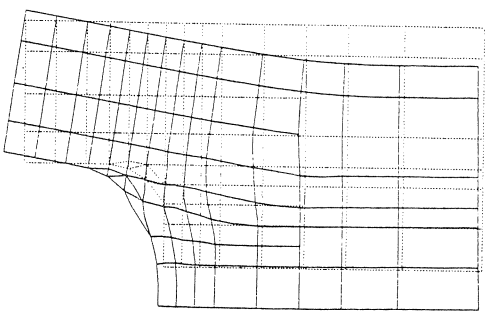

Fig. 1.18. Incremental deformations in load step [16] (case $\varepsilon_{us}=0.0008$), $R=2421$ kN.

this variation. On the basis of these comparative analyses one might make a *qualitative* statement on the structural behaviour of the tooth.
It should be mentioned that in the smeared crack concept, no crack widths, but rather crack strains are computed. Summation of all crack strains over the crack band width may give an indication of the expected crack width. It should be mentioned, however, that the crack width will depend considerably on the fracture strain as well.

### 1.6 *Conclusions*

The following conclusions can be drawn:
- A reasonable numerical simulation of the flexural behaviour of the beam is possible. Load-deflection curves and cracking are calculated accurately.
- In the analysis of the conventionally reinforced tooth structure crack initiation as well as the direction of crack propagation are simulated quite well. However, the development of the second diagonal crack was not observed in the analysis.
- The localized character of the diagonal cracks that were observed in the experiment cannot be simulated with the current model. The choice of the crack parameter $\varepsilon_{us}$ in the smeared crack model is still very difficult.
- In spite of the fact that a *prediction* of structural response is hardly possible, more insight into the *qualitative* structural behaviour can be obtained from a numerical simulation by investigating the influence of some of the model parameters.

## 2 Corbel

### 2.1 *Introduction*

This example comprises the analysis of a "one-sided" corbel. These structures are widely used, and while the analysis sometimes may be rather difficult, it was considered a good subject for numerical analysis. Surprisingly there is not much experimental material available for "one-sided" corbels, as contrasted with experiments on "two-sided" corbels (e.g. Kriz and Raths, 1965). The example chosen is based on experiments on full-scale corbels, carried out in 1961 (Niedenhoff, 1963). The aim of the experiments was to obtain some idea of the stress-distribution in these types of structures. This was done by comparing the results of a photo-elastic investigation with the crack patterns of the full-scale experiments. The experiments carried out by Niedenhoff, especially the one chosen in this example, are widely used to check results of calculations. For example Reich, 1983 used the same corbel for calibrating the results from scale tests on corbels.
In this example the result of two numerical analyses are discussed. First, an analysis with perfect bond between steel and concrete was carried out. In the second analysis, the effect of using special bond-slip elements between the reinforcing bar and the concrete, is demonstrated.

## 2.2 *Description of the experiment*

Experiments were carried out on four types of corbels, each type with different reinforcement. A total of 12 corbels was tested. The most practical experiment was chosen for numerical analysis, viz. No. M2/B2, which was also described by Reich (1983). Reich's report contains more information, in addition to the (not very detailed) material published by Niedenhoff.

Niedenhoff's tests were carried out on full-scale corbels; the dimensions of M2/B2 are given in Fig. 2.1a, details of the reinforcement are shown in Fig. 2.1b. The test set-up is shown in Fig. 2.2. As shown by the structural system, only the corbel was loaded; in the column, horizontal reactions appeared due to the loading on the corbel. During the experiment no displacements were recorded. Instead, results from a photo-elastic investigation were compared with the crack pattern and behaviour of the corbel at failure. Hardly any stresses developed in the lower outside corner of the corbel, and it was found that the resultant force of the principal compressive stresses followed the diagonal from the loading point to the lower inner corner of the corbel. Tensile stresses developed perpendicularly to this diagonal.

During the experiment, load-steps of 50 kN were applied. The first crack (No. 1 in Fig. 2.3) is reported in the second load-step ($P_t = 100$ kN). This crack developed into a main vertical crack at a load level of 150 kN. At $P_t = 300$ kN this crack was fully developed, and crack No. 2 (Fig. 2.3) developed, since the structural system changed. Cracks now occur in the column, but more cracks also develop in the corbel. Though not reported, it is likely that splitting cracks occur parallel to the plane of the corbel, since the radius of the curvature of the main reinforcing bars near the hook seems rather small. Finally, failure occurs at a load level of 585 kN when the main reinforcement starts yielding. At this stage crack No. 1 widens and the compressive zone in the corner fails (No. 3 in Fig. 2.3).

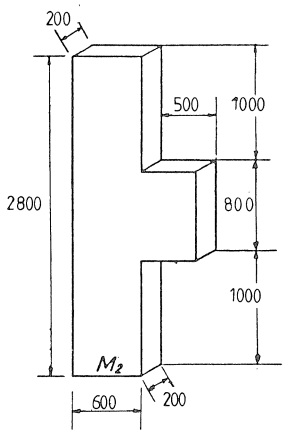


Fig. 2.1a. Dimensions of the corbel.

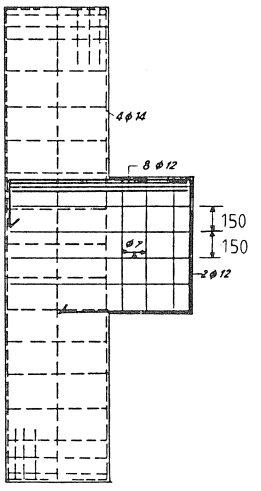


Fig. 2.1b. Reinforcement of the corbel.

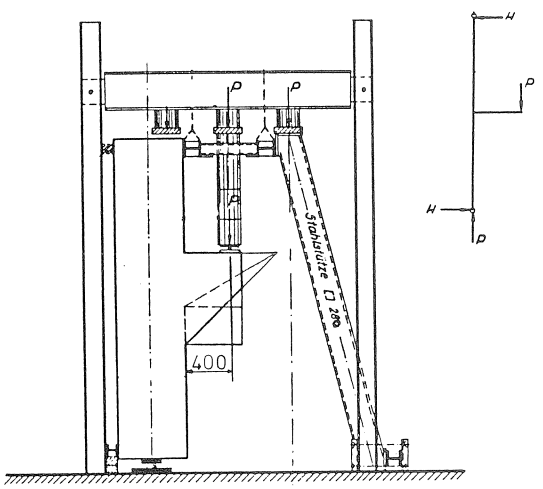


Fig. 2.2. Test set-up.

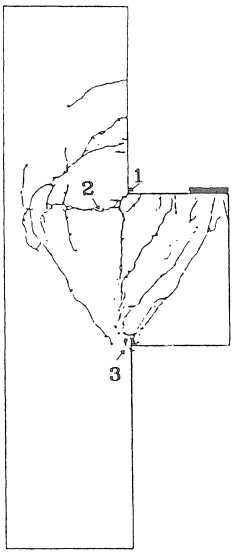


Fig. 2.3. Crack pattern at failure.

## 2.3 *Parameters for the analysis*

As mentioned before, two different analyses were carried out: first, *model A,* was analyzed, in which perfect bond between steel and concrete was assumed, and second, *model B,* in which the main reinforcement (8 ⌀ 12) was connected to the concrete by using special bond-slip elements. The parameters for the calculation of model B are mentioned only where they differ from those used in the analysis of model A.

### 2.3.1 Element discretization

In this example no advantage can be derived from symmetry, and the complete corbel has to be modelled. A full three-dimensional model has to be made if the structure is to be modelled realistically. This implies that in model B also three dimensional bond-slip elements should be used. Since this would make the analysis rather complex, the behaviour of the corbel is simulated in two dimensions. Typical three-dimensional effects cannot be described, such as for example splitting parallel to the plane of the corbel. It could be mentioned that in the experiments no splitting cracks were reported, although they could be expected (see also example 3, the beam-column connection). The element mesh of *model A* is shown in Fig. 2.4a. It is schematized as a plane stress situation. The elements are quadratic isoparametric elements with 8 nodes and 9 integration (Gauss) points. Also shown in the diagram are the supports and the three-noded reinforcement bar elements with three integration points. The main reinforcing bars are at the correct location, although they might give the impression that they are situated rather low. Niedenhoff (1963) reported that the reinforcement bars had moved during the casting of the concrete. Because in the experiment the load is applied

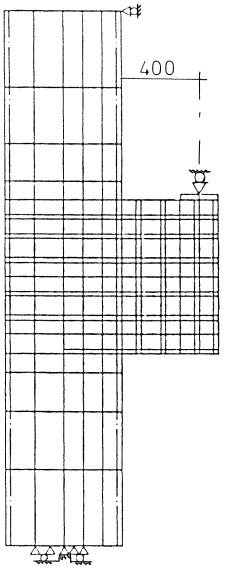


Fig. 2.4a.
Element mesh model A.

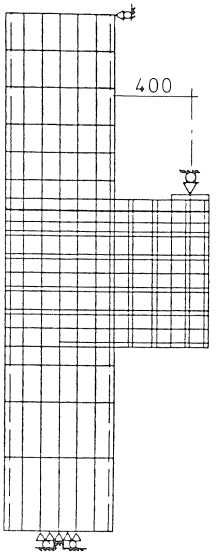


Fig. 2.4b.
Element mesh model B.

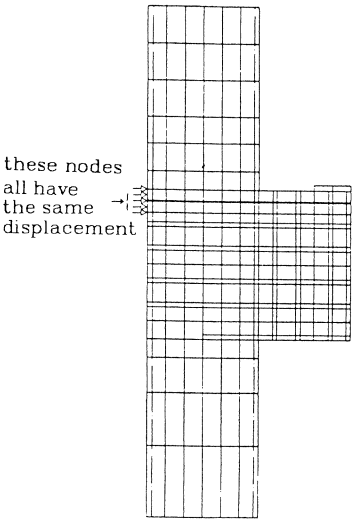


Fig. 2.4c.
Tyings of bond-slip elements.

through a steel platen, it has been included in the element mesh. The steel elements are kept linear-elastic in the analysis.

For *model B* the element mesh is adjusted, as indicated in Fig. 2.4b. The special bond-slip element cannot be situated in an element, as with the reinforcement bars of model A, but has to be modelled between the elements. Only the main reinforcement bars (8 ⌀ 12) are modelled as a bond-slip bar; for the other reinforcing bars full bond is assumed.

Apart from the bond-slip relation at the interface between reinforcement and concrete, another relation is introduced at the end of the bar. In the experiment, the bond length was increased by means of a hook on the main reinforcing bar. In the element model, the nodes at the end of the bond-slip bar are "tied" to the "concrete" elements that are situated above and below the main reinforcing bar. As a result, the displacements of both these concrete elements and the main reinforcing bar are the same (see Fig. 2.4c). By tying the bond-slip bar in this manner, in fact a steel platen is modelled at the end of the bar. This model was chosen, while modelling curvatures in reinforcing bars (e.g. hooks), in combination with bond-slip interface elements has not been done before in a numerical simulation with DIANA. Furthermore the hook is important in the third dimension (which was not modelled): it may be of major influence on the possible occurrence of splitting cracks in the third dimension.

### 2.3.2 Material parameters

The complete set of material parameters is given below. The material parameters are,

as far as possible, taken directly from Niedenhoff, 1963. The models are explained in Chapter 0.

*Concrete*
$E_c = 27000$ N/mm$^2$
$\nu = 0.2$
$f_{ct} = 2.42$ N/mm$^2$
$f_{cc} = 22.6$ N/mm$^2$
tension cut-off 1
$\varepsilon_{us} = 0.0017$
$\beta = 0.2$
The value of the tensile strength of the concrete is based on the formula: $f_{ct} = 0.87*(1.15 + 0.072*f_{cc})$. No value was reported in the experiments.

*Reinforcing steel*
$E_s = 210000$ N/mm$^2$
$f_{sy} = 350$ N/mm$^2$ for ⌀ 7
$f_{sy} = 282$ N/mm$^2$ for ⌀ 12
$f_{sy} = 300$ N/mm$^2$ for ⌀ 14
Niedenhoff reports different values for $f_{sy}$ for different bar diameters, the same values have been applied in the analysis.

*Bond-slip bar (model B)*
$S^z = 200$ N/mm$^2$
$\tau_{zu} = 5$ N/mm$^2$
$E_s = 210000$ N/mm$^2$
$f_{sy} = 282$ N/mm$^2$ ( ⌀ 12)

The bond-slip relation for the bar is explained in Chapter 0. Next to the total cross-sectional area of the bars, (which is 8 ⌀ 12 in the current example), the total surface area of the bars is important in a two-dimensional analysis. Here it is taken as $8*(2 \cdot \pi \cdot r)$, with $r = 6$ mm. It is assumed that along the edge of the bars full bond can develop. However, this is possible only when the mutual distance between the bars is not too small. In the experiment the distance was approximately 30 mm, which seems enough to enable full bond to develop.

### 2.3.3 Load case

In this example only one load case is considered. The external load is applied through the steel platen on top of the corbel. The load can be applied either in load or in displacement control. In this case, a displacement controlled process is chosen.

## 2.4 *Results*

First, in Section 2.4.1, the results of the analysis using model A will be discussed and

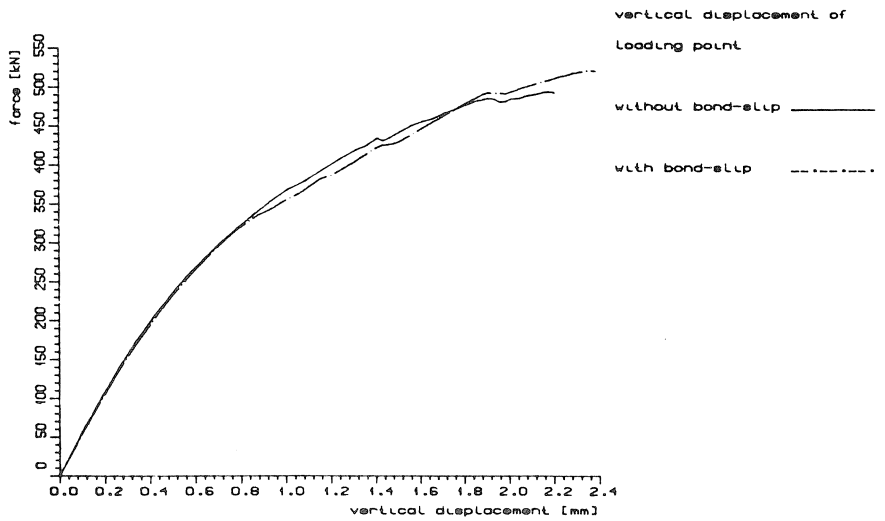


Fig. 2.5. Load-deflection curves.

compared to the experimental results of Niedenhoff. In the discussion of the results of model B, emphasis is placed on the differences with respect to model A.

### 2.4.1 Model A

The computed load-deflection curve is shown in Fig. 2.5. The vertical displacement of the loading point is plotted against the total load. Unfortunately, the computed curve cannot be compared with the experiment, because no displacements were measured in Niedenhoff's experiments. The computed load-deflection curves indicate that failure proceeds very gradually. In the experiment, crack No. 1 appeared rather suddenly (Fig. 2.3) and may have some influence on the shape of the load-deflection curve.
The displacements in the linear-elastic stage are shown in Fig. 2.6. It gives an indication if the input of the loadings and supports are correct. Principal stresses in this stage are plotted in Fig. 2.7a, and may be compared with the results of a photo-elastic investigation (Fig. 2.7b), which was part of Niedenhoff's experimental program. The general impression is that the results are similar: a concentration of tensile stresses appears in the upper corner between the column and the corbel; a concentration of compressive stresses develops simultaneously in the lower corner. Clearly visible are the stress-concentrations under the loading platen, as well as a rather large, almost stress-free region in the lower right corner. Quite often, the lower right corner is cut-off, and the reason for this will be obvious.
The first crack arises, both in the analysis as in the experiment, in the upper corner. The exact level, at which crack initiation occurs is not very well reported in the experiment (viz. somewhere in the load-step between 50 and 100 kN). In the analysis, first cracking occurs at a load level of 48 kN, but it may well be that these first cracks cannot be seen

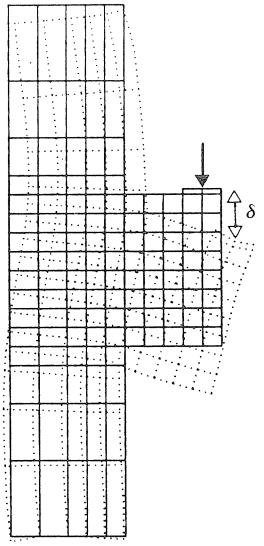


Fig. 2.6. Displacements, linear elastic stage.

with the naked eye. It is also more interesting to compare the cracks at a load level of around 300 kN, when the vertical crack (No. 1, see Fig. 2.3) is fully developed as well as the other main crack (No. 2). This is shown in Fig. 2.8a, and as can be seen, the crack lengths are predicted rather well. What is calculated, however, is not a localized crack, but a fairly large cracked area. This problem may be partly due to the large amount of diffuse reinforcement in the corbel. In fact, the problem is similar to that observed in the analysis of the conventionally reinforced tooth structure (see 1.4.3).

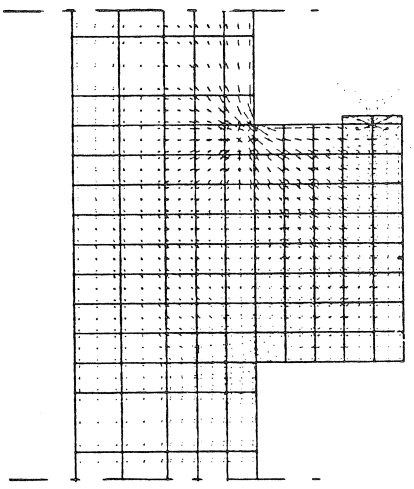

Fig. 2.7a. Principal stresses, linear elastic stage

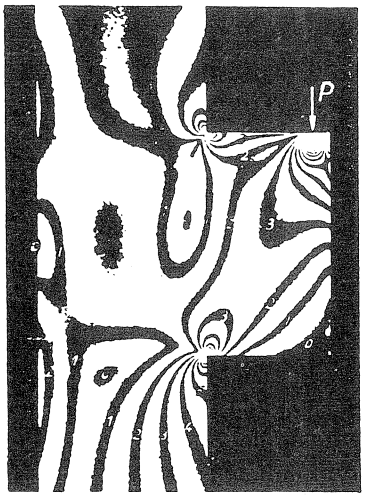


Fig. 2.7b. Photo-elastic results.

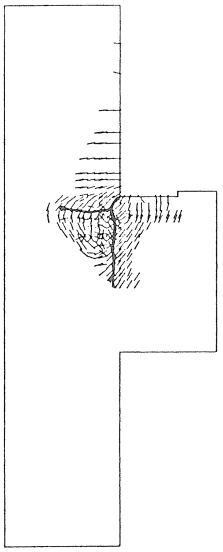

Fig. 2.8a. Crack pattern for model A, load-level 340 kN.

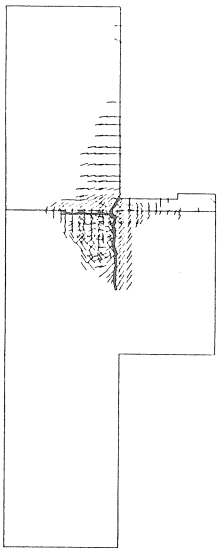

Fig. 2.8b. Crack pattern for model B, load-level 340 kN (the horizontal line indicates were the main reinforcement bar is situated).

At a load level of approximately 430 kN plasticity in the reinforcement was observed. First, the horizontal stirrups ( ø 7) below the main reinforcement started to yield. Next, the vertical reinforcement in the column at the side of the corbel started yielding, and finally the main reinforcement bar. Yielding of the reinforcement is indicated in Fig. 2.9a (the integration points where yielding is observed are indicated by triangles; the size of a triangle is an indication of the amount of plastic strain).
As soon as the main reinforcement starts yielding, the corbel fails. In the experiment a similar failure mechanism was reported. At the same time the compressive zone (No. 3 in Fig. 2.3) failed by crushing of the concrete. Plasticity occurs in the corner, and is indicated by triangles in Fig. 2.9b. The computed failure-load is 486 kN, 83% of the failure load observed in the experiment (585 kN).
At failure, the crack pattern observed in the experiment can be compared with the one predicted in the analysis. This is done in Fig. 2.10a and 2.10b. Again, the smeared crack approach makes it rather difficult to see where the main cracks are located. Nevertheless, the impression is that the location and directions of the cracks are predicted rather well.
Finally, the principal stresses are shown in Fig. 2.11 (in this case the results of model B are shown, but there is no significant difference for the corbel part). In the corbel, a compressive strut develops at an angle of approximately 30° with the vertical. This is, as also stated by Niedenhoff, the direction from the loading point to the lower corner between the corbel and the column.

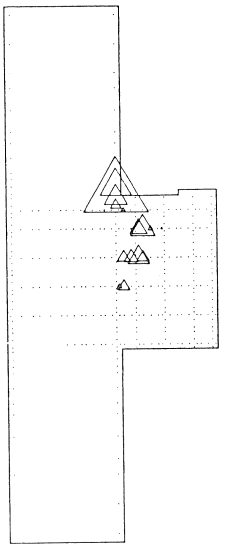

Fig. 2.9a. Plasticity of the reinforcement at failure.

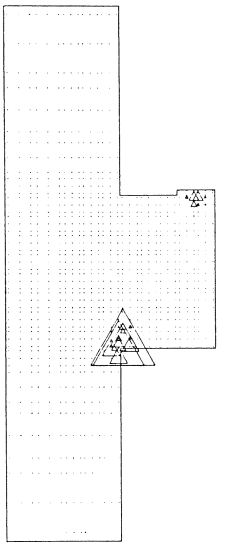

Fig. 2.9b. Concrete plasticity at failure.

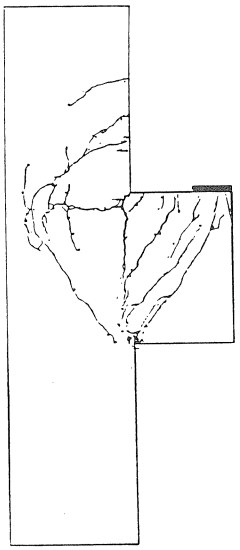

Fig. 2.10a.
Experimentally observed crack pattern at failure.

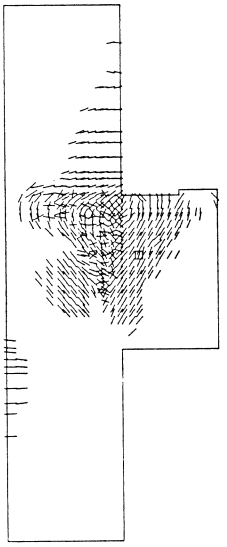

Fig. 2.10b.
Computed crack pattern at failure, model A.

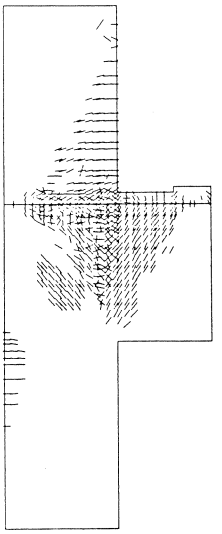

Fig. 2.10c.
Computed crack pattern at failure, model B (the horizontal line indicates where the main reinforcement bar is situated).

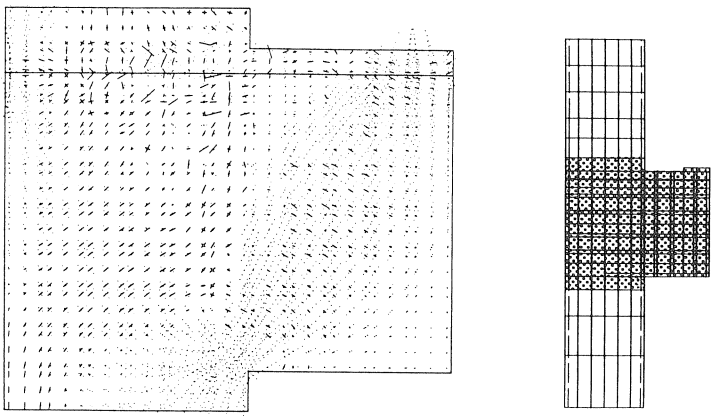

Fig. 2.11. Principal stresses at failure (only results in the shaded area of the corbel are shown; the horizontal line indicates where the main reinforcement bar is situated).

### 2.4.2 Model B

Up to a load level of 300 kN, no difference between the analyses with model A or B is found. This can be seen from the load-deflection curves in Fig. 2.5. The linear-elastic stage as well as the appearance of first cracks is similar to results obtained in the analysis with model A. The development of the vertical crack (between 150 and 300 kN) seems to be simulated more realistically when the bond-slip bar is used (compare Fig. 2.8a with 2.8b). The cracks are somewhat more localized, especially those along the bond-slip bar. Of course, the remaining horizontal and vertical perfect-bond bars (Fig. 2.4b) still have a "smear-out" effect on further crack extension.

The behaviour of the bond-slip bar is shown in Fig. 2.12. In this diagram the axial stress in the bar (Fig. 2.12a) and the bond shear stress (Fig. 2.12b) along the bar are shown at different load levels (starting at 360 kN, after the vertical crack has fully developed). The axial stress reaches a maximum where the vertical crack intersects the reinforcing bar ($x \simeq 0$); the highest values for the bond shear stress is calculated at both sides of the crack. The maximum level of shear-stress, is approximately 2.5 N/mm$^2$. At higher load levels, the bond shear stresses do not increase very much, only the location of the maximum changes slightly. Note that a second crack (at $x \simeq 200$) becomes important. At the highest load levels, around 500 kN, the bond shear stresses increase to a level of 4 N/mm$^2$, but this is not enough and the bar cannot slip yet. The main reason for this may be the presence of the other horizontal bars, which were modelled with perfect bond.

The failure load is predicted slightly better by this model: 520 kN, or 89% of the experimentally determined failure load. Yielding of the reinforcing bars proceeds in the same sequence as in the analysis with model A (compare Fig. 2.9a). First, the horizontal reinforcement below the main reinforcement (the bond-slip bar) starts yielding, next the vertical bar in the column and finally the main reinforcement (the bond-slip bar, see Fig. 2.12a). Also concrete plasticity occurs in the corner (compare Fig. 2.9b).

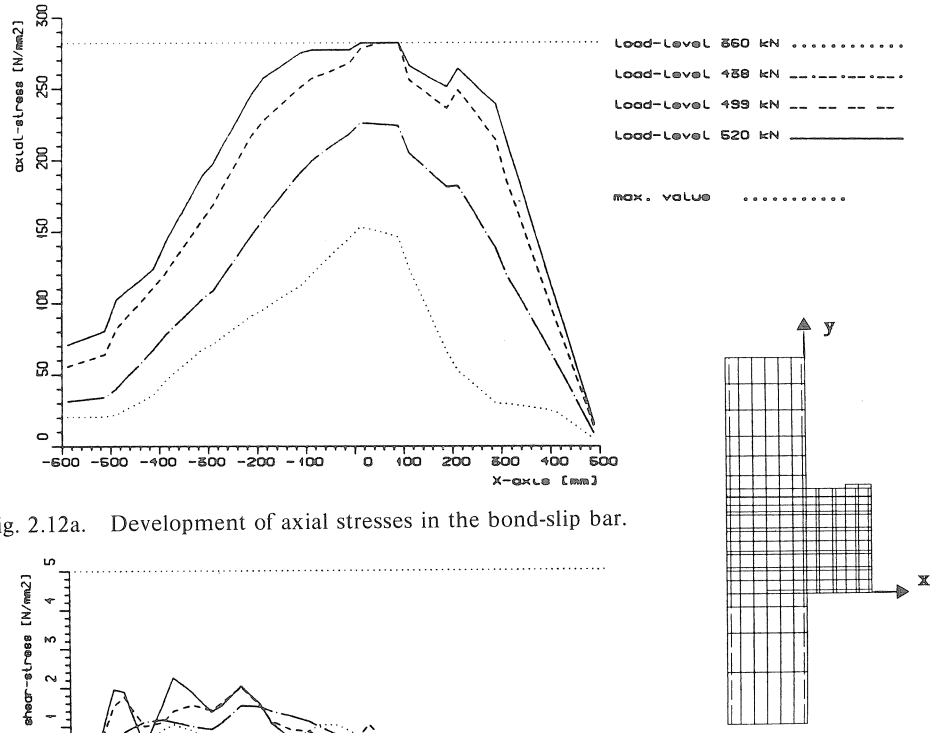


Fig. 2.12a. Development of axial stresses in the bond-slip bar.

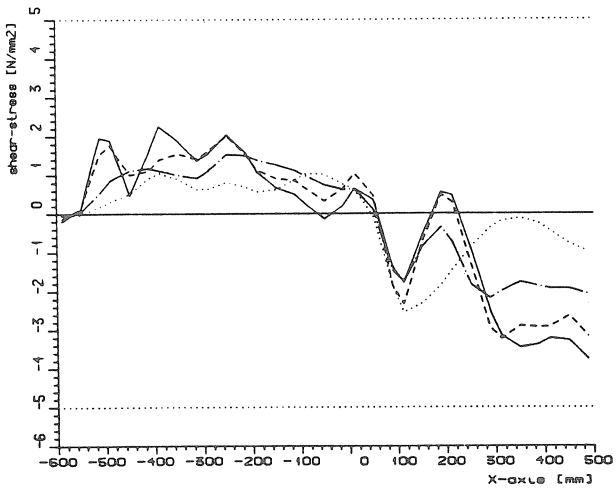


Fig. 2.12b. Development of shear stresses in the bond-slip bar.

Cracking at failure is shown in Fig. 2.10 and can be compared with the experimentally observed crack pattern as well as with the crack pattern computed with the perfect bond model A. The "localized" crack which developed initially has been considerably "smeared out". Near the bond-slip bar the pattern is somewhat better, but it is not spectacular.

The stress distribution in the corbel is almost similar to the one computed with model A. As already shown in Fig. 2.11, a heavily loaded compressive diagonal develops in the corbel. In the same diagram it can be seen that from the anchorage zone of the bond-slip bar, schematized by tyings, a compressive strut develops to the lower corner between

the corbel and the column. The development of this compressive strut may cause problems such as splitting cracks, compression failure of the diagonal and splitting of the lateral concrete cover. These problems are similar to those discussed in Chapter 3, the beam-column connection.

## 2.5 *Discussion*

The corbel has been simulated numerically with two different models. Several simplifications have been made, which are summarized below:

- In model A and B no three-dimensional effects are taken into account (e.g. splitting caused by the hooks of the main reinforcement, higher compressive strength in the lower corner between the corbel and the column; see also example 3).
- The meshes in both model A and B are relatively coarse, especially for model B in relation to the bond slip elements.
- In model A no bond-slip is taken into account, and in model B only the main reinforcement bar is modelled as a two-dimensional bond-slip bar.
- The hook at the end of the main reinforcing bar (the bond-slip bar in model B) was not modelled.

Hardly any differences are observed between the results obtained with the two models. In order to obtain more realistic results one could consider schematizing more bars as bond-slip bars, such as for example the vertical bar in the column. This bar is severely loaded, especially after crack No. 1 develops (see Fig. 2.3). However, for the simulation of the localized cracks, modelling of the other reinforcement bars (for example the horizontal stirrups) as bond-slip bars seems important.

Not only are these two dimensional simplifications important, but two other main problems are also encountered. First, due to the smeared crack approach it is difficult to simulate localized cracking in these types of structures and, second, when this problem is tackled by using bond-slip bars, the choice of the parameters for the two-dimensional bond-slip elements is problematic. The two problems are related: when the reinforcement is modelled completely with bond-slip elements, much better localization of cracks is expected, but then the problem of choosing the bond-slip parameters becomes important, especially in relation to the two-dimensional schematization. The element mesh has to be refined, which undoubtedly will lead to an increase in computer time.

## 2.6 *Conclusions*

The folllowing conclusions can be drawn:

- The failure load and overall behaviour at failure can be predicted satisfactory with a two-dimensional perfect-bond model.
- The results give a good idea of the way forces act in the corner.
- With the current models, it is not satisfactorily possible to simulate localized cracking in this structure with a diffuse network of reinforcing bars.

- Modelling the main reinforcing bar as a bond-slip bar does not lead to significantly better results. Relatively fine element meshes and more bond-slip elements are needed.

## 3 Beam-column connection

### 3.1 *Introduction*

In this example a single-bay portal frame is modelled. Special attention is given to a construction detail, viz. the beam-to-column connection. The behaviour of this structural joint is interesting because in this kind of structure it is commonly assumed that the joints are as strong as the connected members. However, in certain cases the strength of the joint may be lower.
In this example the corner joint is subjected to a negative moment and the behaviour of the joint and the frame is analysed. The causes of failure are studied, and an analysis of the stress distribution within the structural joint is performed. Some results are discussed and compared with findings from experiments.

### 3.2 *Description of the problem*

The overall dimensions, supports and loads on the frame are taken from investigations carried out by Stroband and Kolpa, 1983. The portal frame chosen is shown in Fig. 3.1 (this is a 1 : 4 scale model with no variation of the cross-sectional area of the beam and

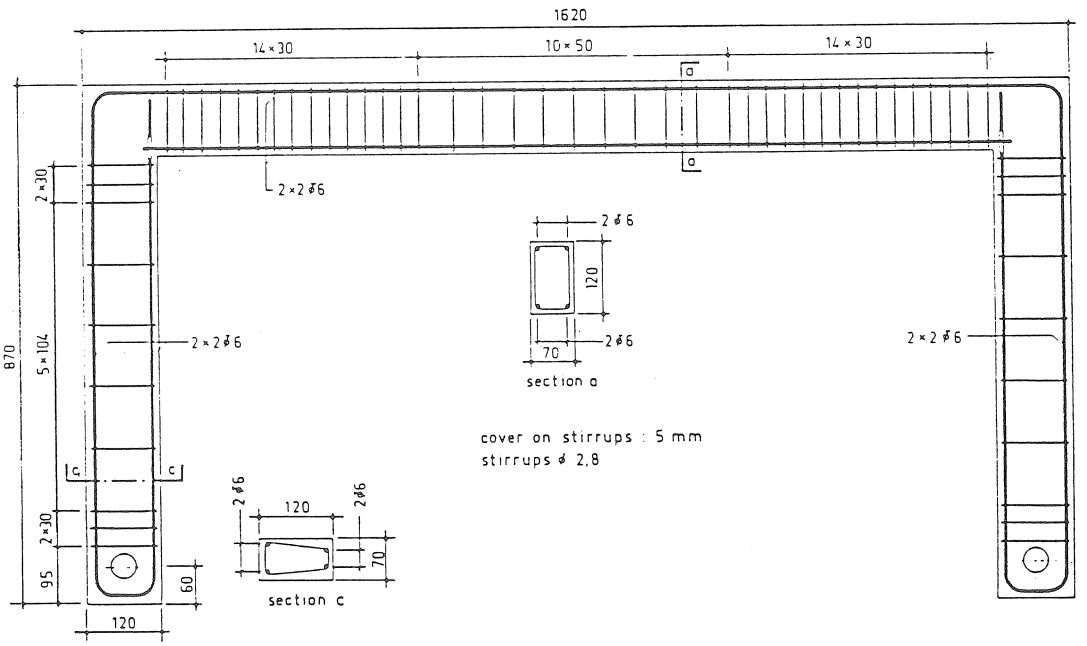


Fig. 3.1. Portal frame: dimensions and reinforcement details.

the column). The dimensions of the frame, as well as the reinforcement, are shown in the same diagram. The frame is loaded in accordance with the conditions of a four-point bending test (Fig. 3.2), causing a negative bending moment in the joint between the beam and the column.

Stroband and Kolpa base the strength of the joint on the condition that it should be able to resist a theoretical ultimate moment of the connected members at critical sections (see Fig. 3.3). From a truss model one can deduce the location of these sections and, on the assumption that the steel stress in the tensile reinforcement reaches a maximum, the theoretical ultimate moment can be calculated. In this case the calculated theoretical ultimate moment was equal to 2.69 kNm for Section I and 2.96 kNm for Section II (this is calculated without compressive reinforcement). The efficiency of the joint can be expressed by the ratio of the observed ultimate moment to the theoretical determined ultimate moment. A ratio of more then 100% means that the joint has sufficient strength in the limit state. The efficiency of the joint is determined in this analysis.

From Stroband and Kolpa it can be concluded that the first cracks in this kind of structure normally occur in the mid-span region of the beam and in the columns (Fig. 3.4a). Only in a more advanced stage does inclined flexural cracking (though rather randomly distributed) occur at the corners. Attention is paid to the nucleation and propagation of splitting cracks (Fig. 3.4b) and crushing at the inner angle causing failure of the joint. The development of splitting cracks mainly depends on the radius of the curved reinforcing bar in the joint. Other important parameters for the strength of the joint include the quality of the concrete, the lay-out of the main reinforcement and the thickness of the lateral concrete cover.

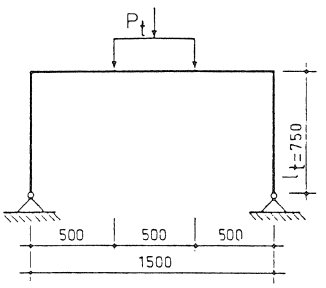


Fig. 3.2. Loading of the frame.

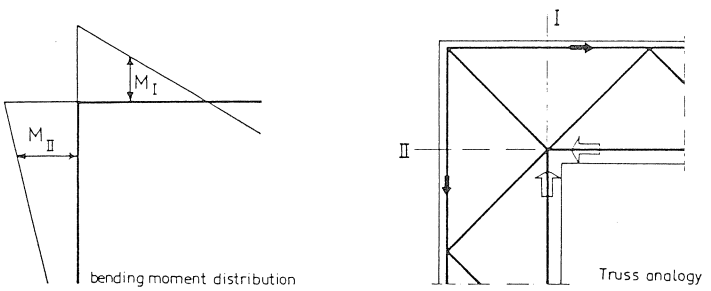


Fig. 3.3. Location of critical sections.

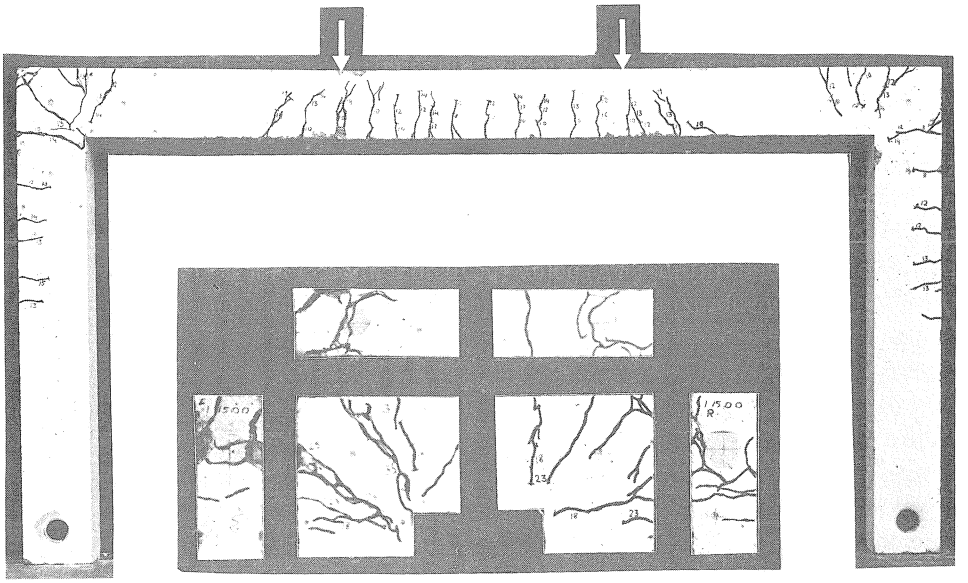

Fig. 3.4a. Example of crack pattern found in experiments.
Fig. 3.4b. Detail, cracking of corner and splitting parallel to the plane of the portal frame.

## 3.3 *Parameters for the analysis*

For a realistic analysis of the joint, a three-dimensional model would be required. Splitting of the concrete parallel to the plane of the portal frame influences the structural behaviour of the joint and cannot be simulated in a two-dimensional model. Yet, for the sake of simplicity, it was decided to perform a two-dimensional analysis of the complete portal frame. With this restriction it is not possible to vary and investigate parameters such as the radius of the curved reinforcing bar. Therefore, only some limited results are compared with the experiments (viz. the crack patterns).

### 3.3.1 Element discretization

The behaviour of the portal frame and the joint is described in two dimensions (plane stress). Eight-noded plane stress elements are used, with nine integration points. Due to symmetry of the frame and the loading conditions only half of the frame has to be modelled. The element mesh, reinforcement, loading and supports are shown in Fig. 3.5. The mesh is refined where stress concentrations are expected, i.e. in the corner and in the midspan region of the beam. Perfect bond is assumed between the reinforcement and the concrete.
The radius of the curved reinforcing bar in the joint was not taken into account. This may - as shown in experiments - have considerable influence on the behaviour of the joint (i.e. out-of-plane splitting). Moreover it should be noted that there is no experience in modelling of the anchorage of the reinforcement bars (e.g. hooks).

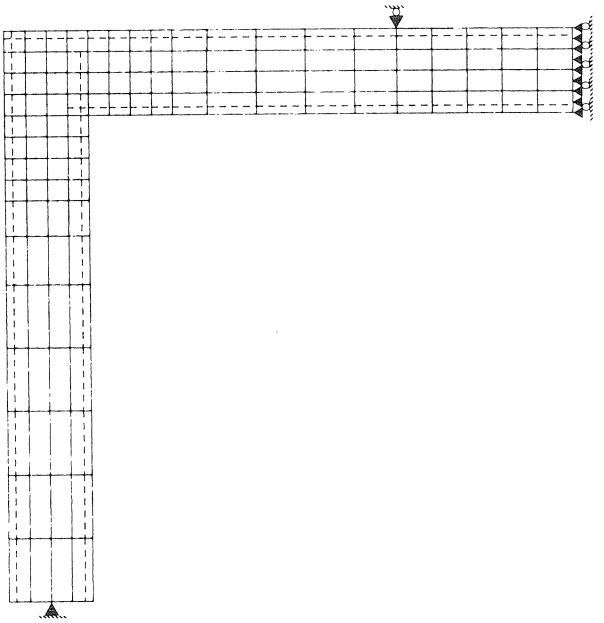

Fig. 3.5. Element mesh with reinforcement, loading conditions and supports.

### 3.3.2 Material parameters

The complete set of material parameters is listed below. All the parameters are explained in Chapter 0.

*Concrete*
$E_c = 28000$ N/mm$^2$
$\nu = 0.2$
$f_{ct} = 2.2$ N/mm$^2$
$f_{cc} = 25$ N/mm$^2$
$f_{cc} = 37.5$ N/mm$^2$ (in three inner corner elements)
tension cut-off 1
$G_f = 60$ N/m ($h = 60$–$20$ mm)
$\varepsilon_u = 0.00091$–$0.00273$
$\beta = 0.2$
In this analysis the so-called $G_f$ concept is used. The different values for $h$ and $\varepsilon_u$ are due to the different dimensions of the elements in which cracks may arise.
In the corner of the joint a three-dimensional compressive state of stress develops, and consequently the compressive strength of the three elements in the inner corner of the joint increased by a factor 1.5. As mentioned in Chapter 0, the Mohr-Coulomb yield criterion underestimates the strength of concrete under multiaxial states of stress. A confinement of 5% in the third direction ($\sigma_3 = 0.05\sigma_1$) yields a triaxial compressive

strength which is 100% higher than the unconfined biaxial strength (Van Mier 1984). This effect comes in addition to the underestimation of the biaxial strength in the Mohr-Coulomb yield criterion (see Section 0.2.2.2).

*Reinforcing steel*
$E_s = 210000$ N/mm$^2$
$f_{sy} = 450$ N/mm$^2$

### 3.3.3 Load case

Only one half of the frame is schematized, and consequently only one half of the load is applied to the frame (note that in the load-deflection curve and all other results the whole load is taken into account). The frame was loaded subject to displacement control. The effect of dead weight of the frame has been neglected.

## 3.4 *Results*

The computed load-deflection curve of the frame is shown in Fig. 3.6. The total load is plotted against the deflection at mid-span of the beam.
First a linear-elastic analysis is carried out. Some parameters can be checked by means of simple manual calculations (e.g. the stiffness of the frame). This gives an indication of the correctness of some parameters such as the modulus of elasticity. An indication of the behaviour of the frame at this stage can be obtained from the displacement plot (see Fig. 3.7). Positions of loads and supports can easily be checked with this plot. The stresses in the linear elastic stage are shown in Fig. 3.8. Fig. 3.8a gives an overview of

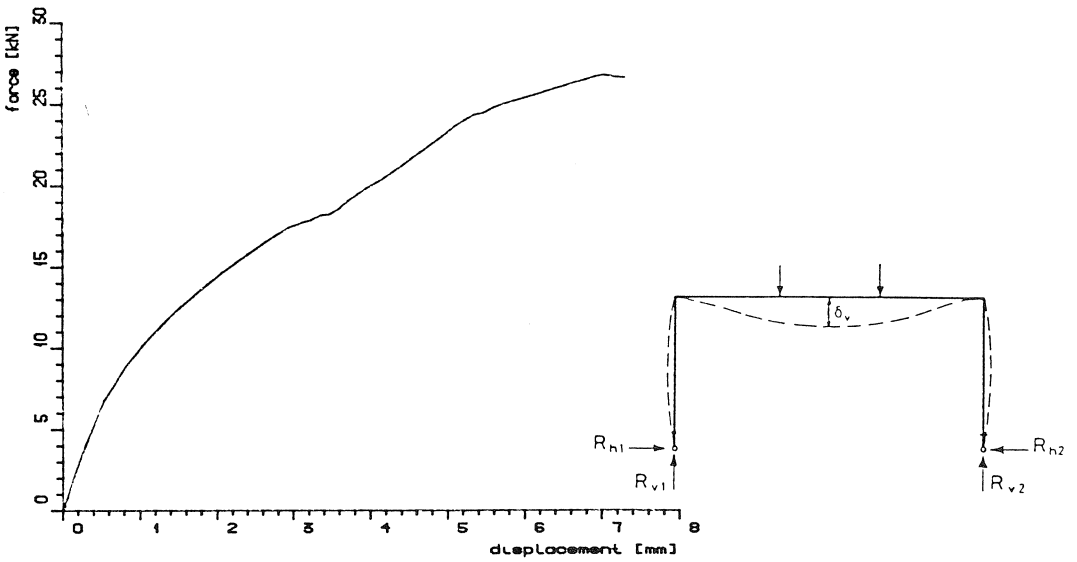


Fig. 3.6. Load-deflection curve (total load against deflection at midspan).

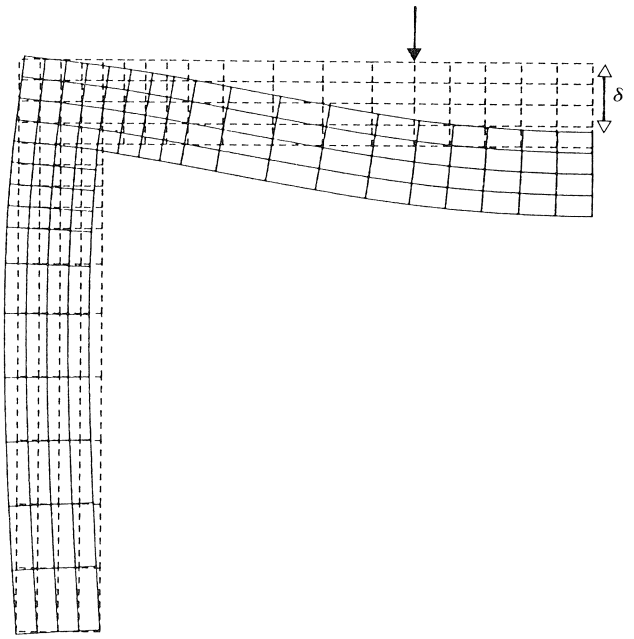


Fig. 3.7. Displacements, linear-elastic stage.

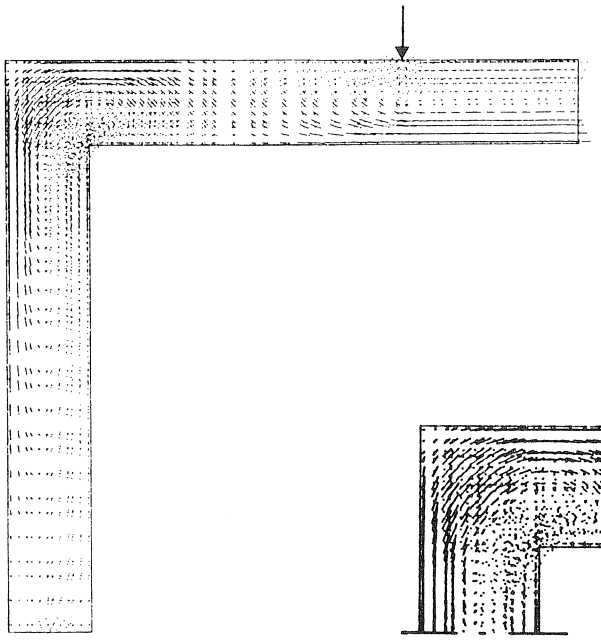

Fig. 3.8a.
Principal stresses,
linear-elastic stage.

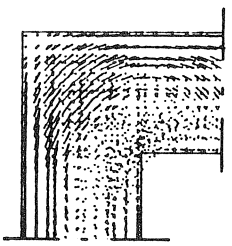

Fig. 3.8b.
Detail of the corner.

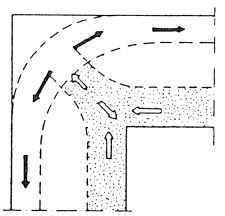

Fig. 3.8c.
Theoretical model.

the stresses in the complete frame, Fig. 3.8b gives some idea of the stresses in the corner, which is in fairly good agreement with a theoretical model of an uncracked corner (see Fig. 3.8c).

First cracks are computed at a load of $P_t = 4$ kN. These cracks appear in the mid-span region of the beam, and very shortly afterwards in the column near the joint. At a somewhat higher value of the load cracks develop in the beam close to the joint. Similar observations are made in experiments. In Fig. 3.9 a computed crack pattern at a load level of about 8 kN is shown.

The next interesting phenomenon occurs at a load $P_t \simeq 17$ kN, when a plateau in the load-deflection curve (Fig. 3.6) is observed. At this point, cracks suddenly widen considerably within a load step of 1 kN. This is shown in Figs. 3.10a and 3.10b where only the open cracks (i.e. with crack strains greater the $\varepsilon_u$) are plotted. The widening of the cracks is also demonstrated clearly with the plot of the incremental deformations in the last load step (Fig. 3.10c). The open cracks are situated in the elements with the largest incremental deformations.

After this point a redistribution of forces occurs in the corner, demonstrated by plots of principal stresses in Fig. 3.11 (compare Fig. 3.11a with Fig. 3.11b). After cracking, the tensile force is carried by the reinforcement, and large compressive stresses develop in the diagonal. This is in agreement with the theoretical model, shown in Fig. 3.11c. In the experiments these stresses cause the splitting tensile stresses at the bend of the tensile reinforcement perpendicular to the plane of bar curvature. Due to the two-dimensional modelling of the problem, splitting cannot occur here. In experiments the appearance of cracks in the joint is not reported as a sudden phenomenon, but rather seems to occur

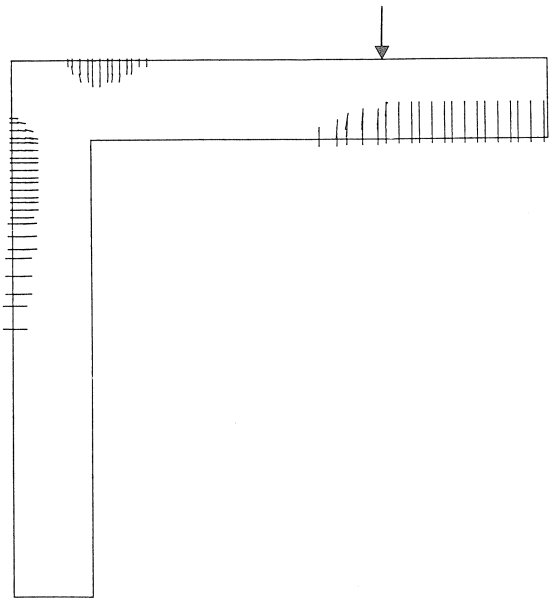

Fig. 3.9. All cracks at load level 8 kN.

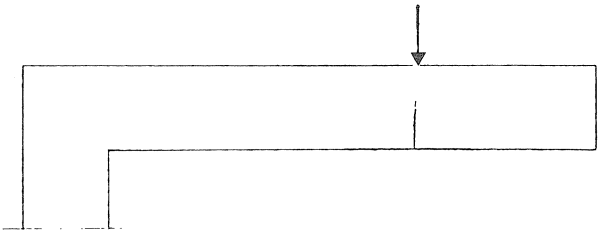

Fig. 3.10a. Cracks (strains $> \varepsilon_u$) at load level 16.9 kN.

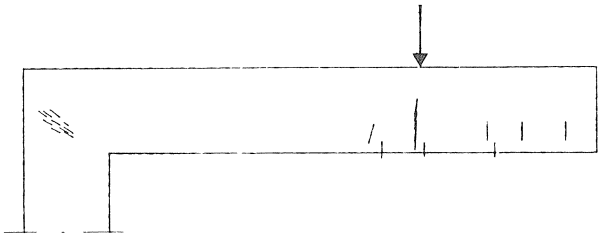

Fig. 3.10b. Cracks (strains $> \varepsilon_u$) at load level 17.9 kN.

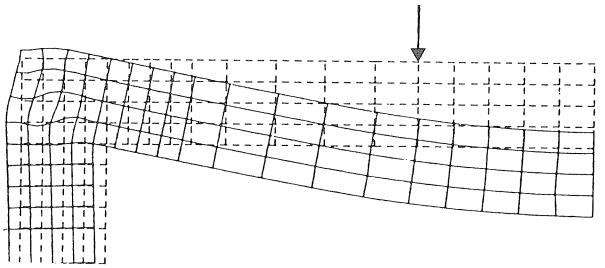

Fig. 3.10c. Incremental displacements at load level 17.9 kN.

more gradually. The sudden appearance of the localized corner crack may be the result of the two-dimensional schematization.

At a load level of 24.4 kN, before the joints fails, the reinforcement in the beam starts yielding. The frame can still take more weight, since the joint has not yet failed.

The joint as well as the complete frame fail at the load level of 26.8 kN. The cracks at failure are shown in Fig. 3.12a (crack strains larger than $\varepsilon_u$) and can be compared with a crack pattern reported by Stroband and Kolpa (Fig. 3.12b).

Failure is initiated due to yielding of the tensile reinforcement in the joint, as indicated by the triangles in Fig. 3.13b. At this stage also plasticity in the inner corner of the joint occurs as well as in the compressive zone of the beam (Fig. 3.13a). The principal stresses at this stage are shown in Fig. 3.14 and clearly indicate the development of a compressive strut in the joint.

If the reinforcement is detailed differently, failure of the compressive diagonal may occur. This (or the formation of splitting cracks) may cause premature failure of the joint. As soon as the reinforcement starts yielding, equilibrium is no longer possible, and the frame collapses.

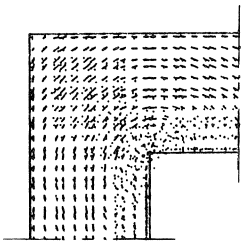

Fig. 3.11a.
Principal stresses,
load level 16.9 kN.

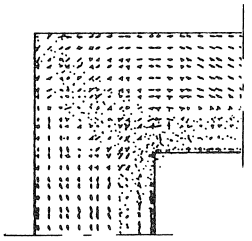

Fig. 3.11b.
Principal stresses,
load level 17.9 kN.

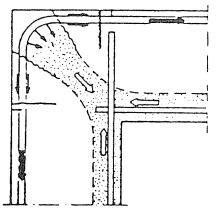

Fig. 3.11c.
Theoretical model
derived from experiments.

From the horizontal support reaction ($F_h$) and the vertical support reaction ($F_u$) we can simply estimate the ultimate moment in the critical sections (of course it is also possible to estimate the moment from the stresses in the integration points in a section):
For Section II we find:

$$M_u = F_h * l,$$

where $l$ is the vertical distance from Section II to the support.
For Section I we find:

$$M_u = F_h * l_t - F_v * d$$

where $d$ is the horizontal distance from Section I to the support. For $l_t$ see Fig. 3.2. With

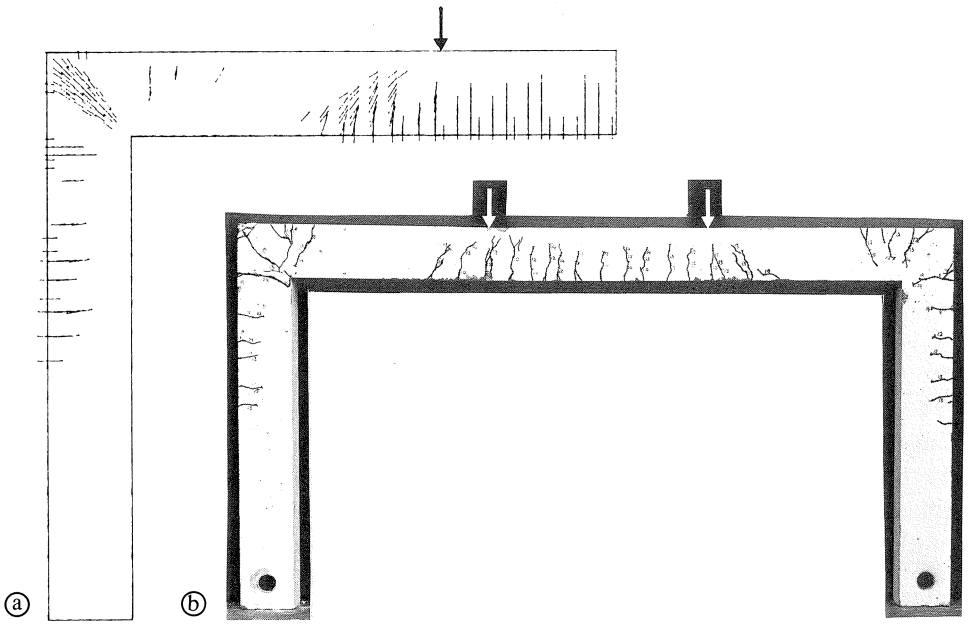


Fig. 3.12a. Cracks (strains $> \varepsilon_u$) at failure ($P_t = 26.8$ kN).

Fig. 3.12b. Experimentally observed crack pattern at failure (Stroband and Kolpa, 1983).

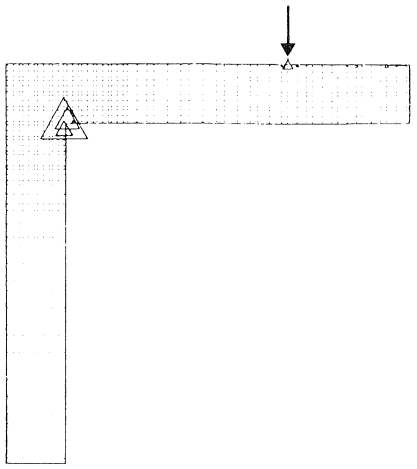

Fig. 3.13a. Concrete plasticity at failure.

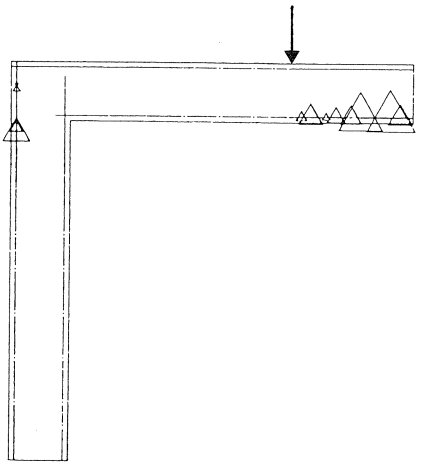

Fig. 3.13b. Reinforcement plasticity at failure.

a horizontal support reaction at failure of the beam (yielding of the reinforcement of the beam) of $F_h = 4.4$ kN and a vertical support reaction of $F_v = 0.5 * P_t = 12.2$ kN, $l_t = 0.750$ m, $d = 0.049$ m we find for Section I: $M_u = 2.70$ kNm. The efficiency of the joint for Section I (the beam), as defined in 3.2, can be computed:

$$\xi = \left\{\frac{2.70}{2.69}\right\} * 100\% = 100\%$$

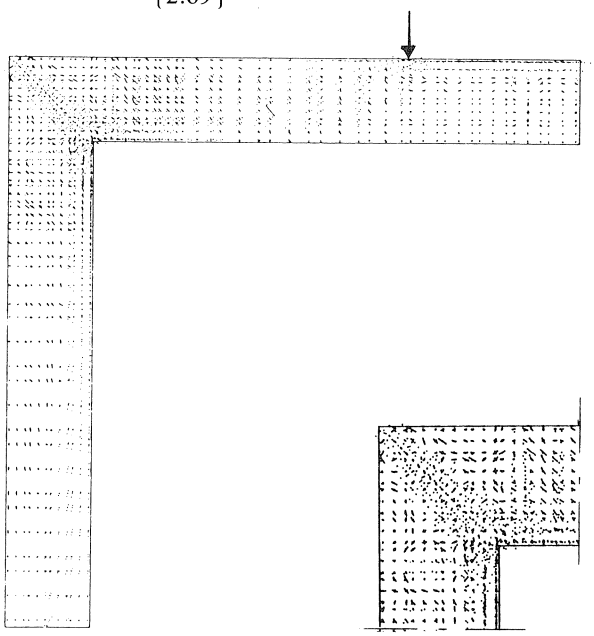

Fig. 3.14a.
Principal stresses at failure.



Fig. 3.14b.
Detail of the corner.

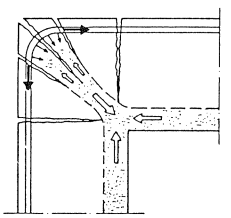

Fig. 3.14c.
Theoretical model
derived from experiments.

For the column we find a horizontal support reaction at failure (yielding of the reinforcement of the column) of $F_h = 5.0$ kN and $l = 0.701$ m. We find also for Section II: $M_u = 3.55$ kNm. The efficiency of the joint for Section I (the beam), as defined in 3.2, can be computed:

$$\xi = \left\{\frac{3.55}{2.96}\right\} * 100\% = 120\%$$

The efficiency of the joint is the larger of the values, i.e. $\xi = 120\%$.

### 3.5 *Discussion*

In the numerical analysis, a relatively course mesh with only four elements over the width of the frame was used, implying that there are in fact two stiff elements (the stiffness of the reinforcement is superimposed on the stiffness of the element) near the edges and two weaker elements in the middle. This causes the open cracks (around the load-level of 17 kN, Fig. 3.10b) not to start at the edges, but in the middle, which may be a reason for the sudden crack opening at a load level of around 17 kN.
From a simple analysis it is found that the compressive zone (at failure) is a mere 15 mm high, and extends only over one or two integration points. A preliminary analysis was carried out without assuming a higher compressive value of the three elements in the inner corner of the joint. At the load level of 17 kN, after opening of the cracks, simultaneously plasticity occurred in the corner elements. The occurrence of plasticity at this load level seems unrealistic, and by considering the three-dimensional stress distribution a higher compressive strength was assumed for the three corner elements. It should be mentioned again that the Mohr-Coulomb failure criterion considerably underestimates the strength of the concrete under three-dimensional states of (compressive) stress. Having regard to the failure load obtained from a simple manual calculation, a 50% higher value was chosen.
With a refined mesh the above-mentioned problems might give less trouble. Only one integration point representing the compressive zone is, of course, not sufficient to give a realistic simulation of the large stress-gradient. However, the result is still acceptable, depending on the purpose of the analysis. An analysis with a course mesh can be made before refining. After such an analysis it might be possible only to refine the mesh of a detail, such as the joint in this example. Also, one might consider carrying out a three-dimensional analysis and modelling the influence of the radius of the curved reinforcing bar, which can be the main cause for splitting in the corner and failure of the joint at a lower load level. However, it should be mentioned that there is no experience with modelling of curved reinforcing bars and hooks.

### 3.6 *Conclusions*

- This two-dimensional analysis was carried out in order to obtain an idea of the *overall* behaviour of the frame and, especially, of the joint.

- The numerical simulation gave a good idea of the structural mechanism in the joint.
- For more detailed research, for example investigating the influence of the concrete quality or the curvature of the reinforcing bar in the joint, a full three-dimensional analysis would be required.

## 4 Tunnel section

### 4.1 *Introduction*

Most of the examples in this report relate to numerical simulations of laboratory experiments. Such cases are illustrative in that the numerical results can be directly compared with the available experimental results, so that assumptions and conjectures can then always be subsequently verified.
Matters are very different when actual problems as encountered in practice are analysed. Feedback of data for comparison with experimental results is not possible in such cases, and the possibilities of checking are limited to carrying out approximate manual calculations. Obviously, the designer must then place full confidence in having made safe and justified choices with regard to the material parameters and boundary conditions for the numerical calculation. Incorrect choices are difficult to rectify and may have disastrous consequences.
The example presented in this chapter relates to a practical problem of this kind, namely, a detail of an existing reinforced concrete tunnel structure in another country. The problem associated with this structure was submitted to consultancy in the Netherlands. This led to a numerical analysis of, among other features, the shear capacity and the bond. Some key results of this analysis will be reported here.
Since the influence of material parameters has already been illustrated in connection with the other examples, the emphasis will here be on the influence of the assumed boundary conditions of the problem, which are liable to be just as important.

### 4.2 *Description of the problem*

Fig. 4.1 shows the principal geometric data of the tunnel cross-section, comprising two traffic lanes.
The first decision to be taken relates to the question as to what part of the structure is to be dealt with by nonlinear analysis. After all, in the present state of the art of computer hardware a nonlinear analysis of the complete cross-section is a rather time-consuming and expensive operation. To obtain a reliable solution it quite soon becomes necessary to work with four plane-strain elements through the thickness of the roof, the walls and the floors. Bearing in mind, too, that the length/width ratio of such elements should preferably be not greater than 4, this would mean that the analysis of the whole cross-section would involve many hundreds of elements, which is impracticable with present facilities.

It is, however, possible to carry out a linear-elastic preliminary analysis of the complete structure. On the basis of such an analysis the most critical member or part of the structure is pinpointed, and the nonlinear analysis is then confined to this critical part. A preliminary analysis of this kind is relatively simple and, if beam elements are used, yields as its result the bending moment diagrams, shear diagrams and normal (or direct) force diagrams. In the case of the present problem this information led to the inference that the connection of the tunnel roof to the intermediate wall was the most critical feature, and for this reason the nonlinear detailed analysis was confined to the part shown shaded in Fig. 4.1.

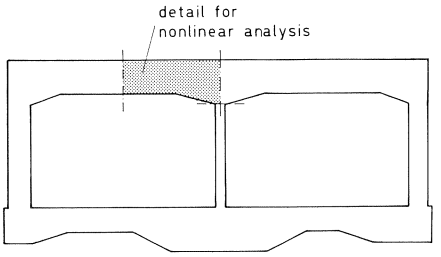


Fig. 4.1. Cross-section of tunnel structure.

## 4.3 *Modelling of the problem*

The structural detail to be analysed and the finite element mesh adopted for the purpose are shown in Figs. 4.2 and 4.3. Because a plane-strain state exists in the deep-lying middle part of a tunnel structure, plane-strain elements were employed. In this case they were eight-node isoparametric quadratic elements, numerically integrated with the aid of the 3 by 3 Gaussian scheme.

The structural detail contains various reinforcing bars, and it is to be noted that the top reinforcement comprising a lapped splice could constitute a weak link. Besides, the top

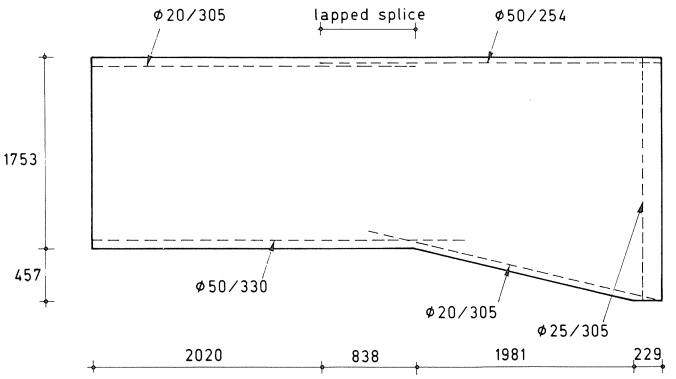


Fig. 4.2. Detail of cross-section for nonlinear analysis. Dimensions in mm. Reinforcement ø 20/305 means 20 mm diameter reinforcing bars, 305 mm centre-to-centre.

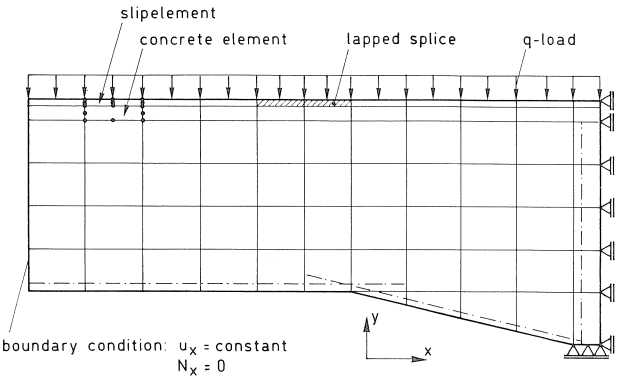


Fig. 4.3. Finite element mesh. Reinforcing bars with perfect bond are indicated by dash-dot lines. The top reinforcement is modelled by separate bond-slip elements.

reinforcement consists of plain bars with the unusually large diameter of 50 mm, with only 50 mm concrete cover. For this reason it was decided to make a detailed study of the bond of this reinforcement by means of special slip elements developed for the purpose. A nine-node slip element was employed, with which the slip layer above the reinforcement and the slip layer below the reinforcement were represented separately. At the lapped splice, overlapping slip elements were employed, so that any pull-out of one of the bars could be simulated. The other reinforcing bars are "embedded" in the concrete elements in the usual way (perfect bond).

Two loading cases were considered: dead weight and uniformly distributed vertical load. First the dead weight was added and then the uniformly distributed load was incrementally increased to failure.

If the nonlinear analysis is, in order to save CPU time, confined to a detail of the structure, this means accepting that the rest of the structure will have to be replaced by realistic boundary conditions. From the bending moment diagram of the linear-elastic preliminary analysis it was apparent that the tunnel behaved in a substantially symmetric manner in relation to the intermediate wall. For this reason an ordinary restraint, indicated by roller bearings, was assumed at the intermediate wall (at the support, on the right in Fig. 4.2). Choosing a boundary condition at midspan (on the left in Fig. 4.2) was more difficult. The following was adopted:

boundary condition for span: $u_x = \text{constant}$

$$N_x = 0$$

The first condition implies that the span cross-section remains straight and vertical (i.e., cannot rotate), but can as a whole undergo a free horizontal displacement. This boundary condition has been introduced by making use of a special tying option with which dependence relations for degrees of freedom are introduced. Here the $u_x$ of all the nodes at the midspan section has been equated ("tied") to the $u_x$ of the bottom node at this section. The effect of the tyings is shown in Fig. 4.4, where the deformed structure is represented.

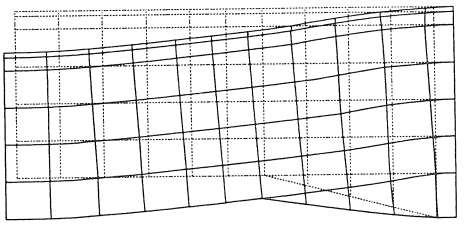

Fig. 4.4. Typical deformed mesh (dashed lines). Tyings compel the midspan section to remain plane and vertical. In the horizontal direction the midspan section is free to displace.

The second condition means that the resultant external normal force $N$ in the tunnel roof is equated to zero, which can be conceived as a safe lower bound approximation, because in reality the horizontal earth and water pressure acting on the side walls of the tunnel will produce a normal force in the roof. This normal force will accentuate the development of a stiffening thrust arch in the roof, which will result in an increased failure load. This will be further considered in Section 4.5.
The complete set of material parameters is given below. For most of the parameters safe lower bounds (design values) have been adopted. The extremely low values for the properties of the concrete may appear strange, but are due to the fact that the tunnel was constructed of only a moderately good grade of concrete. Because the structure has only a limited number of dominant reinforcing bars, the $G_f$ concept was used for the determination of $\varepsilon_u$.

*Concrete*
$E_c = 6640$ N/mm$^2$
$\nu = 0.2$
$f_{cc} = 20$ N/mm$^2$
$f_{ct} = 1.2$ N/mm$^2$
tension cut-off 1
$G_f = 60$ N/m
$h = 100$ mm
$\varepsilon_u = 0.001$
$\beta = 0.20$

*Reinforcing steel*
$E_s = 210000$ N/mm$^2$
$f_{sy} = 220$ N/mm$^2$

*Bond-slip* (see Fig. 0.10)
$S^z = 200$ N/mm$^2$
$\tau_{zu} = 1.2$ N/mm$^2$
$S^r = 20000$ N/mm$^2$

## 4.4 *Results*

During the course of the analysis the load-displacement behaviour for the midspan section was plotted as represented in Fig. 4.5.
The first nonlinearity in this diagram is due to cracking over the support. Next, yielding of the top reinforcement over the support occurs, as a result of which the nonlinearity rapidly increases. In this phase, diagonal shear cracks are formed and there occurs slip between the top reinforcement and the concrete. Despite this damage, the structure is still capable, thanks to redistribution, of resisting further load. Finally, a "ductile"

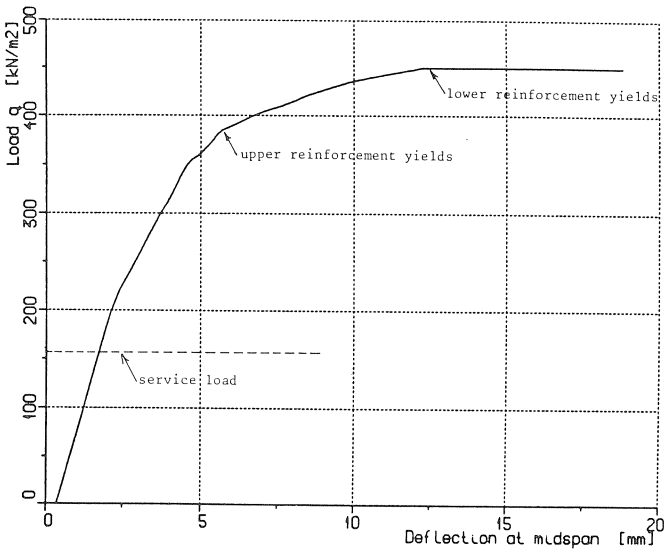


Fig. 4.5. Load versus deflection at midspan.

failure plateau is attained when the bottom reinforcement at midspan also begins to yield. From that instant onwards the redistribution reserve of the structure is exhausted because the failure moment both over the support and at midspan has been mobilized. The safety margin of the failure load with respect to the actual service load on the structure (earth and water pressure) is found to correspond to a factor of 2.9, as indicated in Fig. 4.5.

Finding the failure load, however, was not the most surprising feature of this analysis, since a simple manual calculation would have given the same result. Of greater interest was the qualitative information that the numerical analysis supplied with regard to such matters as cracking patterns, deformations, stress trajectories and the bond behaviour at the lapped splice. Some idea of these features is given by Figs. 4.6 to 4.10.

Fig. 4.6 shows the development of cracking. First, vertical flexural cracks are formed over the support, but with increasing magnitude of the load, diagonal shear cracks are predicted which rapidly increase in number and importance. The deformed element mesh at failure suggests a kind of shearing mechanism along these cracks (Fig. 4.7).

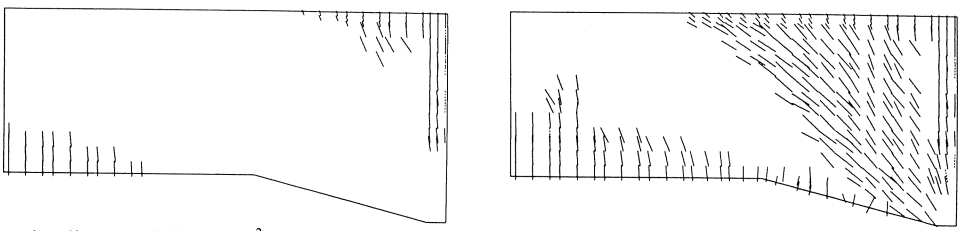

a. loading $q = 300$ kN/m$^2$ b. loading $q = 450$ kN/m$^2$ (failure)

Fig. 4.6. Crack formation with increasing load.

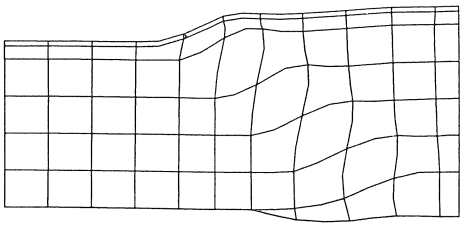

Fig. 4.7. Incremental deformations at failure ($q = 450$ kN/m$^2$).

The concrete stress trajectories in Fig. 4.8 demonstrate the possibility of simulating the redistribution of stresses in a structure by means of nonlinear calculations. In this diagram the stress trajectories in the linear-elastic stage are compared with those in the ultimate stage, i.e., at failure. In the linear-elastic stage the tensile concrete stresses are found still to make a substantial contribution to the transfer of shear force. At failure, on the other hand, the tensile stresses have entirely disappeared (because of cracking), and a pronounced thrust arch can be observed which equilibrates the mid-span tensile reinforcement. The action of such a tied-arch equilibrium system is limited either by yielding of the tensile reinforcement or by crushing of the concrete in compression. In this case the reinforcement was the governing feature; the compressive stresses in the thrust arch remained well within the Mohr-Coulomb yield contour. In this context it is to be noted that a three-dimensional state of stress (plane-strain) existed in the tunnel roof. The third stress component ensured that the Mohr-Coulomb criterion was even more conservative than in the case of a two-dimensional state of stress, so that safety with respect to compressive failure was certainly assured.
Another result was the behaviour of the steel stress in the top reinforcement with increasing load, as indicated in Fig. 9. At failure the lapped splice is suddenly subjected to a large force. This numerical result is in agreement with the theory of the "displaced bending moment diagram" envisaged in the Netherlands Code of Practice for Concrete (VB '74). In this context it is interesting to mention that the numerical tool can also be used to optimize the design codes. Theories embodied in the codes are based on simple and sometimes conservative assumptions, whereas a numerical model tries to choose

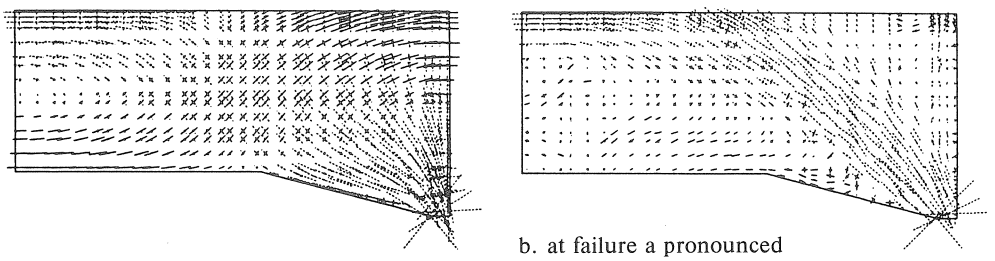

a. linear-elastic stage

b. at failure a pronounced compressive arch occurs

Fig. 4.8. Stress redistributions. Compressive stresses are indicated by dotted line segments and tensile stresses by solid line segments.

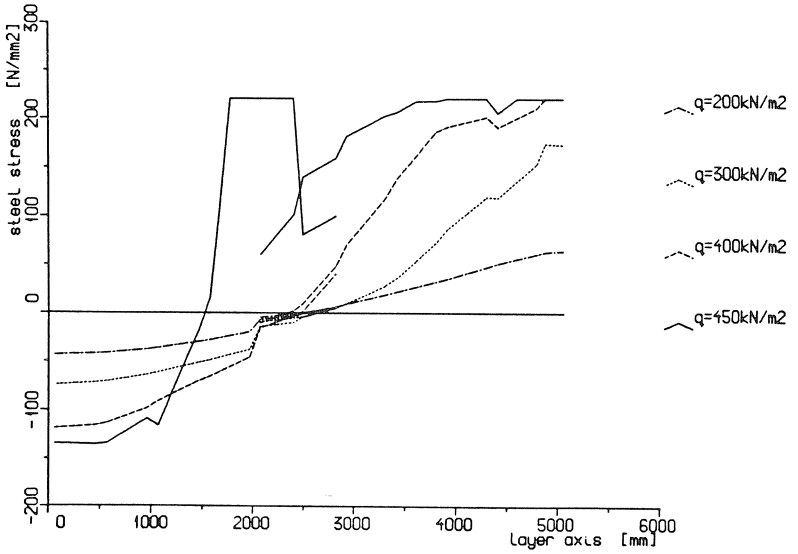


Fig. 4.9. Steel stresses in top reinforcement (compare Figs. 4.2 and 4.3) with increasing load. Note that the lapped spice is subjected to tension at failure.

its starting point in an as realistic a model as possible of the material, which is formulated on the basis of experimental research.
Fig. 4.10 gives some idea of the behaviour of the bond stress along the top reinforcement. At failure the maximum bond stress $\tau_{zu}$ is found to have been mobilized along a major part of that reinforcement. The marked discontinuities in the diagram are due to the presence of cracks.

## 4.5 *Effect of boundary conditions*

Besides the material parameters, the assumed boundary conditions of the problem may considerably affect the final result. In the first analysis reported above, the boundary condition adopted at midspan was (see Section 4.2):

analysis (a): $u_x = \text{constant (free)}$
$N_x = 0$

The opposite condition consists in preventing the displacements, but allowing the horizontal force to increase arbitrarily and unlimitedly:

analysis (d): $u_x = 0$
$N_x = \text{free}$

This condition implies that a standard restraint by means of roller bearings is applied here, just as at the support. The tyings at midspan are then not used.
Besides these two extremes, two intermediate forms were studied: analyses (b) and (c).

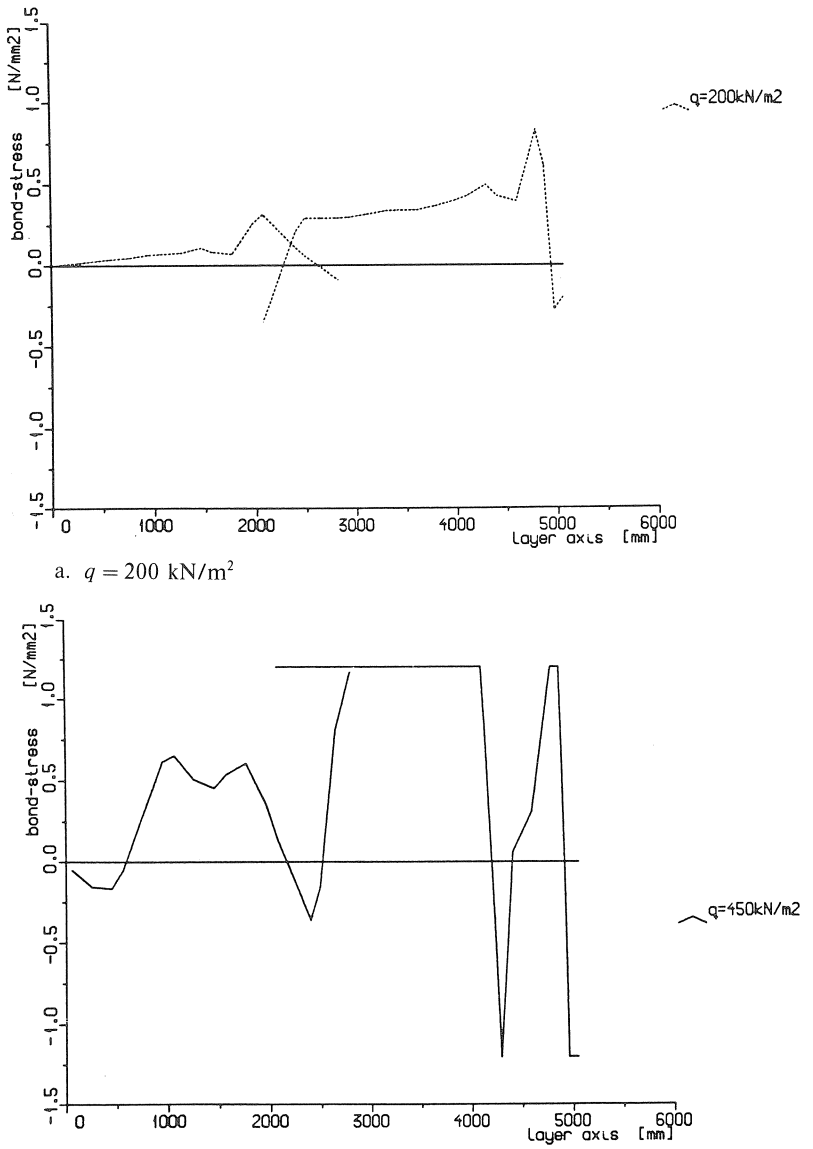


a. $q = 200$ kN/m$^2$

b. $q = 450$ kN/m$^2$ (failure)

Fig. 4.10. Tangential bond stresses along top reinforcement with increasing load.

In these the horizontal force was steadily increased with the vertical load, this perhaps being the most realistic representation of earth and water pressure. In analysis (b) the horizontal force was held constant when it had reached a particular limit which corresponded to the compressive force actually occurring in the tunnel roof at service load. The load-deflection diagrams for the two extremes (a) and (d) and for the two intermediate cases (b) and (c) are shown in Fig. 4.11. The variations in the boundary con-

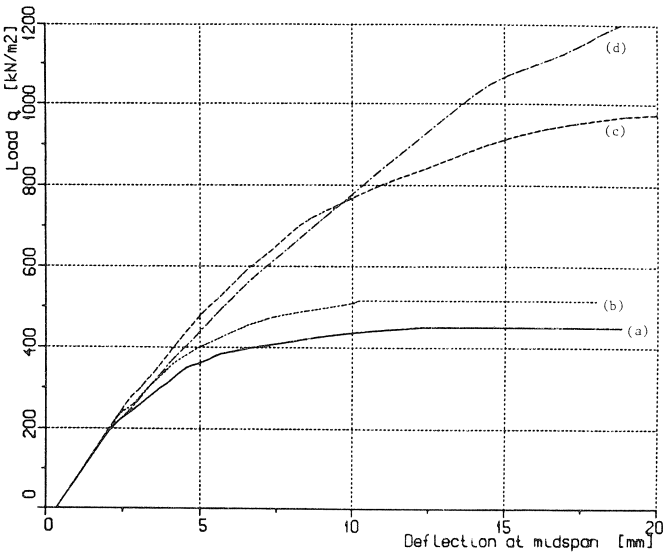


Fig. 4.11. Effect of boundary conditions on load-deflection curve.
(a) $u_{z,\text{field}} = \text{free}$, $N_z = 0$
(b) $u_{z,\text{field}} = 0$, $N_z = \text{free}$
Analysis (a) can be regarded as a lower bound and analysis (d) as un upper bound. (b) and (c) correspond to boundary conditions in between the two extremes.

ditions adopted are found to have a very considerable influence. Analysis (a) can be conceived as a lower bound and analysis (d) as an upper bound.
For the upper bound analysis (d) the crack patterns, deformations and principal stress trajectories are shown in Fig. 4.12. The location of the diagonal crack is found to have changed, and the thrust arch has spread over a much wider region than in analysis (a) (cf. Fig. 4.8). Analysis (d) was not even continued to failure, but was stopped at the

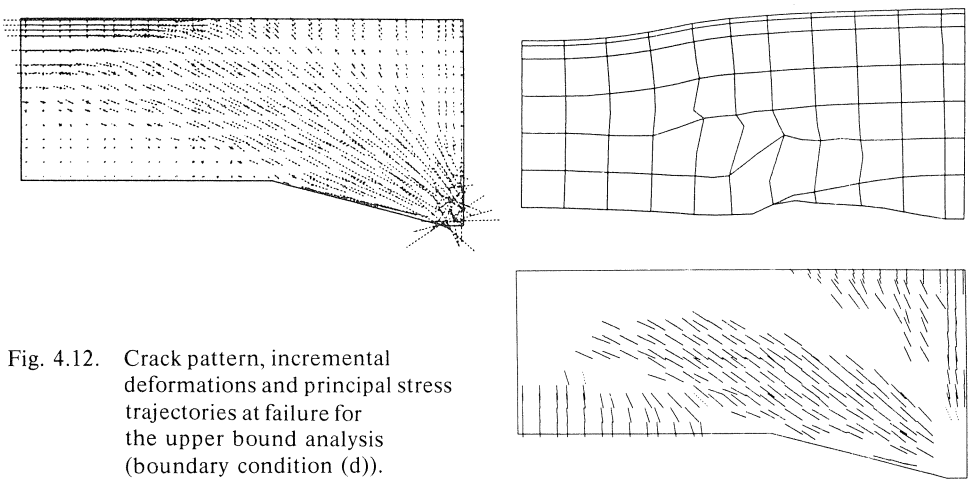

Fig. 4.12. Crack pattern, incremental deformations and principal stress trajectories at failure for the upper bound analysis (boundary condition (d)).

instant when excessive diagonal cracking developed. Actually, the load could have been further increased until the compressive concrete stresses in the arch attained the Mohr-Coulomb yield contour. In that case a very high failure load would have been arrived at, this being due to the fact that the problem region is, as it were, "confined" when the midspan section is deprived of the possibility of free displacement. Then the thrust arch in the concrete, not the tie member formed by the reinforcement, is the governing feature.

### 4.6 *Discussion*

Without going into details concerning the further causes of the differences, it is nevertheless evident that considerable care should be bestowed on determining the boundary conditions.
From this tunnel analysis is has emerged that DIANA offers good possibilities for taking account of boundary conditions. Particularly the "tying" option is popular with numerical analysers because it enables them to apply all sorts of simplifications in the geometric modelling of the problem. The use of linear or nonlinear springs is another extensively used means of replacing large structural members or parts by suitable boundary conditions. The flexural stiffness of beams, columns or walls in the vicinity of the detail can thus be replaced by a rotational spring, and the axial stiffness thereof by a translational spring.
It is furthermore to be noted that in basing the boundary conditions on the results of a linear-elastic preliminary analysis it is likewise necessary to be careful, because the moment distributions, etc. obtained from that analysis are valid only for the linear-elastic case, but it is implicitly presumed that they are valid also for the nonlinear case. If drastic redistribution occurs, this will not necessarily be a realistic assumption. However, in view of the tremendous rate of development in computer hardware and software (more rapid solution procedures!) the problem of choosing boundary conditions will dwindle in importance because it will be possible to include an increasingly large part of the structure in the non-linear analysis.

### 4.7 *Conclusions*

The nonlinear detail analysis of an existing tunnel structure with the aid of DIANA supports the following conclusions:
- The development of vertical flexural cracks and diagonal shear cracks can be predicted reasonably well in a qualitative way.
- Redistribution of stresses is predicted surprisingly well. At failure a pronounced thrust arch is observed in the concrete and is in equilibrium with the midspan tensile reinforcement.
- Bond-slip elements prove to be a suitable tool for studying the bond of reinforcement in reinforced concrete, even if lapped splices are present.

- DIANA offers good possibilities for replacing structural parts which are of no particular interest by realistic boundary conditions. The choices for these conditions may have a major influence on the final result.

## 5 Two reinforced concrete panels

Deep beams are usually analyzed on the assumption of linear-elastic behaviour. The behaviour after cracking is difficult to estimate,especially when deep beams continuous over several supports are considered. Based on an extensive experimental investigation by Leonhardt and Walther in 1966, recommendations for the design and construction of deep beams on two or three supports were determined. The non-linear numerical tool can also be applied for analyzing the structural behaviour of such in-plane loaded panels. In this example, two of the panels tested by Leonhardt and Walther (1966), have been simulated numerically. The first example comprises the analysis of a deep beam on two supports; in the second example a deep beam on three supports is simulated numerically. In both cases, the results of the analysis are compared with the experimental results.

### 5.1 *Deep beam on two supports*

#### 5.1.1 Introduction

From the nine single-span deep beams tested by Leonhardt and Walther, beam WT3 has been chosen for analysis. This particular beam was chosen because structural failure occurs due to compressive failure of the concrete near the supports. This was considered an interesting extension of the other examples, in which mostly tensile and shear fractures are the dominant mechanisms.

#### 5.1.2 Description of the experiment

Details of the loading procedure and the specimen (WT3) are shown in Fig. 5.1. In Fig. 5.1a the dimensions of the deep beam are given, as well as details of the reinforcement. WT3 is a single-span beam 1600 mm × 1600 mm in size. The thickness of the panel is 100 mm and it is loaded by a distributed load along the upper edge as indicated in Fig. 5.1b. Details of the supports are shown in the same diagram: two steel platens on roller bearings are used. A thin layer of mortar was placed between the beam and the steel loading platen as well as between the beam and the supporting steel platens. The entire structure was loaded in a 5 MN compressive testing apparatus. Load was applied in steps of 100 kN, after which measurements were taken (which lasted approximately 40 min.).
Eight 8 mm diameter reinforcing bars were installed in four layers in the lower part of the beam. Furthermore, a square grid of 5 mm bars was placed over the entire panel (see Fig. 5.1a).

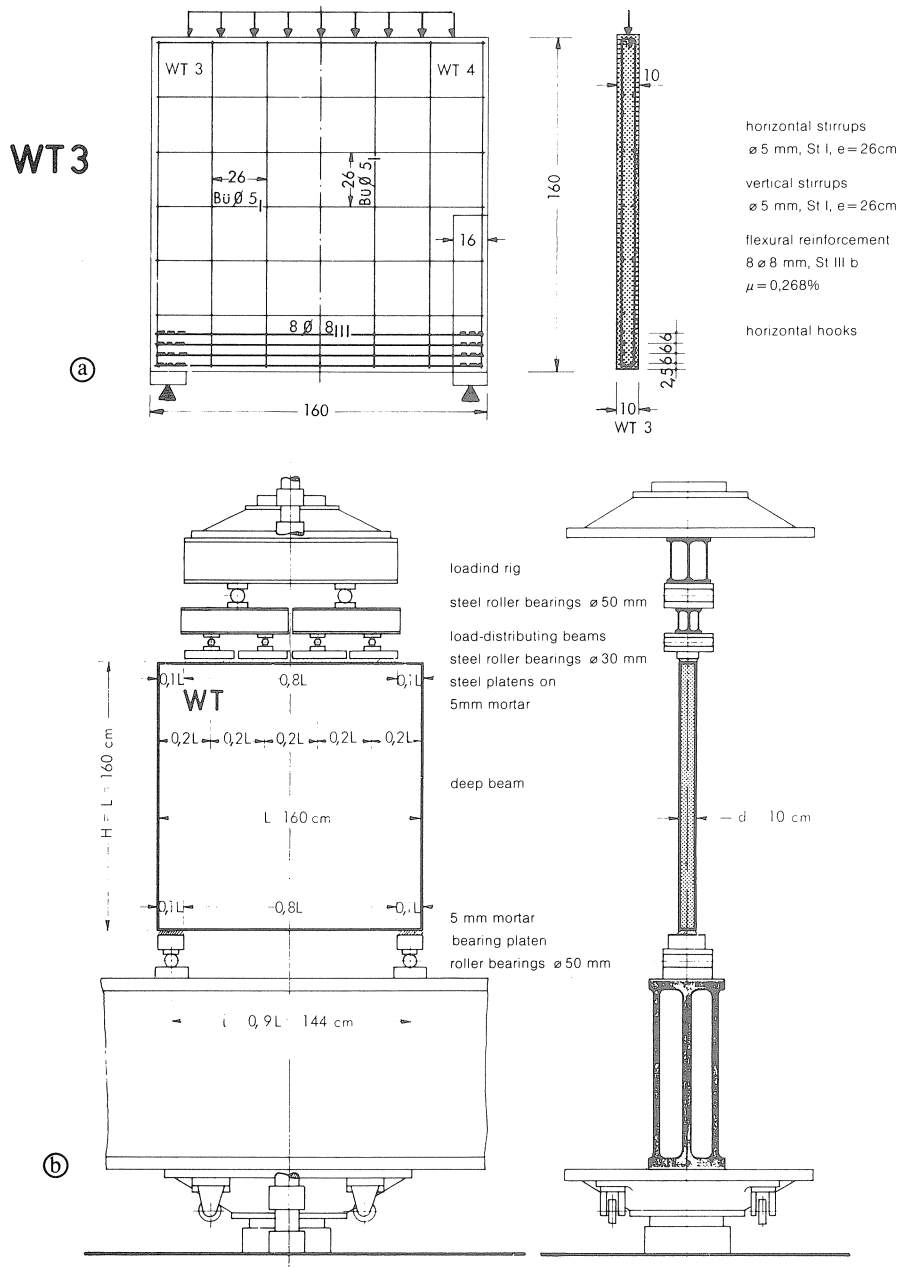


Fig. 5.1. Reinforced concrete panel WT3, dimensions and reinforcement details (a), and test set-up (b).

Results of the experiments are shown in Figs. 5.2 to 5.4. The moment-deflection curve is shown in Fig. 5.2, together with some of the results of the other beams that were tested in the same program. Fig. 5.3 shows the crack pattern after failure of the beam. The

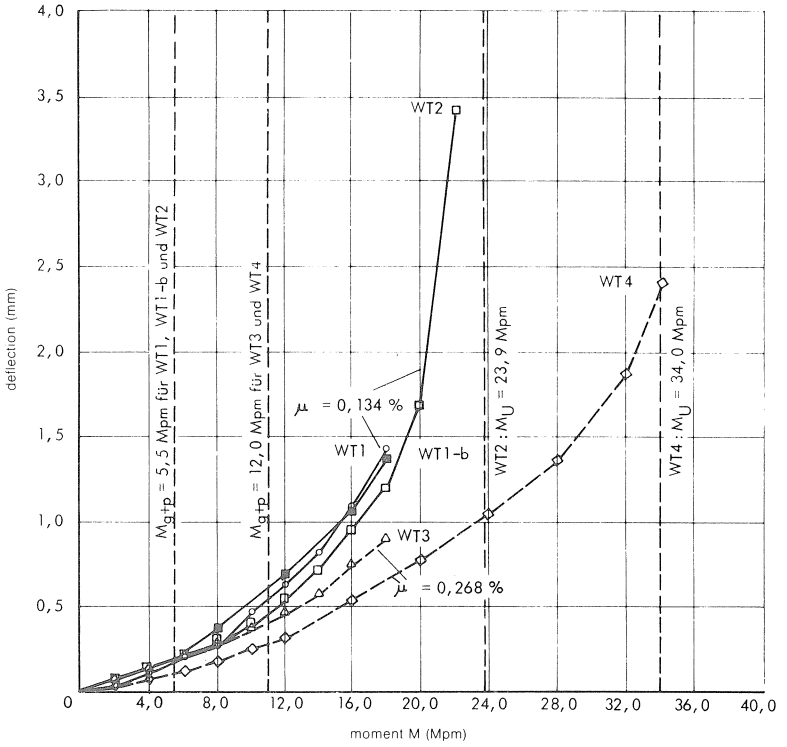


Fig. 5.2. Experimental results, moment-deflection curves at mid-span.

concrete over the left support failed at $P_t = 1000$ kN. This part of the beam was reinforced by confining the concrete between two steel platens, and after these steel platens were fixed, the external load could be increased again, until the right support failed at $P_t = 1290$ kN. Finally, in Fig. 5.4, the steel stresses in the lower reinforcement bar are shown. The steel stresses were determined over the supports and the middle of the beam, and can therefore serve only as an indication. As will be shown in the subsequent sections, a much more detailed distribution of steel stresses was obtained from the analysis.

### 5.1.3 Parameters for the analysis

The panel could realistically be schematized as a plane stress case. In the following the element discretization is shown, and the parameters for the analysis are mentioned.

#### 5.1.3.1 Element discretization

The element mesh adopted is shown in Fig. 5.5. Due to symmetry only one half of the complete structure has to be modelled. Again the eight-noded quadratic isoparametric

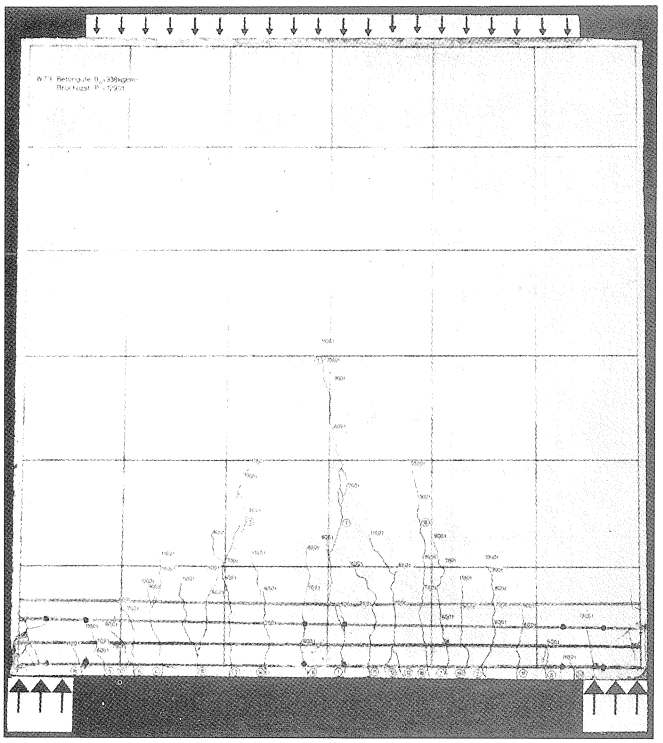

Fig. 5.3. Cracking observed in the experiment.

elements have been used. The support platen has also been modelled, and the mesh is refined over the support. This was done because in general it is rather unfavourable to define a support in a middle node. By refining the mesh, the support reaction coincided with the corner nodes as indicated. The support platen was rigidly fixed to the concrete elements, and Poisson's ratio of the support platen was taken as equal to Poisson's ratio of the concrete elements (i.e. $\nu = 0.20$).

Loading was applied to the panel as concentrated loads in the nodes along the upper edge (i.e. the distributed load in the experiment was replaced by a series of concentrated loads). In a preliminary analysis the panel stiffness was found to be overestimated when the loading platens were modelled as similar to the support platens.

The dotted lines in Fig. 5.5 show the locations of the reinforcing bars. Three-noded numerically integrated bar elements were used for the reinforcement. Full bond was assumed between reinforcement and concrete.

### 5.1.3.2 Material parameters

The material parameters used in the analysis are summarized below; the parameters used for modelling the support platens are also included. In Fig. 5.6, both the measured

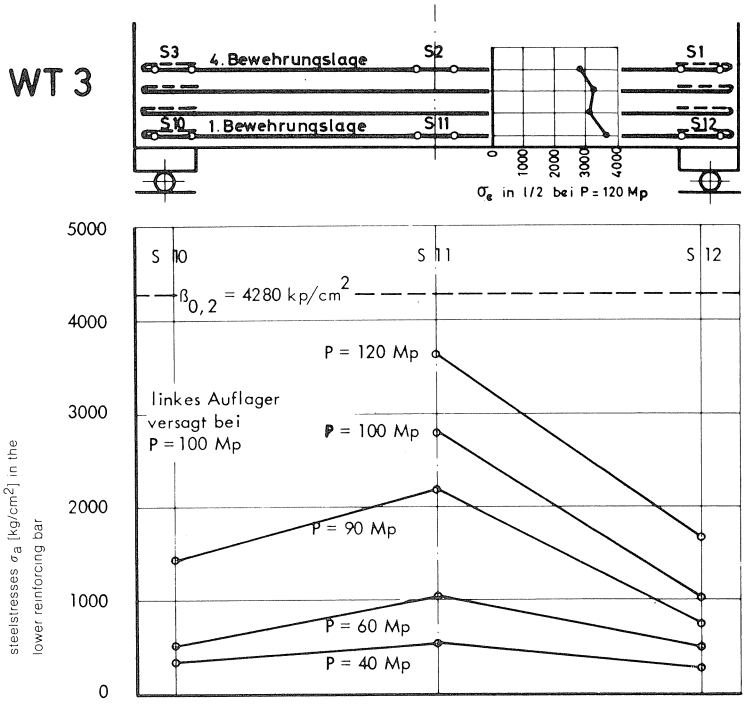


Fig. 5.4. Stresses measured in the lower reinforcing bar.

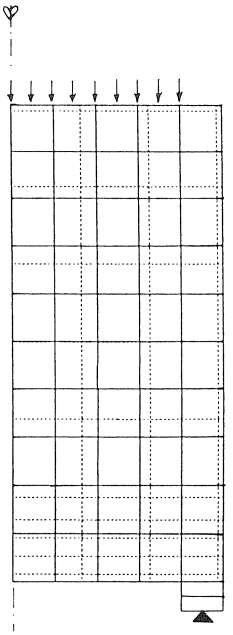

Fig. 5.5. Element discretization; dotted lines indicate the location of the reinforcement bars.

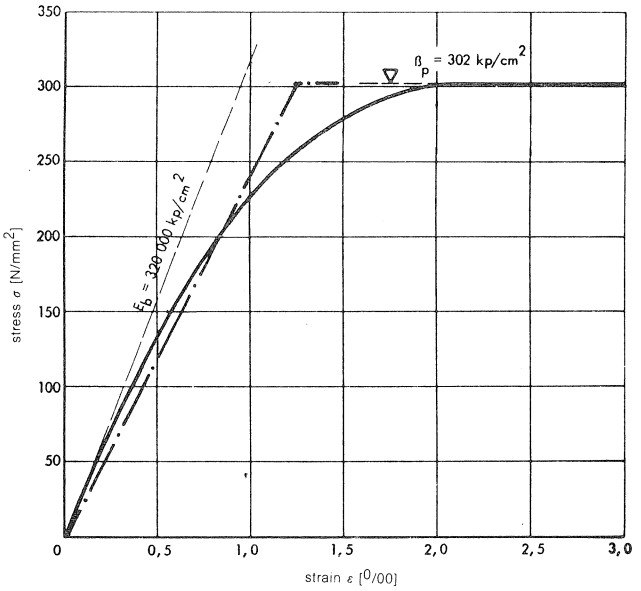


Fig. 5.6. Elasto-plastic model for concrete in compression.

compressive stress-strain curve and the elasto-plastic model are shown. The adopted material models are explained in Chapter 0.

*Concrete*
$E_c = 24000$ N/mm$^2$
$\nu = 0.2$
$f_{ct} = 3.65$ N/mm$^2$
$f_{cc} = 30.2$ N/mm$^2$
tension cut-off 2
$\varepsilon_{us} = 0.0010$
$\beta = 0.20$

*Reinforcing steel*
$E_s = 210000$ N/mm$^2$
$f_{sy} = 400$ N/mm$^2$

*Support platen*
$E_s = 210000$ N/mm$^2$
$\nu = 0.2$

### 5.1.3.3 Analyses performed

Two different analyses were carried out for the deep beam on two supports. The first analysis was performed with $\varepsilon_{us} = 0.0019$; in the second analysis $\varepsilon_{us}$ was taken as 0.001, almost identical with the value adopted in the analysis of the conventionally reinforced tooth of the metro beam (see Chapter 1).

## 5.1.4 Results

In this section mainly the results of the analysis with the low $\varepsilon_{us}$-value (0.001), are reported. Only in load-deflection diagrams and steel stress plots is a comparison made

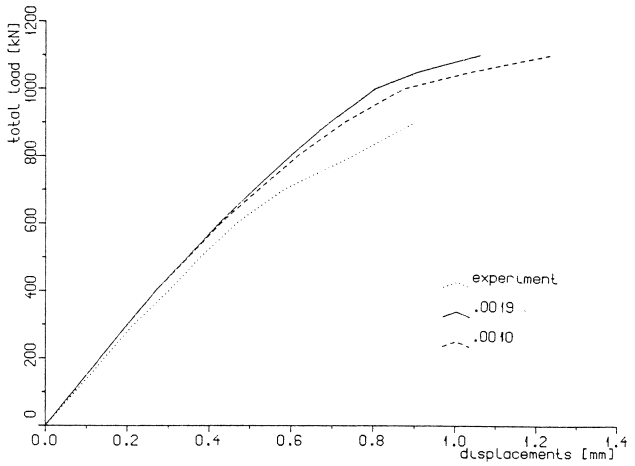


Fig. 5.7. Comparison between calculated and experimental load-deflection curves, influence of tension stiffening parameter $\varepsilon_{us}$.

between the two analyses, and is the influence of the $\varepsilon_{us}$ variation shown. The results of the analysis are shown in Figs. 5.7 to 5.13.

First, in Fig. 5.7, the computed load-deflection diagrams are compared with the experimentally observed behaviour. The failure load of the panel is estimated rather well in the analysis. Experimental values are 1000 kN and 1290 kN for the left and right support respectively. In the analysis, a failure load $P_t = 1100$ kN is computed, which fits nicely between the experimental bounds. In both analyses the stiffness of the panel is clearly overestimated at higher load levels. Reducing $\varepsilon_{us}$ only has a minor effect on the stiffness. As we have seen before in the analysis of the reinforced concrete tooth of the metro viaduct (Chapter 1), a reduction of $\varepsilon_{us}$ leads to increased crack extension.

Plots of the computed crack development for the case $\varepsilon_{us} = 0.001$ are shown in Fig. 5.8.

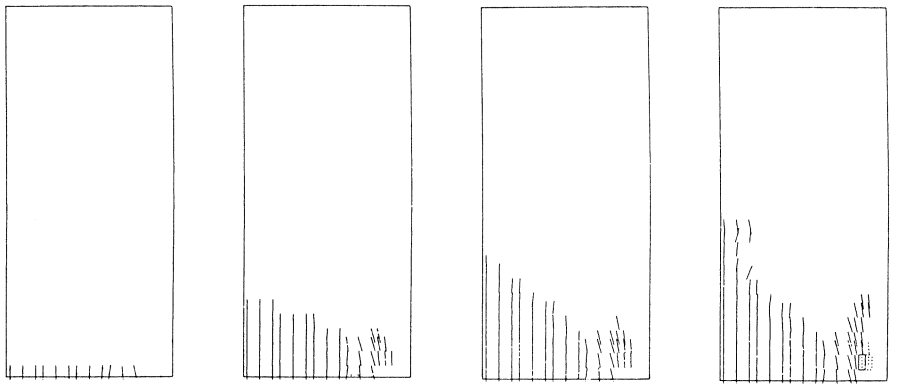

a. $P_t$ = 400 kN b. $P_t$ = 800 kN c. $P_t$ = 1000 kN d. $P_t$ = 1100 kN

Fig. 5.8. Calculated crack development ($\varepsilon_{us} = 0.0010$).

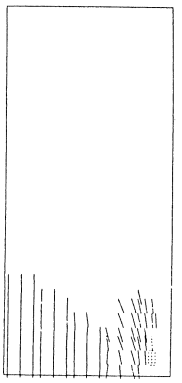

Fig. 5.9. Calculated crack pattern at $P_t = 1100$ kN ($\varepsilon_{us} = 0.0019$).

The cracks are shown at four loading levels; $P_t = 400$, 800, 1000 and 1100 kN respectively. Fig. 5.9 shows the crack pattern observed at $P_t = 1100$ kN in the analysis with $\varepsilon_{us} = 0.0019$. In Fig. 5.10 the principal stresses, computed in the analysis with $\varepsilon_{us} = 0.001$, are shown for four load steps (respectively $P_t = 400, 800, 1000$ and 1100 kN). The incremental deformations for the same load steps are shown in Fig. 5.11, while Fig. 5.12 shows the calculated total deformations.

Finally, the calculated stresses in the lower reinforcing bar are shown in Fig. 5.13. Also the experimental results are indicated in these diagram. In the experiment, steel stresses were measured only at three positions: over both supports and in the middle section of the beam. In Fig. 5.13 only the average result of the steel stresses above the supports is shown, as well as the measured value in the middle section. Unfortunately, no results are available along the rest of the bar. In these diagrams the influence of $\varepsilon_{us}$ is shown (Fig. 5.13a), as well as the effect of increasing the external load (Fig. 5.13b).

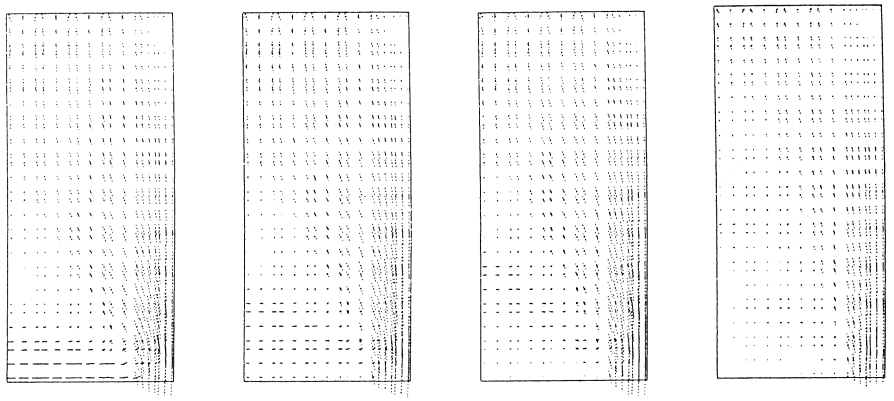

Fig. 5.10. Principal stresses at different loadlevels ($\varepsilon_{us} = 0.0010$).

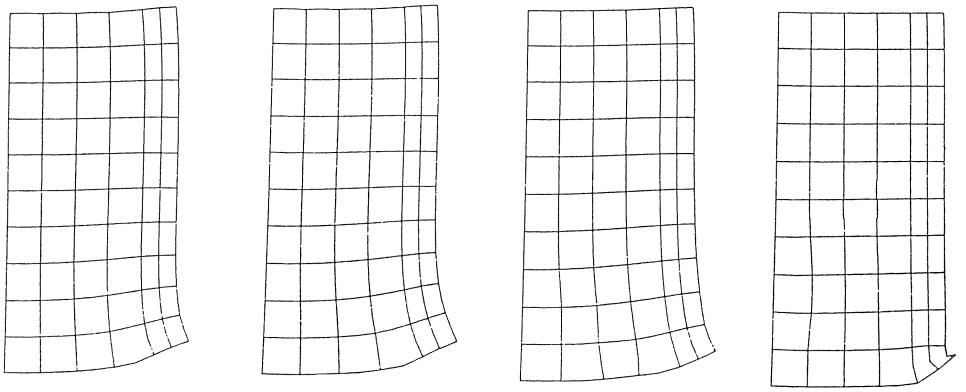

Fig. 5.11. Incremental deformations at subsequent loadlevels ($\varepsilon_{us} = 0.0010$).

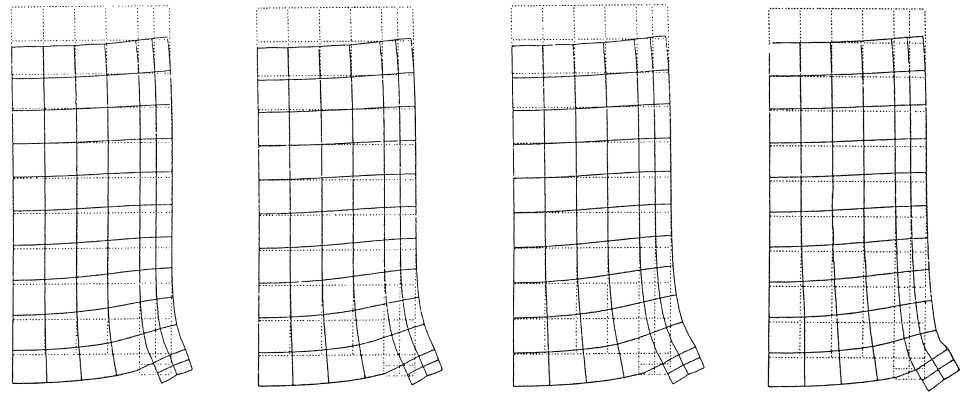


Fig. 5.12. Total deformations at different loadlevels ($\varepsilon_{us} = 0.0010$).

### 5.1.5 Discussion

The expected influence of the variation of $\varepsilon_{us}$ is clearly apparent from the results shown in Fig. 5.8 and 5.9. Increased crack extension occurs when the tension stiffening parameter is reduced (compare Fig. 5.8d with Fig. 5.9). However, the effect on the computed load-deflection curve is only marginal (see Fig. 5.7). Comparison of the computed crack patterns with the experimentally observed crack pattern indicates that a better fit between analysis and experiments is obtained when the tension stiffening parameter is reduced. The diagrams indicate that even a larger reduction of $\varepsilon_{us}$ is needed (compare Figs. 5.3 and 5.8d).

In the analysis a dominant crack develops to the left of the supporting steel platen. This crack is dominant from the beginning, and its development is a direct result of the linear-elastic stress-distribution calculated in the beam. From the incremental deformation plots the dominant character can clearly be seen at the lower load levels

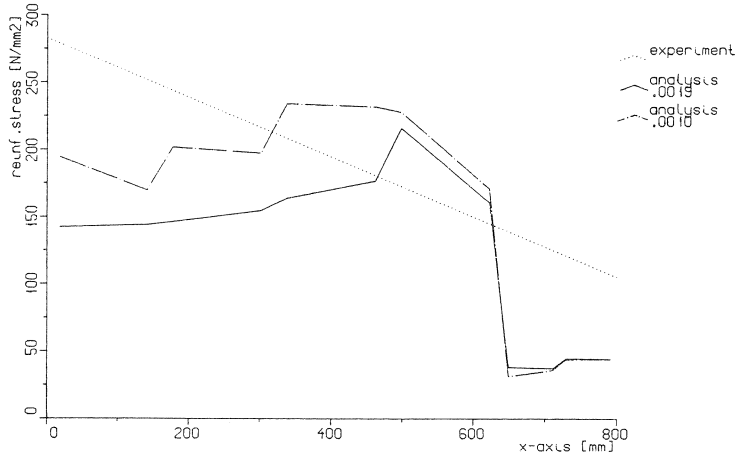


Fig. 5.13a. Influence of the tension stiffening parameter ($\varepsilon_{us}$) on the stress distribution in the lower reinforcing bar at $P_t = 1000$ kN.

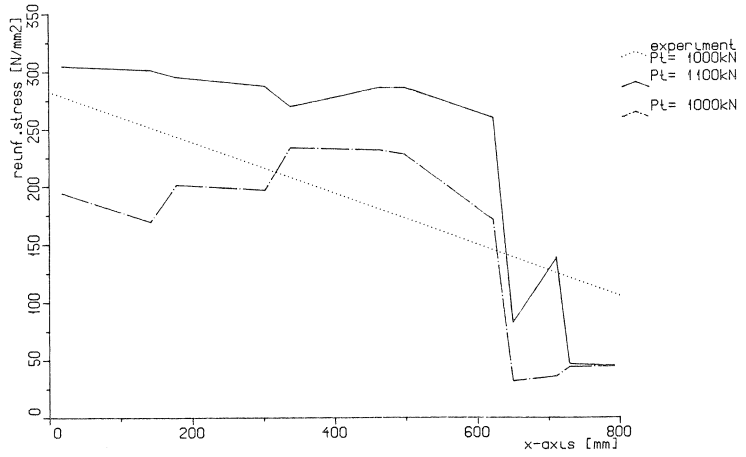


Fig. 5.13b. Stress distribution in the lower reinforcing bar at $P_t = 1000$ and 1100 kN respectively ($\varepsilon_{us} = 0.0010$).

($P_t = 400$ and 800 kN respectively); the influence seems to diminish somewhat at higher load levels. Yet, the total deformation plot shown in Fig. 5.12, indicates that the concrete element next to the support platen has the largest deformation. In the experiment, this dominant crack was not observed. No good explanation can be given for these deviations between experiment and analysis. Possibly the thin mortar layer between the support platen and the panel has some influence on the stress distribution. In the analysis Poisson's ratio of the supporting steel platen was taken as equal to that of the concrete. This was done in order to avoid major disturbances in the stress field directly over the support, and to simulate the mortar layer. One should bear in mind that already in the linear-elastic analysis the largest tensile principal stress was calculated

next to the support platen, and was responsible for crack initiation at this particular place. In the experiment cracking started in the middle of the beam, as can be seen from Fig. 5.3.
The steel stress plots also clearly show the position of the dominant crack near the support platen, although the effect diminishes when the external load is increased (Fig. 5.13b). The effect of reducing $\varepsilon_{us}$ is shown in Fig. 5.13a, and the expected result is obtained. Unfortunately no more data are available in the mid-section of the reinforcing bar. In the second deep beam analysis, some more experimental results were available. From the stress plots, it can be seen that at the highest load level hardly any tensile stresses are transferred in the cracked zone. A second dominant crack near the centre of the panel is even visible. The results indicate that after the panel cracked in the central region, the load is transferred directly through the "concrete column" over the support, to this support.
Finally, the panel fails due to "yielding" of the concrete over the supports. This is clearly visible in the incremental deformation plots, but also in the plot of the total deformations at $P_t = 1100$ kN (Fig. 5.12d). In the load-deflection diagram a stiffer response of the panel was calculated at higher loading levels (e.g. $P_t > 600$ kN). The fact that the behaviour of the panel is completely determined by the behaviour of the "concrete column" over the support (see Fig. 5.10) may be responsible for these deviations. As can be seen from Fig. 5.6, the behaviour of concrete in compression is simulated by an elasto-plastic model, which does not give a good fit with the experimentally observed stress-strain curve. Only recently, a better model has been implemented (Vermeer and De Borst, 1984), but was not generally available at the time when these analyses were carried out.

### 5.1.6 Conclusions

The following conclusions can be drawn:
- A realistic simulation of the structural behaviour of the reinforced concrete panel on two supports is possible. The load-deflection curve observed in the experiments, but also crack patterns, are quite well simulated.
- The behaviour of the panel is, after the central region has cracked, completely determined by the compressive response of the "column" over the support. The results indicate, that as soon as this central region is separated from the "column", failure is inevitable. This separation seems to occur through the development of a dominant crack in the panel next to the support platen. This dominant crack was not observed in the experiment.
- When small problems such as this beam on two supports are analysed, a parameter study can easily be carried out, which is considered very favourable.

## 5.2 *Deep beam on three supports*

### 5.2.1 Introduction

Leonhardt and Walther also tested two deep beams on three supports. One of these

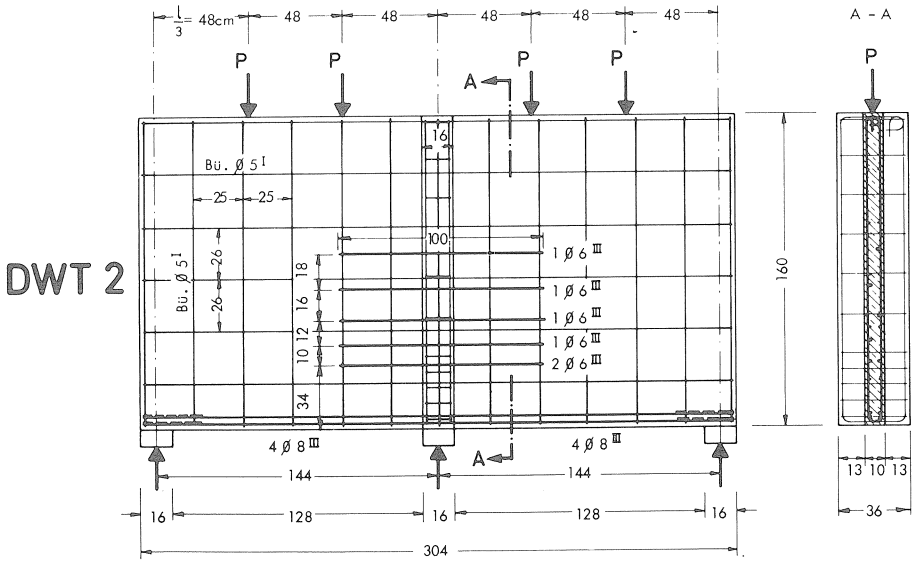


ⓐ dimensions in cm, ⌀ reinforcement in mm

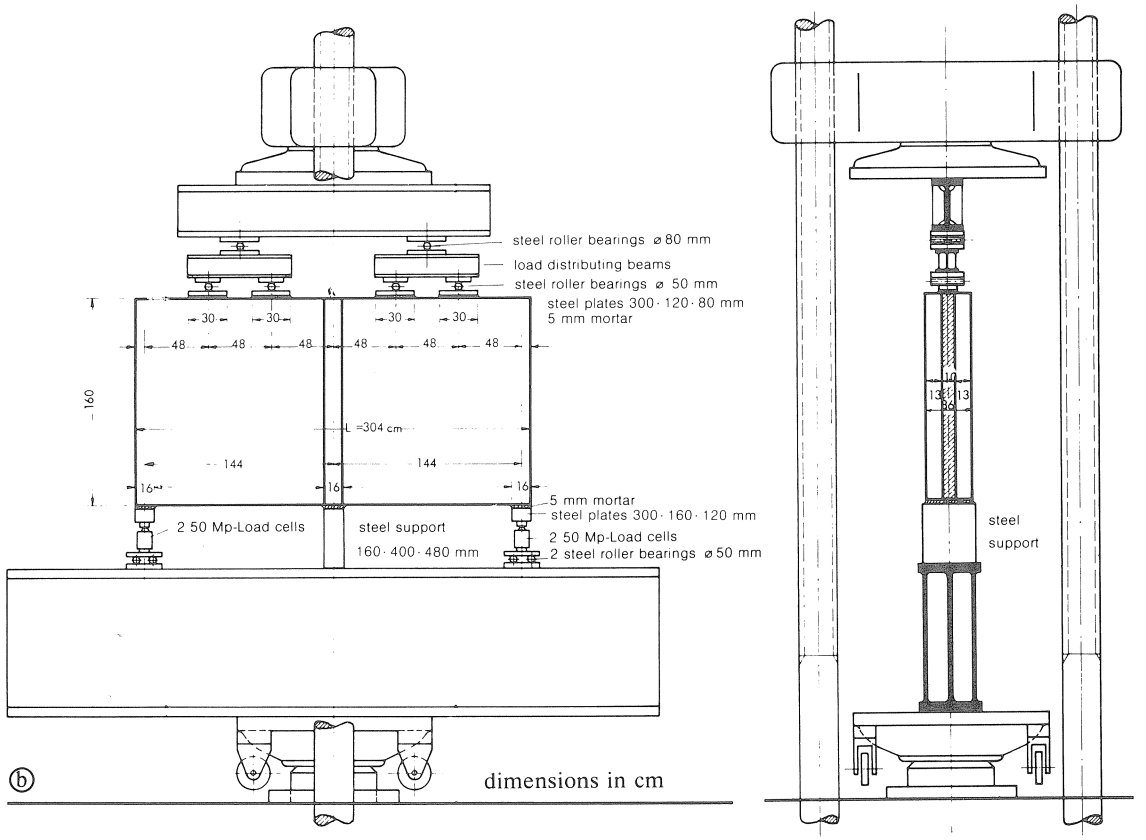


ⓑ dimensions in cm

Fig. 5.14. Reinforced concrete panel DWT2, dimensions and reinforcement details (a) and test set-up (b).

beams, DWT2, has been chosen for the numerical simulation with DIANA. Particularly this beam on three supports has been chosen because rather dominant shear cracks determine the behaviour of this beam. It was considered interesting to ascertain whether such behaviour could be simulated in a non-linear analysis.

### 5.2.2 Description of the experiment

The loading procedure and the specimen (DTW2) are shown in Fig. 5.14. Details of the test set-up and loading conditions are shown in Fig. 5.14b. The dimensions of the beam as well as details of the reinforcement are given in Fig. 5.14a. It is a beam on three supports with a 360 mm thick supporting member in the middle. The thickness of the panel is 100 mm, with overall dimensions of 3040 mm × 1600 mm. For the three supports two steel platens on roller bearings are used and, in the middle, a block made of steel. A thin layer of mortar was placed between the beam and steel loading platens as well as between the beam and the supporting steel platens. The load was applied in steps of 100 kN and 200 kN.
Four 8 mm diameter reinforcing bars were installed in the lower part of the beam, and a double square grid of 5 mm bars was placed over the entire panel (see Fig. 5.14a). Furthermore, six reinforcing bars of 6 mm diameter were installed over the middle support as indicated in Fig. 5.14b.
The load-deflection curve is shown in Fig. 5.15a. The deflection was measured in the middle of each of the two spans (the measurements were performed up to a load level of 2200 kN). Since hardly any difference between these two deflections was observed, only one of them is shown. The crack patterns recorded during the test are given in Fig. 5.16.

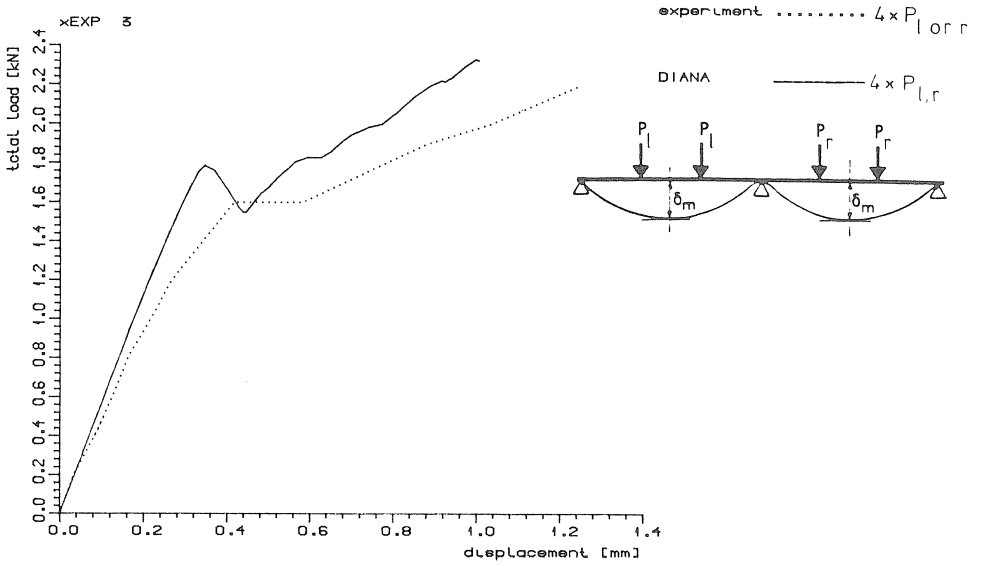


Fig. 5.15.a Load-deflection curve at midpsan.

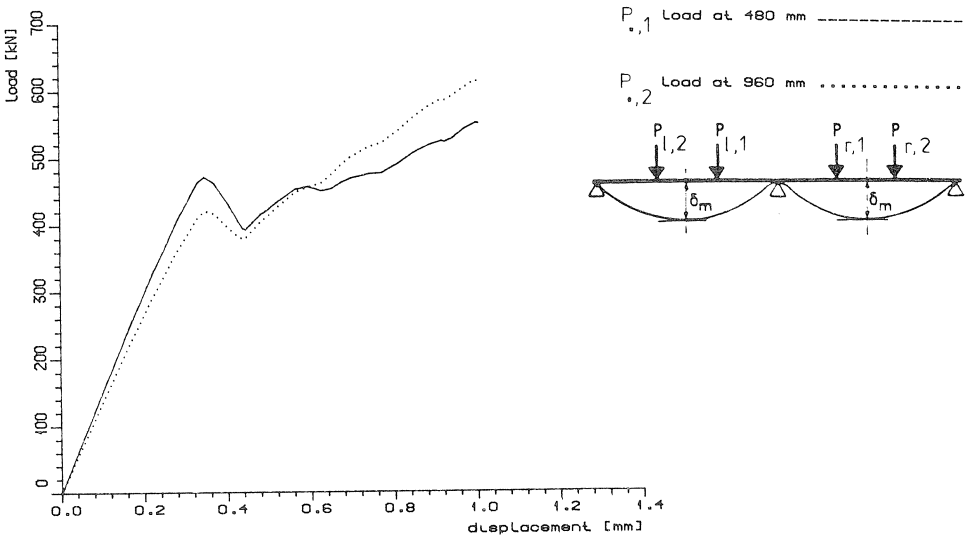


Fig. 5.15b. Difference between the applied loads in the analysis.

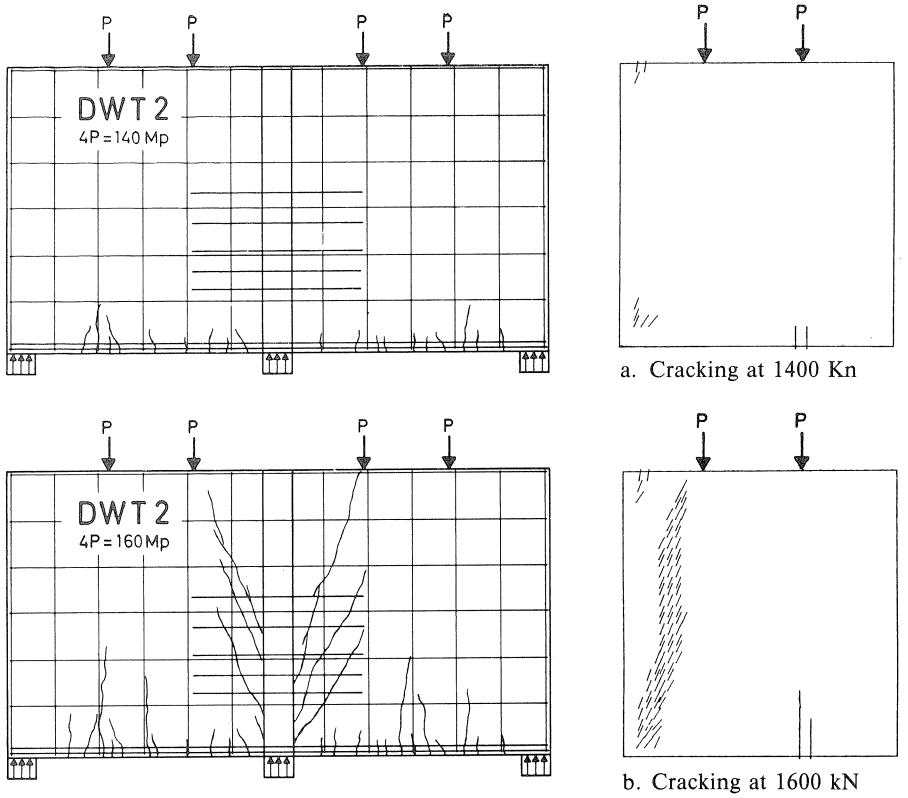


a. Cracking at 1400 Kn

b. Cracking at 1600 kN

Fig. 5.16. Cracking observed in the experiment and calculated cracks (strains $> \varepsilon_{us}$).

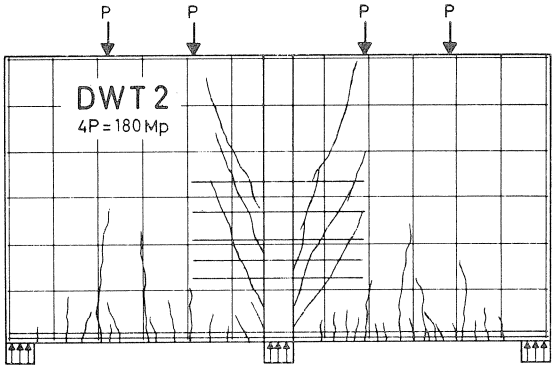


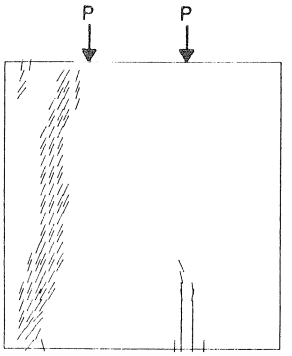


c. Cracking at 1800 kN

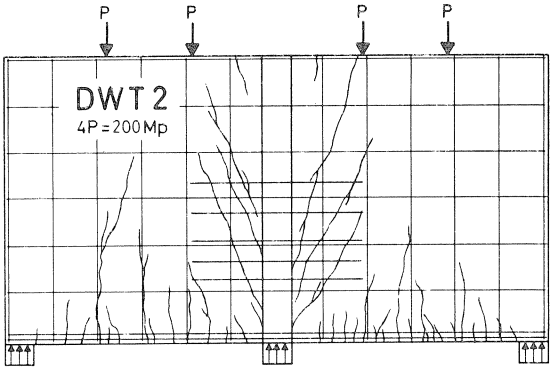


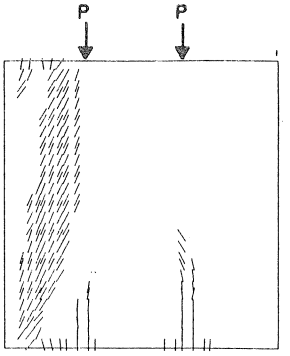


d. Cracking at 2000 kN

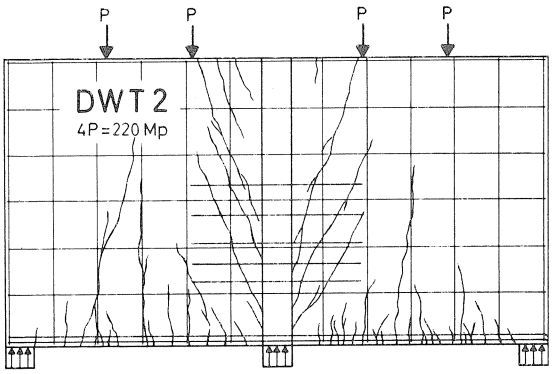


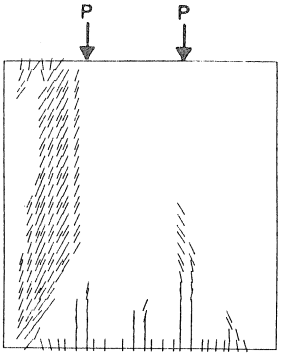


e. Cracking at 2200 kN

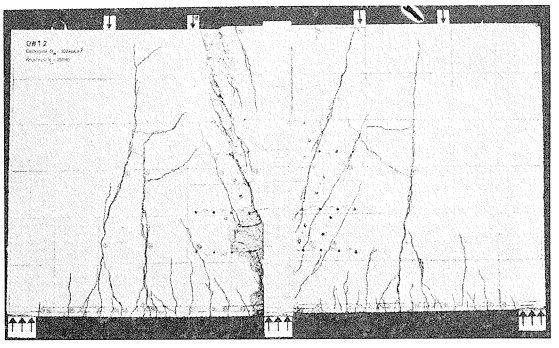

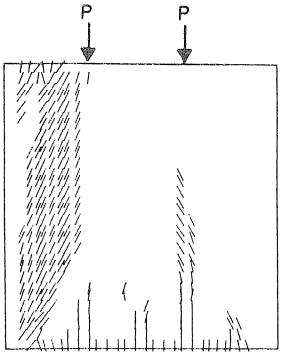


f. Failure

The first crack appears about 500 mm from the right support of the beam, at a load level of 1200 kN. The steep shear cracks beside the supporting beam appeared suddenly during the load step from 1400 to 1600 kN: the crack on the left of the supporting member at a load level of 1550 kN and the one on the right at 1600 kN. The development of these cracks caused the plateau in the load-deflection curve at 1600 kN.
Up to 2000 kN, load steps of 100 kN each were taken. Thereafter the load step size was increased to 200 kN, until failure of DWT2 occurred at 2510 kN. Fig. 5.16f shows the beam at failure. Two failure zones developed, one next to the loading platen, and the other beside the supporting member. The reinforcement acts like a dowel and deformed considerably. Yielding of the reinforcement (6 ⌀ 6) over the middle support was reported at this point. The stresses in the main reinforcement (4 ⌀ 8) remain just below the yield stress. In Fig. 5.19b the steel stresses in this reinforcement are shown at a load level of 2200 kN. These stresses were determined at 12 positions in both spans. Both spans are drawn in one diagram, starting from the middle support. In this case the span to the left of the middle support is mirrored.

### 5.2.3 Parameter for the analysis

#### 5.2.3.1 Element discretization

The adopted element mesh and reinforcement are shown in Fig. 5.17. Due to symmetry it is possible, as with the deep beam on two supports, to model only one half of the beam. Plane stress elements are used, with 8 nodes each. Full bond is assumed between the reinforcement and the concrete. Support platens are modelled in the same way as described in 5.1.3.1. Three triangular plane stress elements were used for refining the mesh near the right (left) support platen. This was done to avoid having to define the whole support reaction at a middle node.

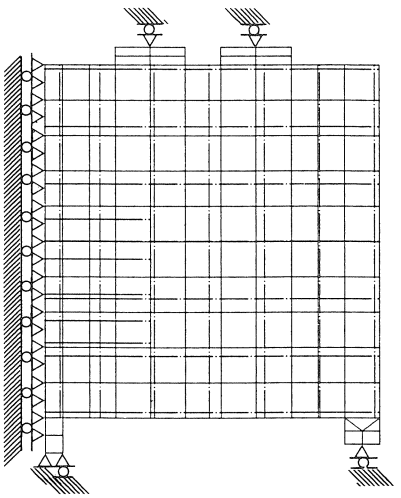

Fig. 5.17. Element mesh, dash-dotted lines indicate the location of the reinforcing bars.

In the experiment the loading was applied through loading platens. These platens were included in the finite element model.

### 5.2.3.2 Material parameters

The complete set of material parameters used in the analysis is listed below. The parameters used for the support- and loading platens are included. For an explanation, see Chapter 0.

*Concrete*
$E_c = 32000$ N/mm$^2$
$\nu = 0.2$
$f_{ct} = 3.02$ N/mm$^2$
$f_{cc} = 30.2$ N/mm$^2$
tension cut-off 1
$\varepsilon_{us} = 0.001$
$\beta = 0.2$
The value for the tensioning stiffening parameter $\varepsilon_{us}$ was taken as similar to the value used in the preceding analysis (viz. the panel on two supports). This seems possible because the element mesh and reinforcement are comparable.

*Reinforcing steel*
$E_s = 210000$ N/mm$^2$
$f_{sy} = 430$ N/mm$^2$

*Support and loading platens*
$E_s = 210000$ N/mm$^2$
$\nu = 0.2$

### 5.2.3.3 Load case

In a preliminary attempt a load-controlled process was chosen for analyzing the beam. For reasons explained in Chapter 5.2.5 the load-controlled process caused numerical problems. The simplest way of solving this was to adopt a displacement-controlled process. This means that the two concentrated loads do not necessarily remain equal during the loading process. However, in the present analysis the differences were not very large, as will be shown later on.

## 5.2.4 Results

In Fig. 5.15a the computed load-deflection diagram is compared with the experimentally observed behaviour. The stiffness in the linear-elastic stage is described rather well, but the non-linear behaviour seems somewhat too stiff. The diagram shows an interest-

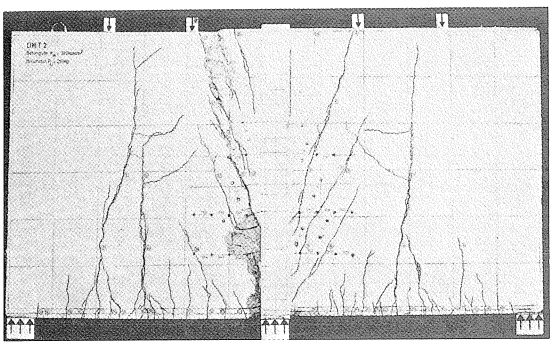

Fig. 5.18a.
Cracking observed in the experiment at failure.

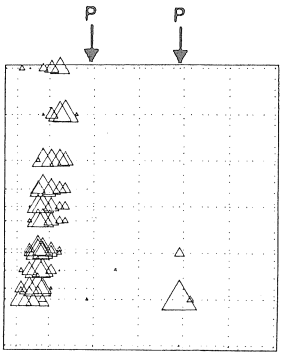


Fig. 5.18b.
Calculated reinforcement plasticity at failure.

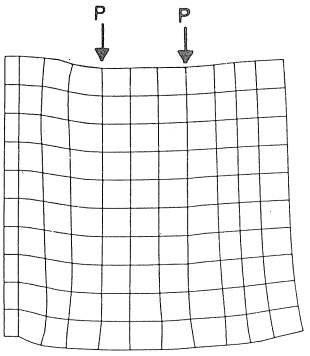


Fig. 5.18c.
Calculated total displacements at failure.

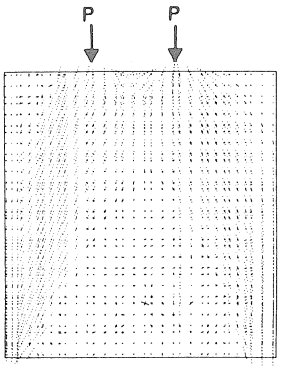


Fig. 5.18d.
Calculated principal stresses at failure.

ing dip between 1550 and 1800 kN, when the dominant shear crack arises beside the supporting member. The load level at which the shear crack develops is predicted rather well. The failure load is underestimated in the analysis, 2333 kN, or 93% of the failure load observed in the experiment (2510 kN).

The computed crack development can be compared with the reported crack patterns at five different load levels (respectively at 1400, 1600, 1800, 2000 and 2200 kN) and with the reported crack pattern at failure (see Fig. 5.16). Only the "open" cracks are shown, with crack strains greater then $\varepsilon_{us} = 0.001$. Note that only one half of the panel is shown without loading or support platens. The cracks can be compared with the reported ones to the right *and* left of the middle support. The steep shear crack next to the supporting member is simulated quite well in the numerical analysis. Also, the development of the cracks in the spans between the supports is closely similar to the experimental results.

The behaviour at failure is shown in Figs. 5.18 and 5.19. As in the experiment, the reinforcement in the shear cracks yields and failure occurs when all the bars over the middle

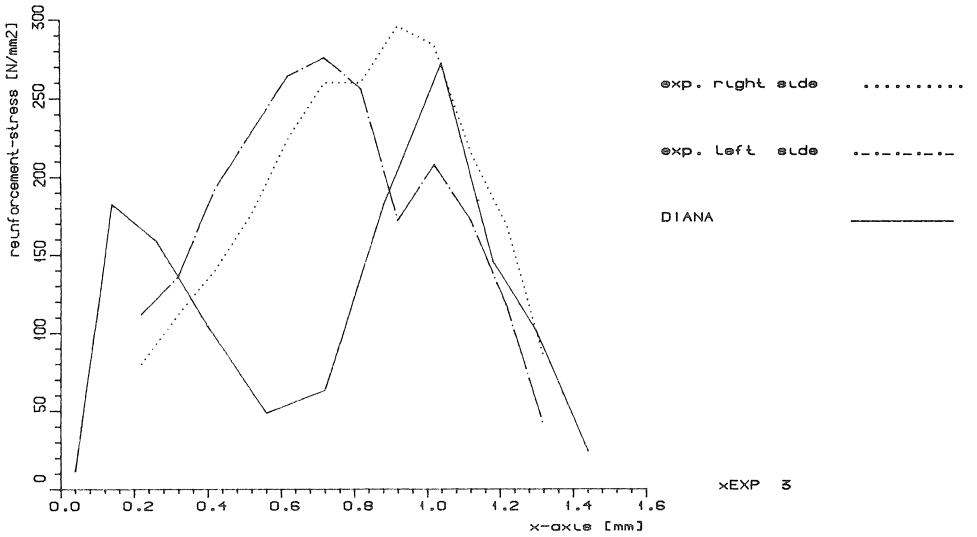


Fig. 5.19a. Stress distribution in the lower reinforcing bar at a load level of 1800 kN.

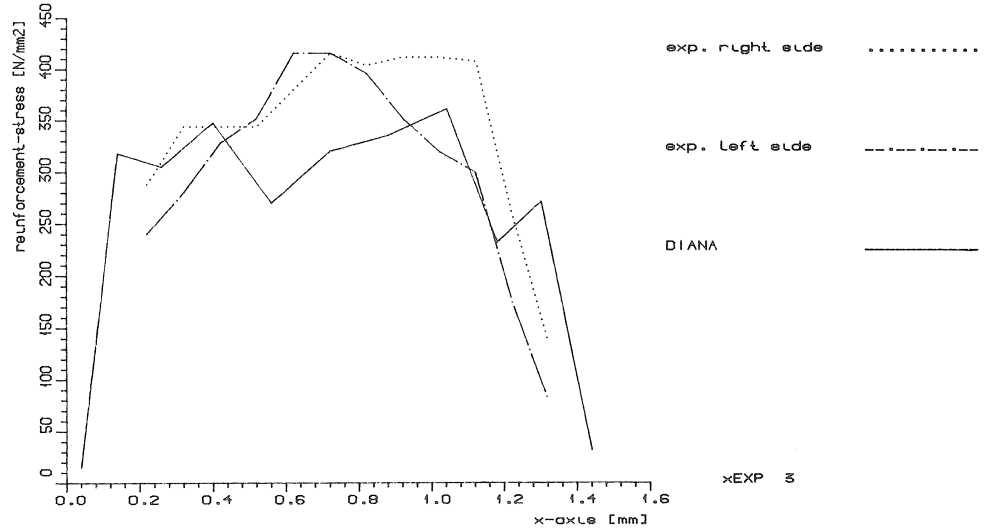


Fig. 5.19b. Stress distribution in the lower reinforcing bar at a load level of 2200 kN.

support start to yield (see Fig. 5.18b). The calculated stresses are shown in Fig. 5.18d, and exhibit almost the same distribution on the right-hand side of the panel when compared with the results obtained from the analysis of the beam on two supports (Fig. 5.10d). In Fig. 5.18c the calculated total deformations are shown. Compare the upper edge with the part to the left of the middle of the panel in Fig. 5.18a.
In Fig. 5.19 the calculated stresses in the lower reinforcing bar are shown at a load level of 1800 and 2200 kN. The stresses in the lower reinforcement bar in the span remain just above the yield stress level. This was also observed in the experiment.

### 5.2.5 Discussion

The development of a dominant crack just beside the left or right support as reported in the analysis of the deep beam on two supports, does not occur in this example. Though the first cracks are computed at the same position, they do not become dominant.
The steep shear crack next to the supporting member in the middle of the panel is predicted rather well. From the load-deflection curve in Fig. 5.15a it can be seen that the loading force undergoes a considerable drop. Since the experiment was load-controlled, the curve of the experiment cannot be computed this way. Numerically, this kind of calculation causes problems when a load-controlled proces is used, although DIANA procedures are available to "get through the dip" with a load-controlled proces (the Riks method). The difficulty can also be solved by using a displacement-controlled process, as was done here. Only then does a difference between the two (or, rather, the twice two) applied loads occur as shown in Fig. 5.15b. Only minor influences on the results are expected, since the loads differ only slightly.
The calculated crack development in the span of the beam shows a very good resemblance to the reported crack patterns in the left span, also the span where failure occurred. Direction and length of the cracks are predicted satisfactorily.
The stiffer response of the panel is probably due to the same cause as that mentioned for the deep beam on two supports in Chapter 5.1.5: the behaviour of the "concrete" column over the support (see Fig. 5.18d). At failure another reason may be that in the shear cracks beside the supporting member the reinforcement acts like a dowel (see Fig. 5.18a). In the experiment these bars will slip. In the analysis bond-slip of the reinforcement has not been taken into account.
The results of the stresses measured in the reinforcing bar are also interesting. At a load level of 1800 kN (Fig. 5.19a) the influence of open cracks is clearly seen. In two places where the cracks develop (compare the crack pattern at this level, Fig. 5.16c), a large increase in stress occurs. The experimental results give higher stresses in the middle of the spans, since more cracks have developed there. No higher stress for the steep shear crack next to the middle support are reported, since no measurements were taken in that region.
At a higher load level of 2200 kN far better agreement between the calculated and experimental stresses in the reinforcement is observed (Fig. 5.19b). More cracks have now opened (Fig. 5.16e) and the calculated stresses in the reinforcement in the span are also higher and compare more favourably with the experimental stresses. Unfortunately, the stress in the crack beside the supporting member cannot be compared with the experimental results.
In this example, failure by "yielding" of the concrete above the supports (see 5.1.5, the analysis of the beam on two supports) does not occur. Failure occurs (before compressive failure of the concrete can occur) by yielding of the reinforcement in the shear crack. The deformations of the panel are "predicted" quite satisfactorily in the analysis (compare Figs. 5.18a and 5.18c); note especially the resemblance near the edges.

### 5.2.6 Conclusions

The following conclusions can be drawn:
- A realistic simulation of the structural behaviour of the reinforced concrete panel on three supports is possible. Crack patterns and the sudden appearance of a steep shear crack are quite well simulated.
- The steep shear crack determines the behaviour of the panel: as soon as this crack has developed and reinforcement in the crack yields, failure is inevitable.
- The compressive response of the "column" over the supports is not important for failure, but seems to influence the stiffness.
- The previous analysis of the beam on two supports proved to be fruitful, especially for determining the tension stiffening parameter $\varepsilon_{us}$.

## 6 LNG tank

### 6.1 *Introduction*

In recent years much attention has been given to cryogenic storage of hydrocarbons. Hydrocarbons can be stored under atmospheric pressure in liquefied condition when cooled to a temperature below the evaporation point. The volume of the gas decreases to 1/600 of the original volume for LNG (Liquefied Natural Gas) and to 1/270 for LPG (Liquefied Petroleum Gas). Therefore, the storage temperature has to be $\approx -160\,°C$ for LNG and $\approx -50\,°C$ for LPG.

The most commonly used type of tank is a double-walled tank, consisting of an outer tank of mild steel surrounding an insulated tank of 9% nickel-steel. In order to obtain the necessary security against external hazards (for instance fire, impact loads or explosions) concrete can be used, and an obvious choice is to replace the outer tank by a concrete one. This has resulted in the development of a so-called C-IS (concrete-insulation-steel) tank. The storage tank is single-walled and is provided with an insulation layer on the outside in order to maintain the desired low temperature. The outer wall is separated from the insulation by a cavity. In this analysis the outer tank will be subjected to two different load cases, which will be analysed separately:

1. The tank will be filled with water to a certain height in order to investigate the liquid-tightness.
2. The tank will be subjected to a fire load caused by an adjacent tank which is on fire.

Before a new storage tank structure is commissioned, test loadings have to be performed. In principle, there are three possibilities: the "water test", the "gas test" and the "cooling test".

The so-called "water test" means that the tank has to be filled with water until the load on the base of the tank is equal to 1.25 times the maximum working load. Assuming a density of LNG of about 500 kg/m$^3$ and a maximum height of 30.0 m results in a water level of 18.7 m.

## 6.2 *Description of the problem*

The storage tank which will be investigated was designed and analysed by Muller (1985). This tank has been chosen because a substantial amount of information on this tank is available. Its cross-section is shown in Fig. 6.1. The roof and the base are monolithically connected to the wall. The storage tank is supported on 497 precast concrete piles, each with a cross-section of 0.45 m*0.45 m. These piles are placed in concentric circles and are equally spaced at 2.0 m within each circle. The circles are spaced at a distance of 2.083 m.

The amount of prestressing steel has been calculated on the following assumptions (Muller, 1985):

- The outer vessel will be filled with water to a height of 18.7 m (the so-called water test) or will be filled with LNG to a height of 30.0 m.
- The amount of horizontal prestress in the outer wall is calculated using the so-called tangential force balancing method. This means that the tangential force which is introduced by the horizontal prestress balances the tangential force caused by the water test or the LNG-load.

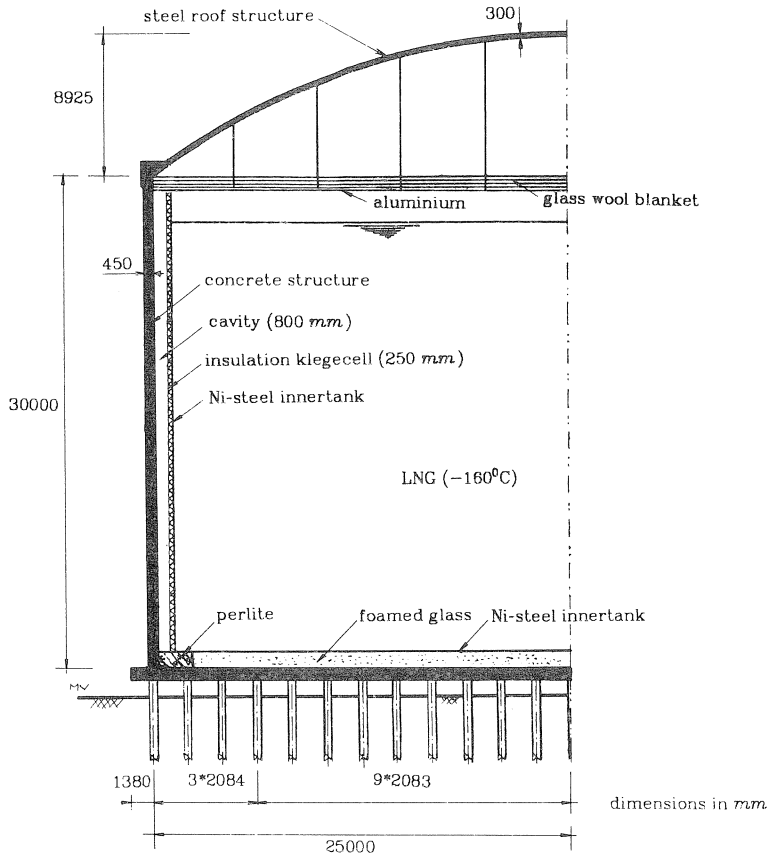


Fig. 6.1. Cross-section of the LNG tank.

- When the tank is loaded with water or LNG, the average tangential stress in the concrete must at least be equal to $-0.7$ N/mm$^2$.

The horizontal prestress in the wall is induced by 84 Freyssinet 12/12.5 prestressing cables. These cables are variously spaced. The smallest distance is 0.2 m at a height of 5.4 m above the base. The vertical prestress in the wall is induced by Freyssinet 12/15.2 cables, which are equally spaced at a distance of 2.0 m. They induce a mean compressive stress of $-2.0$ N/mm$^2$. As the horizontal prestress in the wall is based on the so-called tangential force balancing method, the shear force acting at the wall-to-base connection will introduce tensile stresses in the base if the vessel is loaded beyond a certain level. Therefore the base is prestressed using 10 cables Freyssinet 24/12.9, which introduce a compressive stress of $-1.5$ N/mm$^2$. The base is extended outside the wall in order to provide room for these cables.

The yield stress of the prestressing steel is 1860 and 1760 N/mm$^2$ for the 12/12.5 and 24/12.9 cables and for the 12/15.3 cables respectively.

The quantity of reinforcing steel is:

- At the bottom and top of the base ⌀ 20–250, both in the radial and the tangential direction.
- At the inside and outside of the wall ⌀ 25–250 in the vertical and the tangential direction. Only over the bottom 3.6 m at the inside of the wall, the quantity of reinforcing steel is equal to ⌀ 32–250 in the vertical direction and ⌀ 20–250 in the horizontal direction.

### 6.3 *Parameters for analysis*

In the numerical analysis, the tank has been schematized using axi-symmetric elements. Not only the water test, but also the fire load can be schematized in this way. This is due to the fact that the circumferential temperature gradient is not very steep. Elastic finite element analysis was performed in order to investigate this assumption. Stresses and strains in the hottest section were calculated. It appeared that there is no significant difference between the calculation with an axi-symmetric temperature pattern and the calculation with a temperature pattern that varies along the circumference of the tank (Walther, 1983).

It should also be mentioned that a three-dimensional analysis would require very many elements and a vast amount of computer-time.

#### 6.3.1 Element discretization

The element mesh is shown in Fig. 6.2. The mesh has been refined near the wall-to-base connection. The wall as well as the base have two elements through depth. The foundation piles are modelled as axial springs. The lateral resistance due to the flexural stiffness of the pile has been neglected. The axial stiffness has been schematized by using a linear elastic force-displacement diagram.

The concrete roof is omitted, since major attention will be paid to the wall-to-base

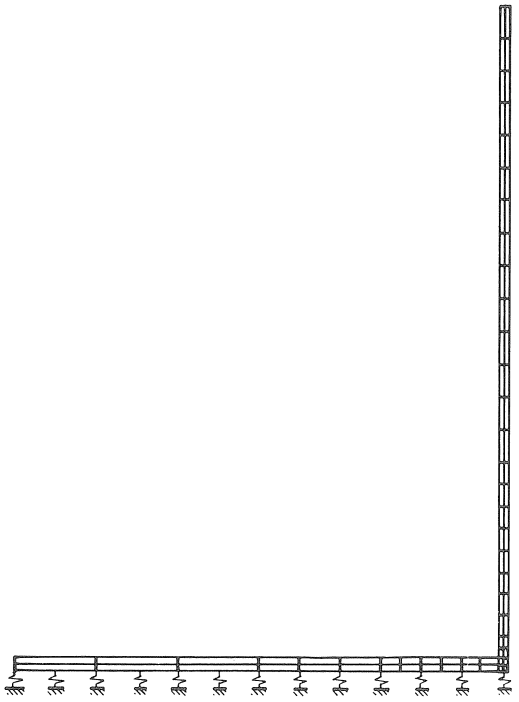

Fig. 6.2. Axisymmetric finite element idealisation.

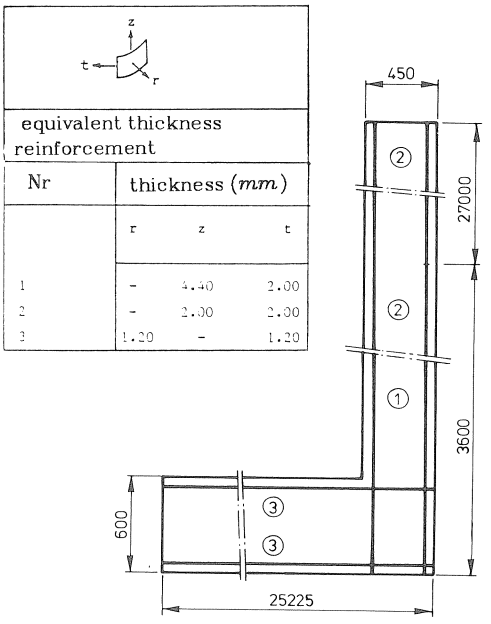


Fig. 6.3. Applied reinforcing steel.

connection. The stresses in this region are not much influenced by whether the roof has been taken into account or not. A uniform axial load is acting on the wall as a substitute for the roof loading.

The axi-symmetric model consists of 76 rectangular eight-noded isoparametric numerically integrated elements using a 3*3 Gaussian integration scheme. A total of 13 axial springs were used for schematizing the foundation piles. The reinforcing steel is schematized as indicated in Fig. 6.3.

### 6.3.2 Material parameters

The material parameters used in the analysis are summarized below.

*Concrete*
$E_c = 17500$ N/mm$^2$
$\nu = 0.2$
$f_{ct} = 1.8$ N/mm$^2$
$f_{cc} = 30.0$ N/mm$^2$
tension cut-off 2
$\varepsilon_{us} = 0.0019$
$\beta = 0.2$

*Reinforcing steel*
$E_s = 210000$ N/mm$^2$
$f_{sy} = 400$ N/mm$^2$
$\nu = 0.3$

*Prestressing steel*
$E_p = 210000$ N/mm$^2$
$f_{py} = 1760$ N/mm$^2$ (FeP 1760)
$f_{py} = 1860$ N/mm$^2$ (FeP 1860)
$\nu = 0.3$

a. Modulus of elasticity of concrete

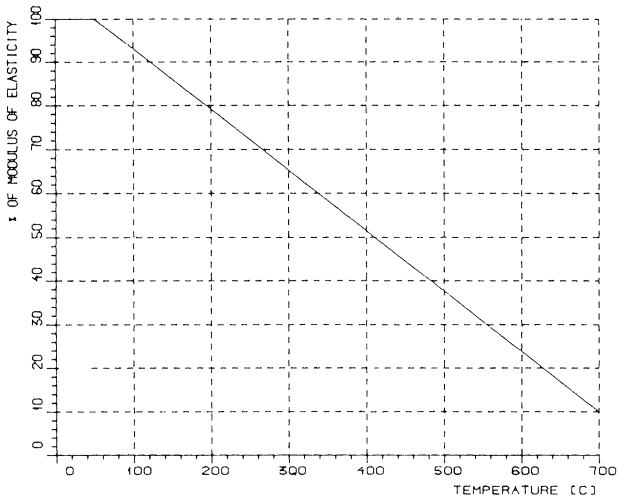


b. Modulus of elasticity of steel

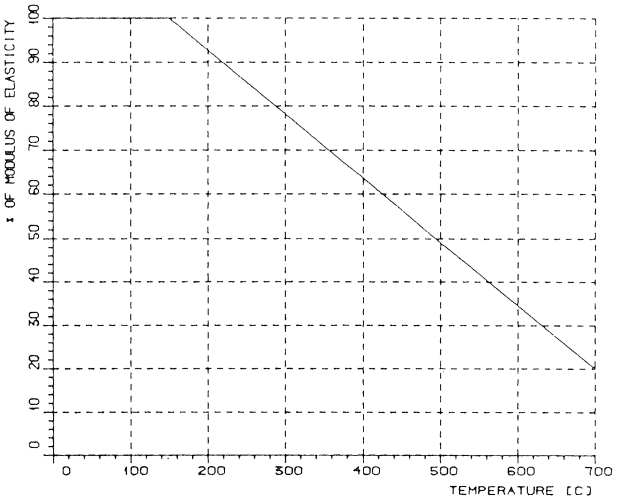


c. Thermal coefficient of expansion of concrete

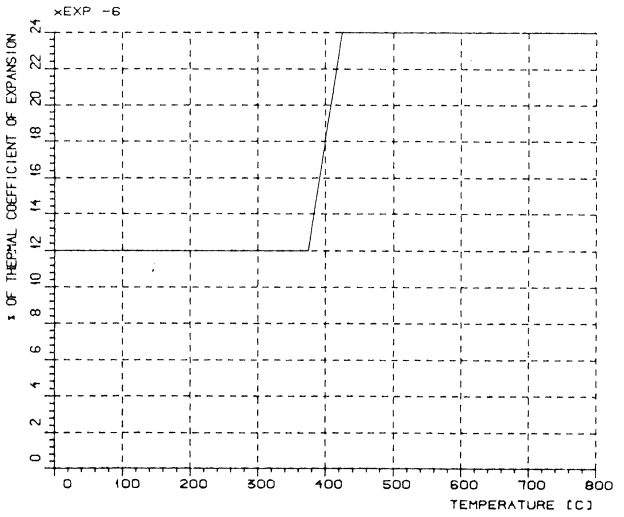


Fig. 6.4.
Material properties as a function of temperature.

In the fire load analysis some material properties are temperature-dependent, viz.:
- the thermal coefficient of expansion $\alpha_T$, and
- the modulus of elasticity of concrete and of the reinforcing and the prestressing steel.

The temperature dependence of these material properties is indicated in Fig. 6.4 (CEB, 1982).

The thermal coefficient of expansion of both the reinforcing and prestressing steel is assumed to be constant ($12.0*10^{-6}$/°C).

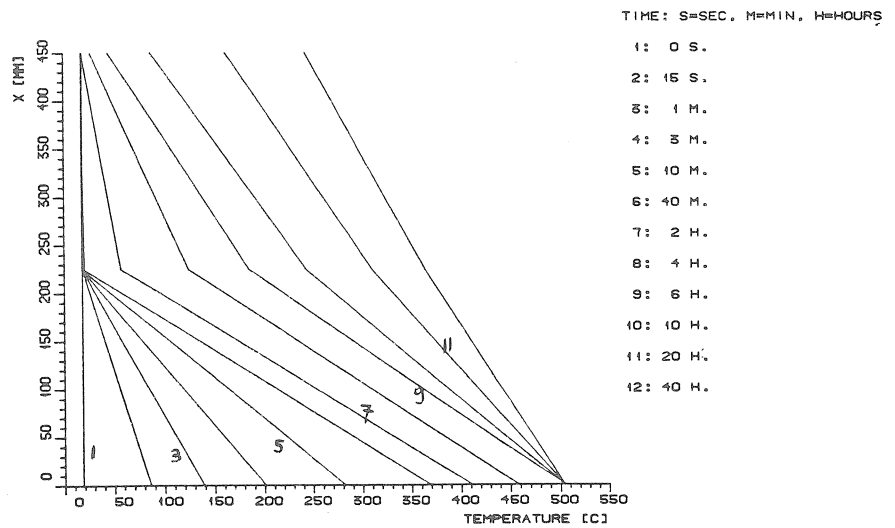


Fig. 6.5a. Development of the temperature in the wall of the tank as a function of time.

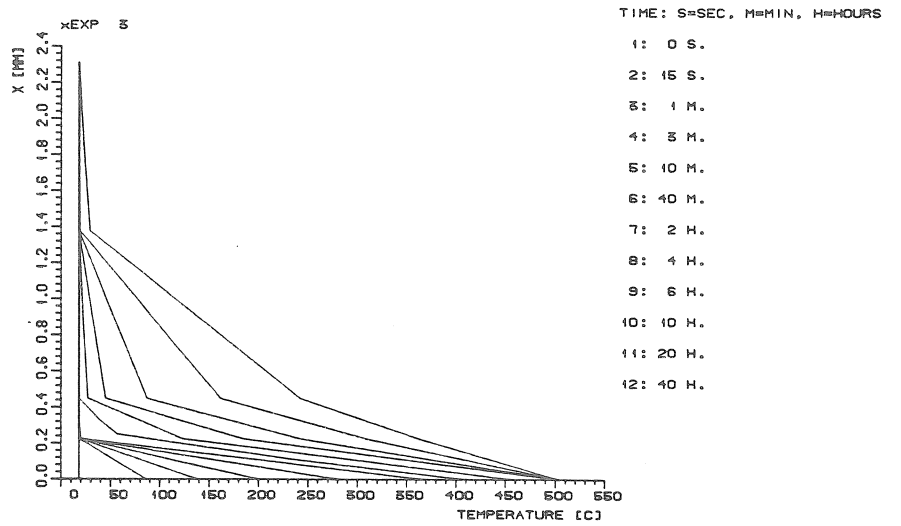


Fig. 6.5b. Development of the temperature in the base of the tank as a function of time.

### 6.3.3 Analyses performed

In this example, two analyses were carried out:

1. Tank subjected to water test.
   In this analysis the behaviour of the tank subjected to static loading was checked.
2. Tank subjected to fire load.
   In this second analysis the development of temperature with time is important. This is shown for both the wall and the base in Fig. 6.5 (Muller, 1984). The "manual calculation" was performed on the following assumptions: The fire load is caused by a burning adjacent storage tank which is at a distance of 62.5 m from the tank analyzed. The fire causes a thermal radiation of 30 kW/m$^2$, which is assumed to be constant over the height of the tank. This radiation is also assumed to be constant with time (40 hours).

Since the strength and the modulus of elasticity of the prestressing steel depend on the temperature, the prestress will decrease with time. This decrease has been determined by "manual" calculation (Muller 1984), and the result is shown in Fig. 6.6.

## 6.4 *Results*

### 6.4.1 Water test

In this paragraph the results will be presented when the tank is subjected to a water test. In order to investigate the behaviour of the tank, it was not only filled with water to a level equal to the water test level, but was filled as high as possible. In the analysis the tank was completely filled with water, and the water test level (18.7 m) was considerably exceeded (30.0 m).

The results from the analysis will be presented at the following loading situations:

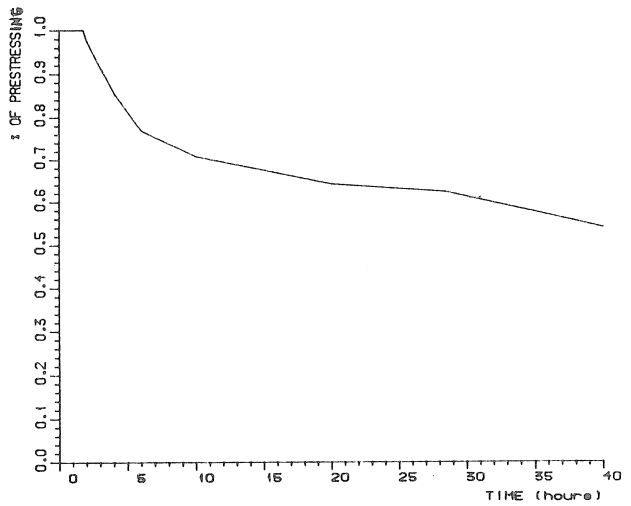


Fig. 6.6. Decrease of the prestress with time.

- The situation after prestressing.
- Water load up to 18.7 m (water test).
- Water load up to 24.6 m: the level at which the first crack occurs on the inside of the tank.
- Maximum load: the tank is completely filled with water.

Fig. 6.7 shows the development of the deformation of the tank (deformations are enlarged 250 times). After prestressing, an "inside bulge" develops in the wall of the tank. This is caused by the horizontal prestress in the wall. It can also be seen that the dead weight of the wall and the roof introduce relatively large deformations on the outside of the base. When the water load increases, the vertical deformation of the base increases gradually. The horizontal deformation of the wall decreases, due to the hydrostatic liquid pressure.

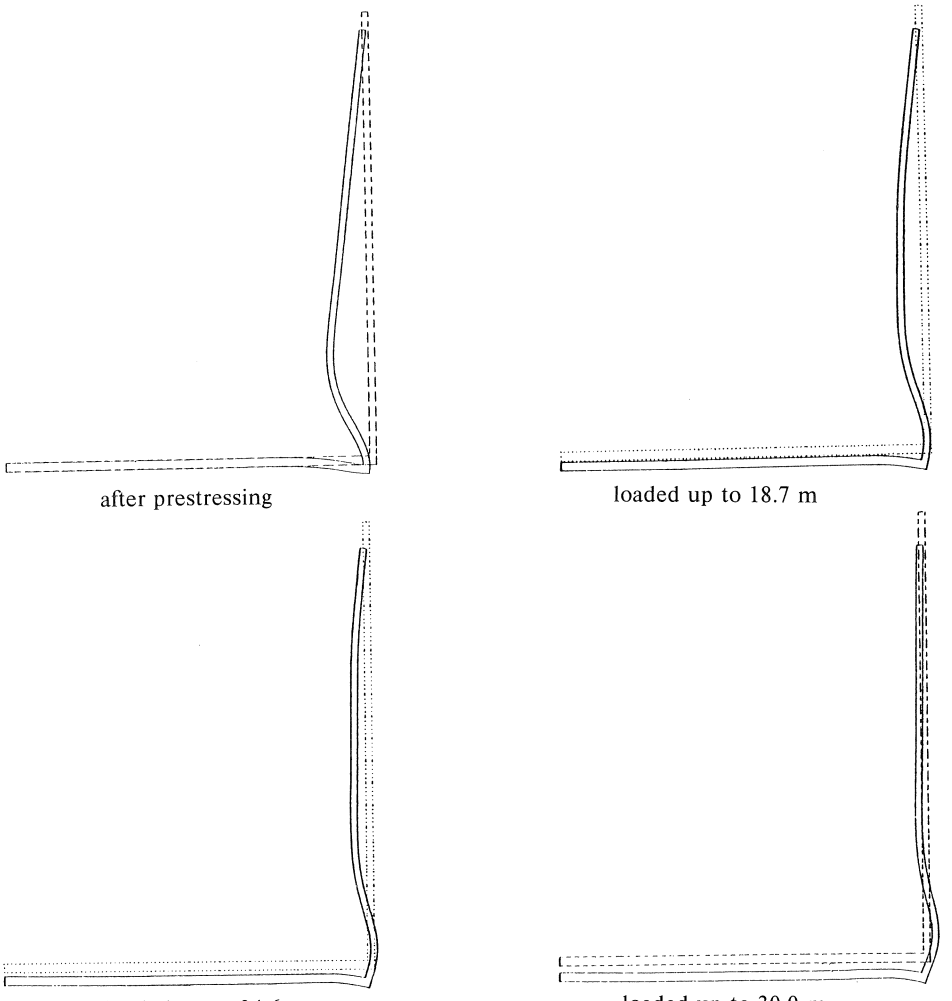


Fig. 6.7. Deformation of the tank (250 times enlarged).

Fig. 6.8 shows the development of the crack pattern. Four integration points located on the outside of the tank are cracked when the prestress is applied. When the tank is loaded with water, these cracks gradually close. At a water level of 15.6 m, all the cracks are closed, and the first crack on the inside of the tank develops when the water level is raised to 24.6 m. When the level increases, the number of cracks gradually increases and when the tank is completely filled, seven integration points are cracked.
In Fig. 6.9 the tangential force in the wall of the tank is shown at different loading levels. From this diagram it can be seen that the minimum tangential force is equal to $-340$ kN/m[1] when the tank is subjected to the water test. This is equal to a mean compressive stress of $-0.70$ N/mm$^2$. In this case, the compressive stress varies between $-1.23$ N/mm$^2$ on the inside of the tank and $-0.19$ N/mm$^2$ on the outside.

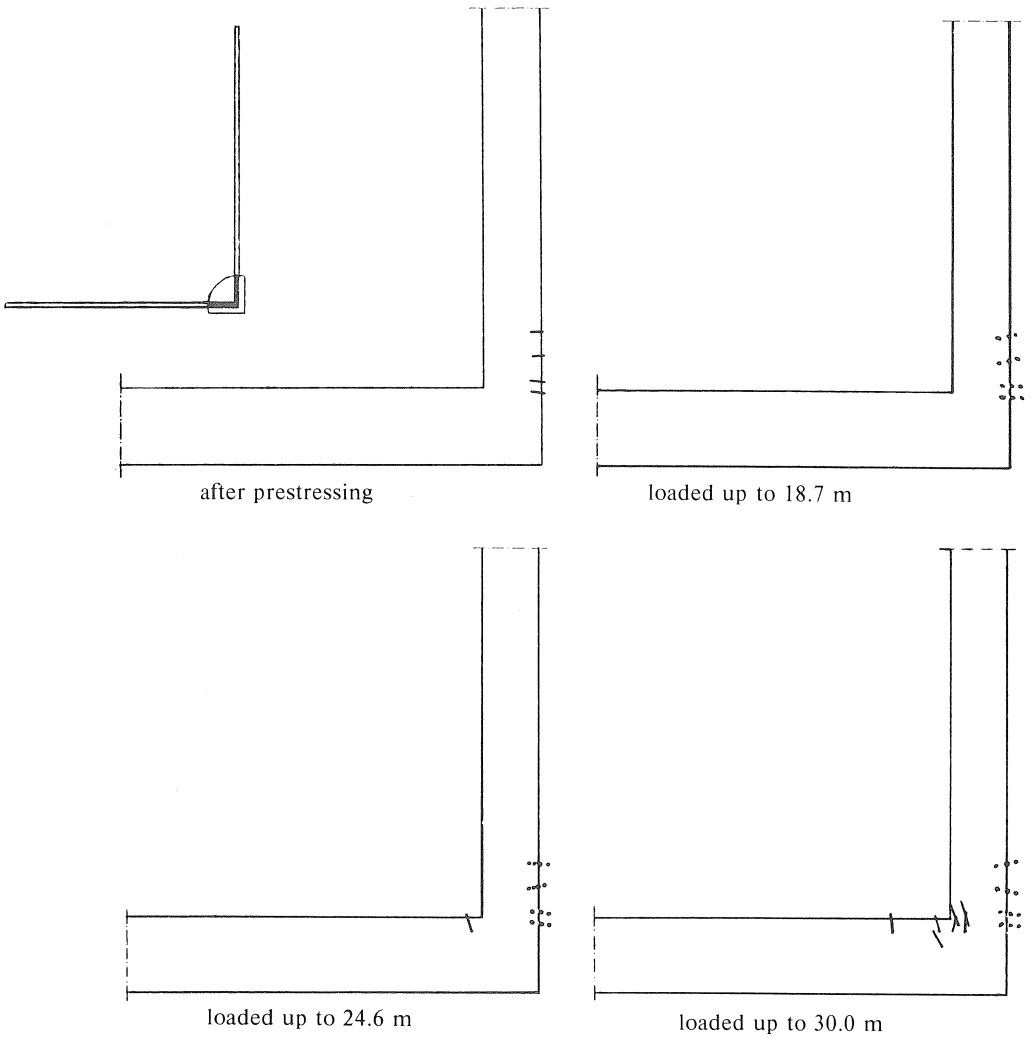


Fig. 6.8. Crack pattern of the tank (dotted lines indicate closed cracks).

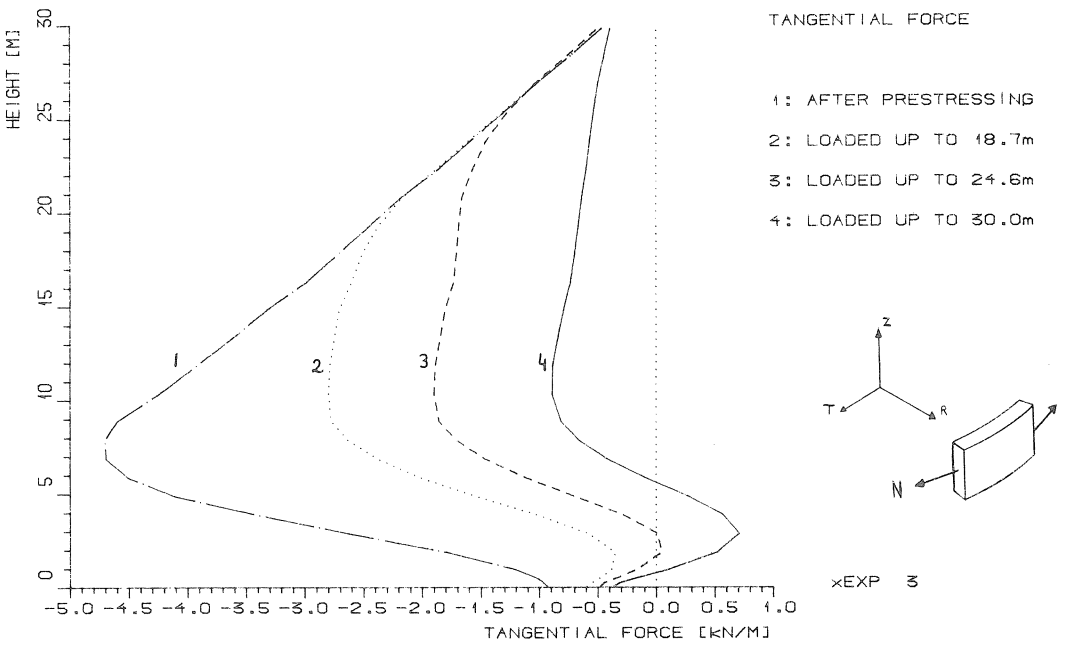


Fig. 6.9. Tangential force in the wall.

If the loading increases, the first tangential tensile stresses occur at a water level of about 24.6 m. This is equal to the level at which the first cracks at the inside of the tank are formed.
When the tank is completely filled, the tangential tensile force reaches a maximum of 710 kN/m$^1$, about 2.9 m above the base. This is equal to a mean tangential tensile stress of 1.45 N/mm$^2$.
The bending moment and the shear force in the wall are given in Figs. 6.10 and 6.11. The results of the static analysis (water test) are as expected and give confidence in the numerical simulation technique. We can now proceed with more complicated load cases.

### 6.4.2 Fire load

The development of the temperature in the tank is, as already stated, shown in Fig. 6.5. The temperature dependence of the material parameters were shown in Fig. 6.4. It should be mentioned again that in this analysis no plasticity, neither in the concrete nor in the reinforcing and prestressing steel, is taken into account.
The results of this analysis will be shown at the points of time at which the temperature is calculated (see Fig. 6.5).
The deformation of the tank is shown in Fig. 6.12, while Figs. 6.13 and 6.14 show the cracks which occur in the entire tank and in the wall-to-base connection. It should be mentioned that only cracks with a crack strain greater then $\varepsilon_{us}$ are shown.

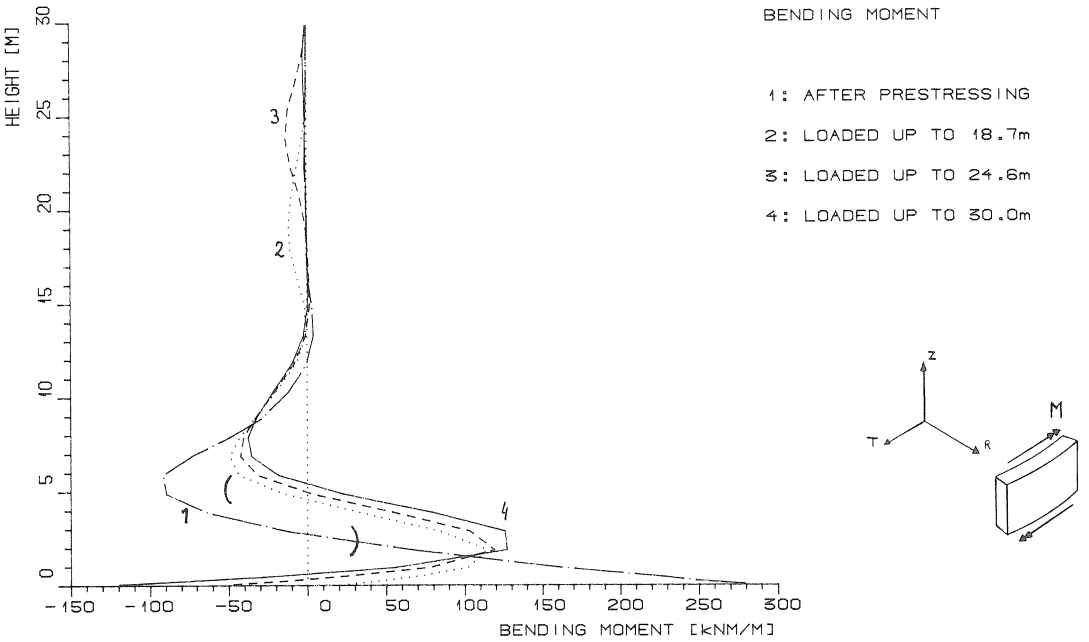


Fig. 6.10. Bending moment in the wall.

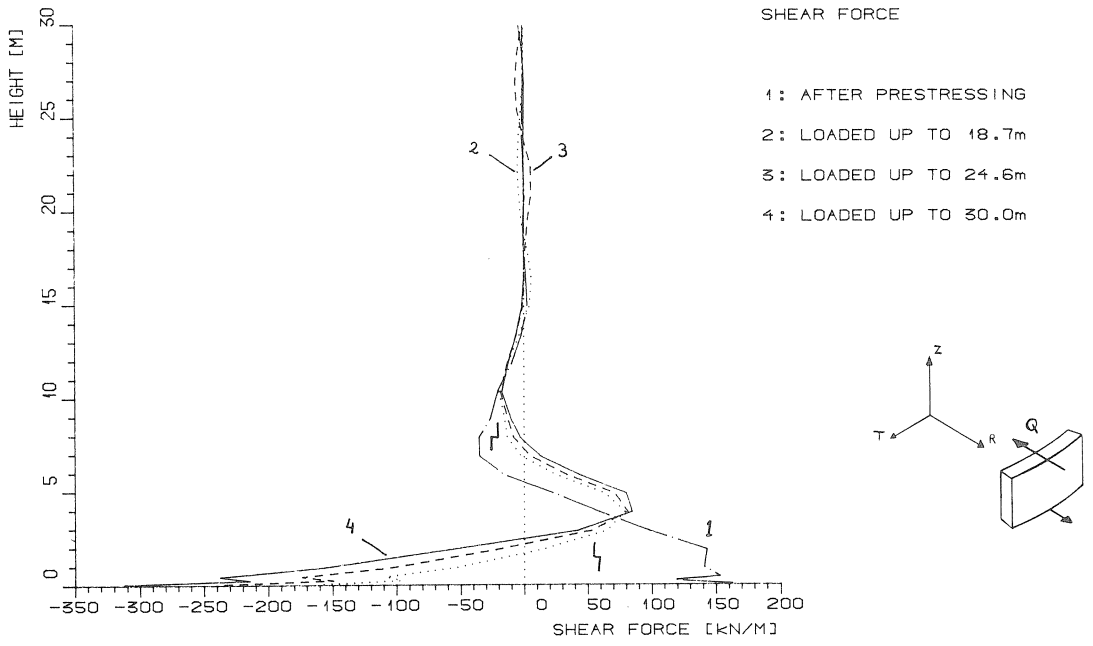


Fig. 6.11. Shear force in the wall.

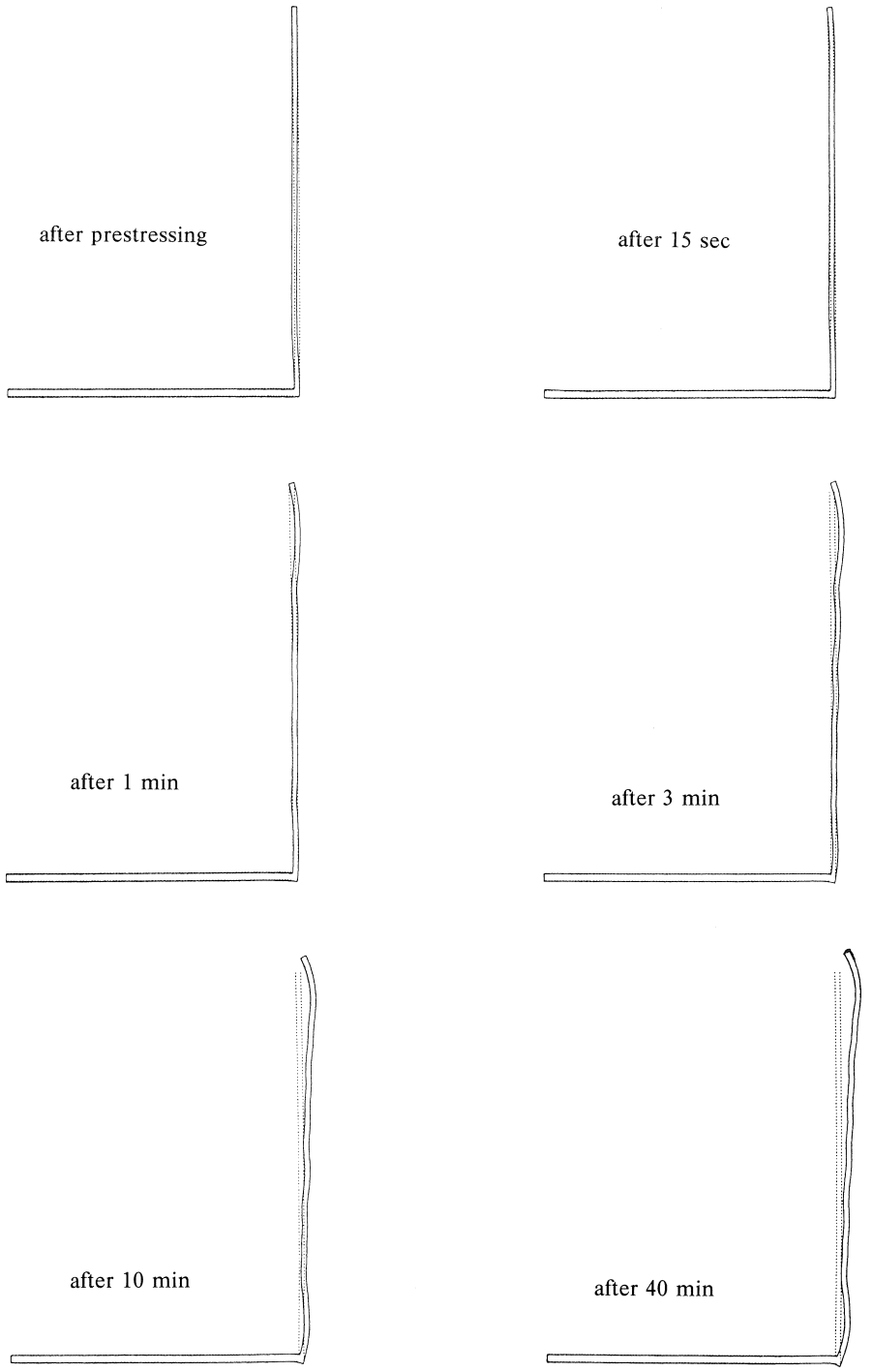


Fig. 6.12a. Deformation of the tank, $t = 0$–40 min (25 times enlarged).

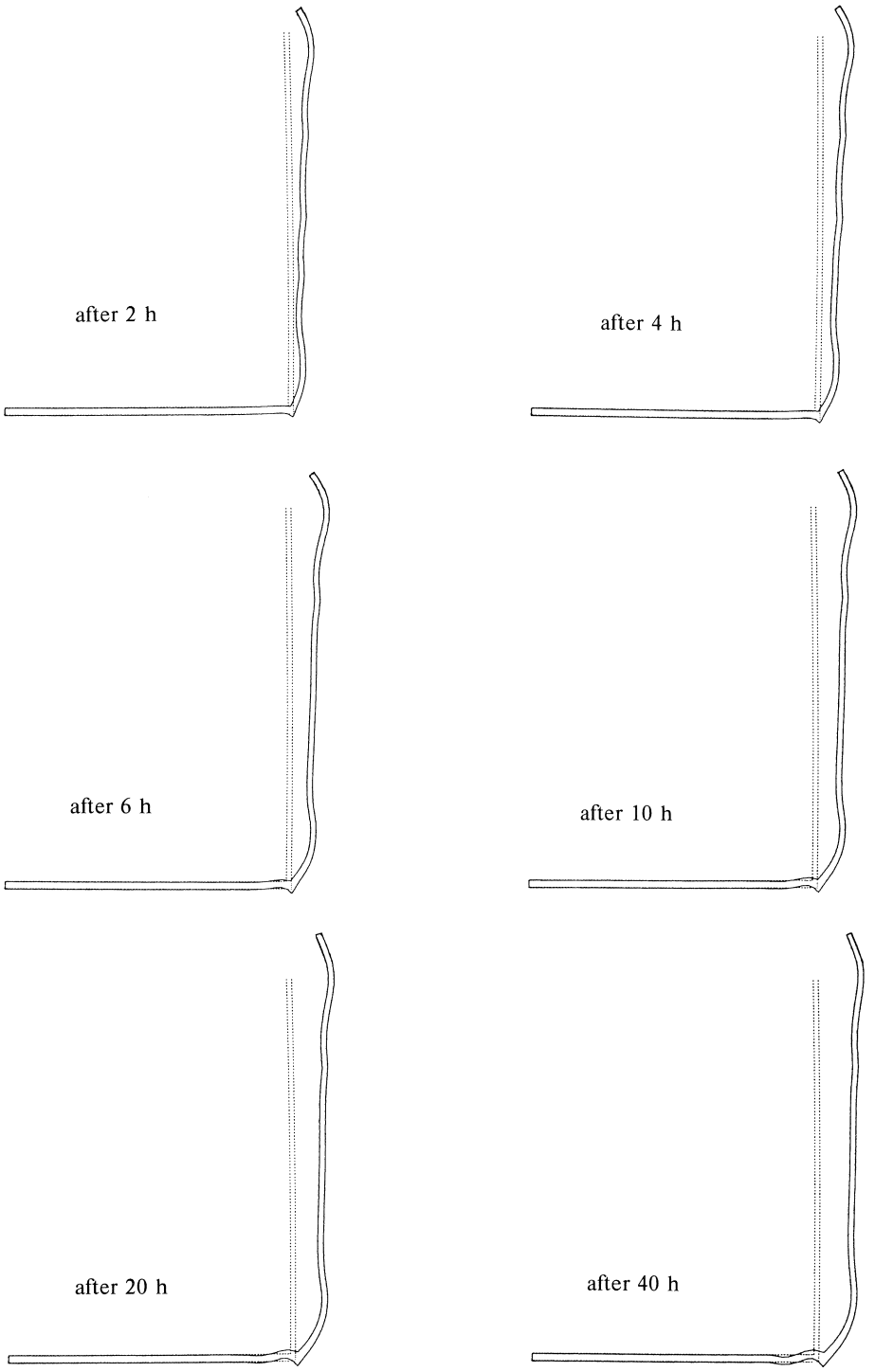


Fig. 6.12b. Deformation of the tank, $t = 2$-$40$ h (25 times enlarged).

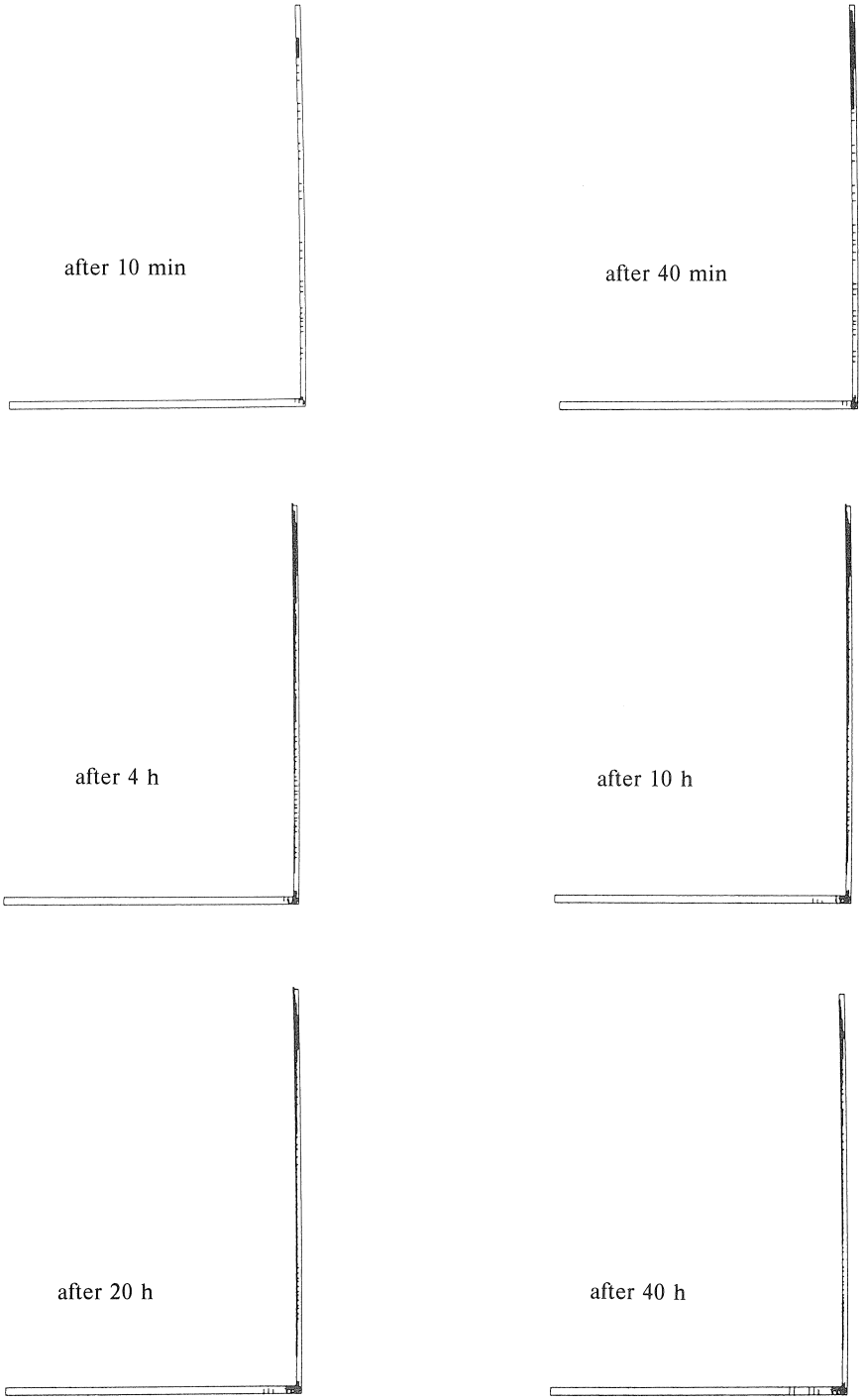


Fig. 6.13. Cracks with crack strain $> 1.0\varepsilon_{us}$.

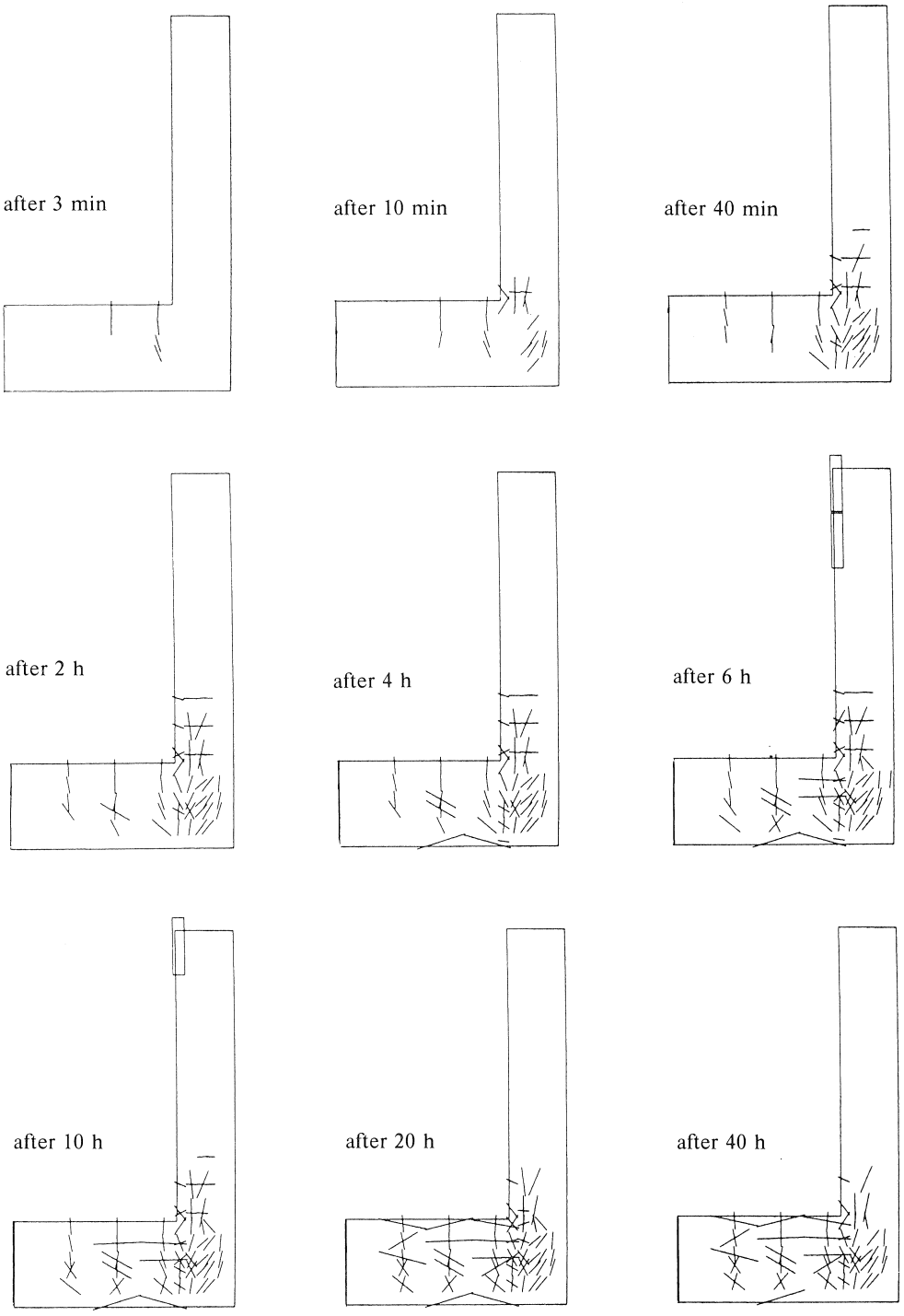


Fig. 6.14. Cracks with cracks strain $> 1.0\varepsilon_{us}$ wall-to-base connection.

Since the cracks which are perpendicular to the tangential direction, i.e. the cracks which are in the plane of the diagrams are represented by rectangles, the dark areas in Fig. 6.13 occur. In Fig. 6.14 a detail of the tank is shown, and some of these tangential cracks are visible.
The first cracks occur on the inside of the tank, which is due to the fact that the temperature reaches the highest level at the outside of the wall. Already after 15 seconds the four cracks which occurred on the outside of the tank due to the prestress are closed again.
The total number of cracks decreases after about 6 hours, as a result of the decreasing temperature gradient in the wall with time.
After 3 minutes the stresses on the outside of the wall are equal to $-30\ N/mm^2$, which is equal to the compressive strength of the concrete. Plasticity should now occur in the lower 1.1 m of the wall, but as already mentioned, this has not been taken into account. The results indicate that after 10 minutes plasticity should occur at least in the lower 14 m of the wall. Because plasticity is not taken into account, the deformations are largely underestimated and will therefore also influence the behaviour of the tank.

## 6.5 *Discussion*

In this example a storage tank comprising a nickel-steel inner and a concrete outer tank has been analysed. The outer tank is reinforced and prestressed.
In the first analysis the concrete tank was subjected to a water test. The crack patterns

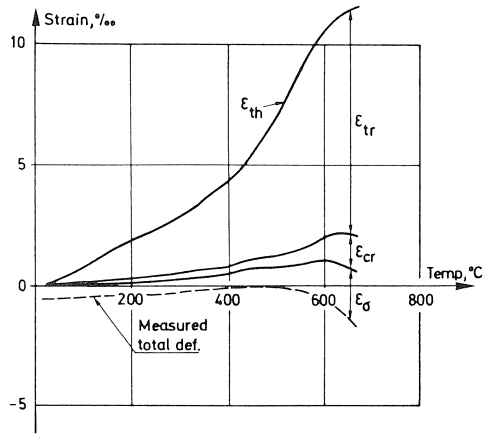


Fig. 6.15. Relation between different strain components.
This diagram gives an indication of different strain components as calculated by a model developed by Anderberg and Thelandersson, 1976.
The load level is equal to 35% of ultimate load.
$\varepsilon_{th}$ = thermal strain, including shrinkage
$\varepsilon_{\sigma}$ = instantaneous, stress-related strain
$\varepsilon_{cr}$ = creep strain
$\varepsilon_{tr}$ = transient strain

which are shown suggest that the tank is well designed: hardly any cracks occur when the water test load is applied.
The second analysis comprised the behaviour of the tank when subjected to a fire load. This fire was assumed to be caused by a burning adjacent tank and lasted approximately 40 hours.
The reported crack pattern and the deformations are in agreement with the expected behaviour. The fact that plasticity could not be taken into account is of course a restriction that should be mentioned. Furthermore, in the numerical analysis only crack strains are calculated.
Another restriction is that the so-called "transient strain" has not been taken into account. This effect comprises the large deformations which concrete can undergo without increase in stress, when subjected to high temperatures (Anderberg and Forsen, 1982; Khoury et al., 1985), see Fig. 6.15.

### 6.6 *Conclusions*

In this example a prestressed concrete storage tank was subjected to a water test and a fire load. The following conclusions can be drawn:
- The water test analysis demonstrated good agreement between "elementary calculations" on the one hand, and "numerical simulation" on the other hand. No cracking was observed when the tank was subjected to the water test, which indicates that the tank was well designed.
- The results of the fire load analysis are presented as numerically calculated crack patterns and deformations, and are in agreement with theoretical considerations. However, one should realise that some simplifications were made in the numerical analysis. The most important ones are that combined plasticity and temperature dependence and "transient strain" effects are not taken into account.

## 7 Beam falling on a shock-absorbing element

### 7.1 *Introduction*

In the late seventies the Institute of Structural Engineering of the Swiss Federal Institute of Technology in Zurich started a test series under the title "Experimental and Numerical Investigations of Reinforced and Prestressed Concrete Beams for Shock Loading".
The object of these investigations was to ascertain the energy-absorbing capacity of concrete in its plastic range. The tests are reported by Ammann et al., 1981 and 1982. Now - more than 5 years later - considerably more is known about the material properties of reinforced concrete under dynamic loading and finite element programs, as DIANA make it possible to perform dynamic non-linear calculations. Hence the results of the test-series of Zurich can now be obtained numerically.
This example of a beam falling on a shock- absorbing element will demonstrate this.

## 7.2 *Description of the experiment*

In the test-series - of which one test has been chosen for simulation with DIANA - 8.15 m long beams are supported by means of a hinge at one end around which it can rotate freely in a vertical plane (Figs. 7.1, 7.2). The other end of the beam is lifted vertically to the desired drop-height H by means of an overhead crane and then released. The beam falls onto a shock-absorbing element and undergoes severe bending within fractions of a second (Fig. 7.3) after striking the shock absorber.

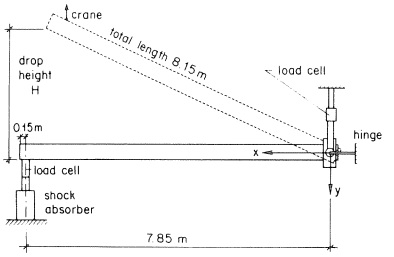


Fig. 7.1. Test set-up. The beam is hinged at one end and can be rotated in a vertical plane. The other end of the beam is lifted to a height of 3.75 m and dropped onto a fixed shock-absorbing element.

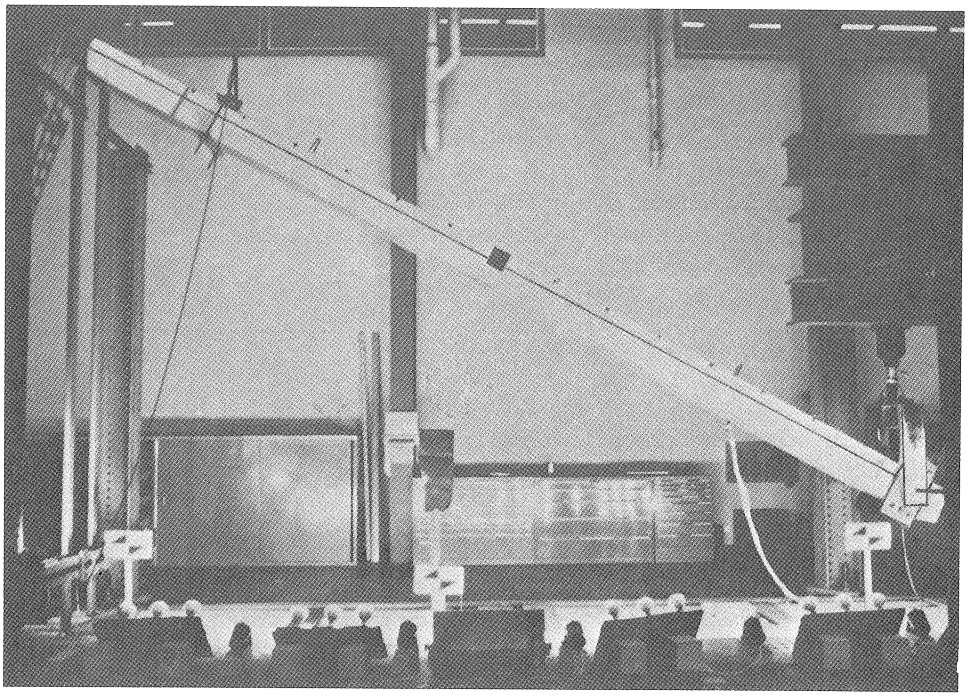

Fig. 7.2. Beam B1 raised to a height of 3.75 m. The black longitudinal line and the triangular markings on the upper edge of the beam serve as reference marks for defining the deflected shape in the film.

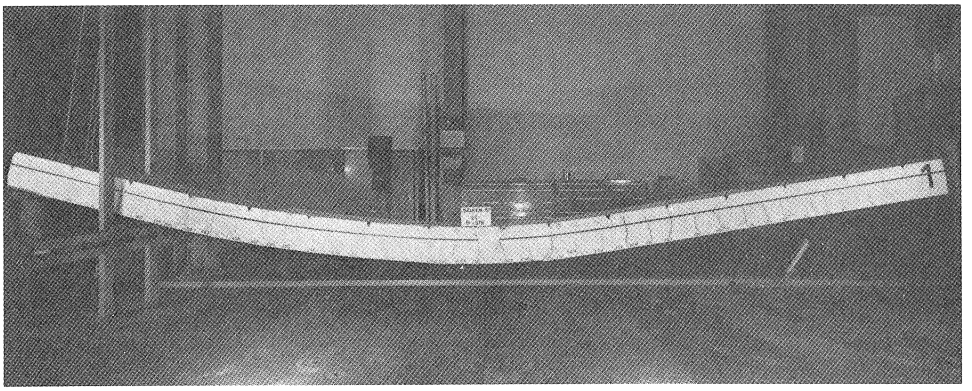

Fig. 7.3. Beam B1 after the test. The permanent maximum deflection is 0.59 m.

After a maximum deflection is reached the beam vibrates, provided that it does not rupture due to failure of the steel. When the vibrations die away the final value of deflection is reached.

Several characteristic values of the beam were simultaneously and continuously registered. Typical results are shown in Fig. 7.4. In addition, each test is photographed at the rate of 1000 exposures per second. The film is also used for evaluation purposes (Figs. 7.5 and 7.6).

A total of 23 beams were tested, the following parameters being varied:

- shape of cross-section (rectangular or T-shaped);
- quantity of reinforcing steel (0.20 to 1.50% of the concrete area);
- type of reinforcing steel (hot rolled, cold worked, high strength);
- degree of prestressing;

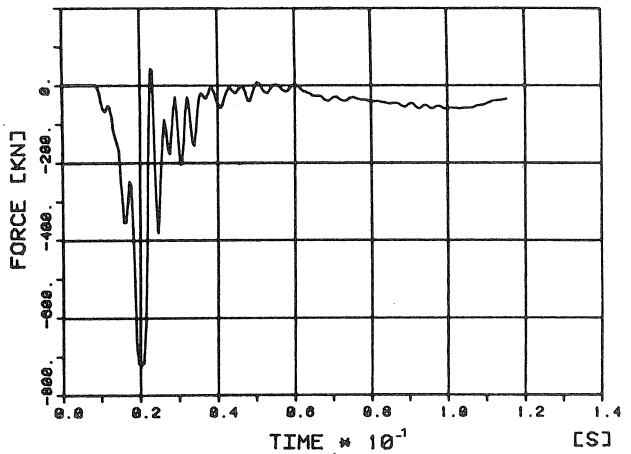


Fig. 7.4. Force-time relationship of the shock-absorbing element measured on the top of the shock absorber for beam B1. The zero response of the shock absorber during the first 0.01 s is incomprehensible.

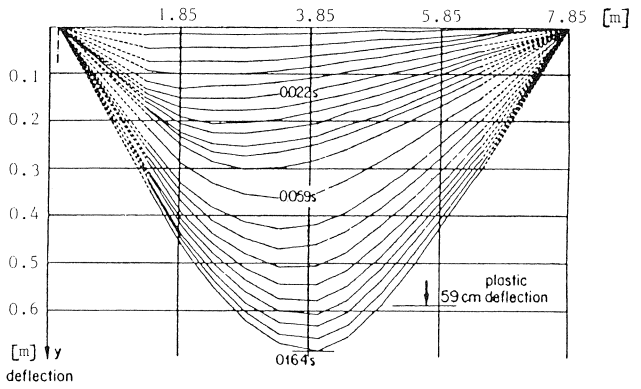


Fig. 7.5. Deflected shapes of beam B1. The maximum deflection of 0.65 m occurs at a distance of 4.05 m from the shock absorber. These deflected shapes have been determined directly from the film.

- mass of beam (could be doubled by using lead sheets);
- method of testing (single or multiple drops);
- type of shock-absorbing element.

The test specimen which was labelled "B1" in the tests at Zurich was chosen for the calculation. The basic idea behind this choice is that not too many difficulties must be combined with the dynamic calculation. In this way the results of the calculation can be shown in their most elementary aspect, not overlaid with other problems.

When this basic idea did not impose the choice of a certain parameter, an average value was chosen for the parameter. These "rules" led to test-specimen "B1". It has a rectangular cross-section(0.4 m deep; 0.3 m high), 0.56% hot-rolled reinforcing steel, no pre-

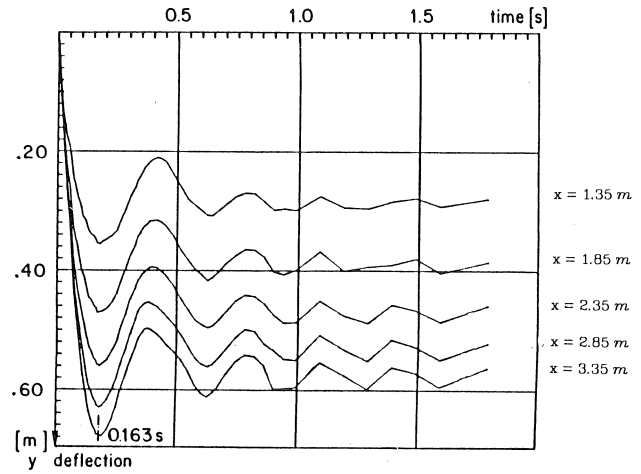


Fig. 7.6. Deflection-time relationship for selected points of beam B1 as determined from the film. The locations of the points are referenced by means of their distance from the shock obsorber. The maximum deflection is reached after 0.163 s.

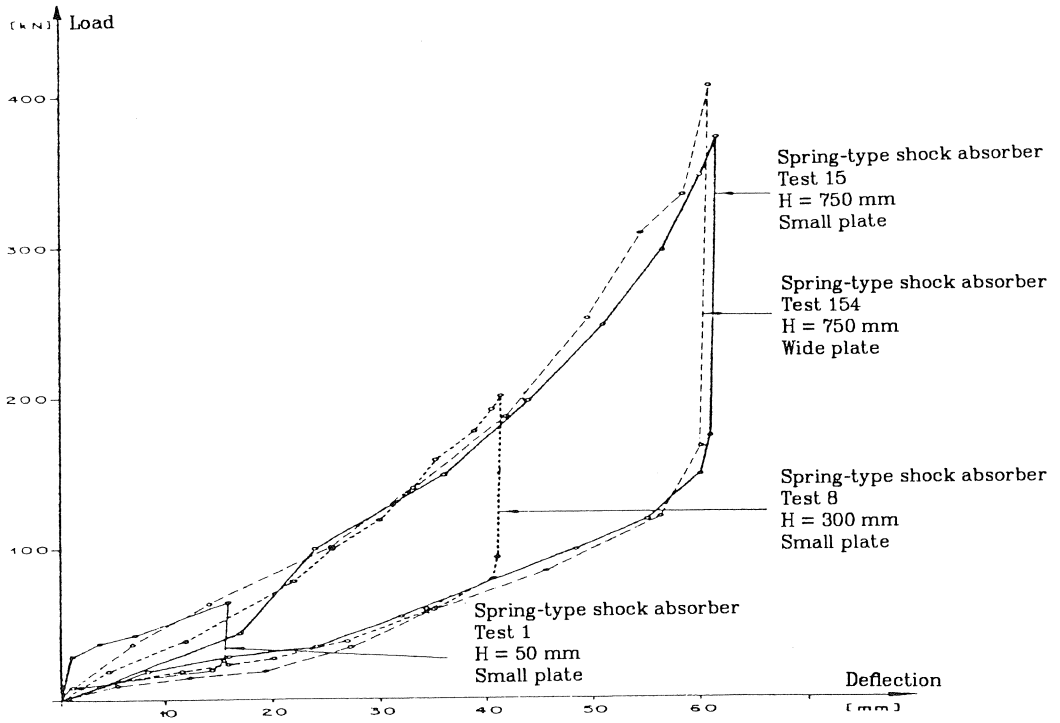


Fig. 7.7. Load-deflection characteristic of the spring-type shock absorber with different concrete-protecting steel plates and different drop heights ($H$).

stressing and no extra mass (i.e. 2470 kg/m$^3$). It was dropped only once from a height of 3.75 m onto a spring-type shock absorber. The load-deflection characteristic of this shock absorber - as determined by tests - is given in Fig. 7.7.

## 7.3 *Parameters for the analysis*

### 7.3.1 Element discretization

In the numerical analysis the beam is schematized with plane stress elements comprising eight nodes (Fig. 7.8). So the actual beam is simplified to a two-dimensional problem.

In the test the part of the beam that hits the shock absorber was protected by a steel plate to prevent crushing of the concrete. In the calculation this is simulated by leaving the four elements above the shock absorber linear-elastic. This avoids modelling of extra steel elements, but creates a somewhat different introduction of the force from the shock absorber into the beam.

The hinge is modelled as a vertically and horizontally supported point. The location of this hinge is the same as it was in the test: at 0.15 m from the right end of the beam, at mid-depth of the cross-section.

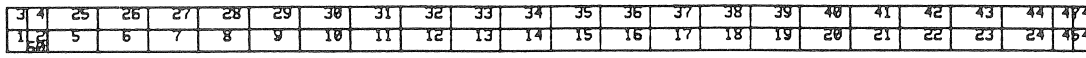

Fig. 7.8. Element mesh. On the left under the beam element No. 50: the shock absorber. Over the shock absorber the four elastic concrete elements. On the right in the middle of the four square elements: the hinge (not shown).

### 7.3.2 The shock-absorbing element

The spring-type shock-absorbing element is schematized by a spring with a load-deflection characteristic comprising three branches (Fig. 7.9). Because at the time of calculation a more advanced spring was not available in DIANA, this spring is hyper-elastic, which means that the loading and unloading paths of its load-deflection curve are the same.

In reality the shock-absorbing element will show a considerable amount of hysteresis. A part of the energy in the beam will be absorbed by the shock absorber. In the calculation this energy must be absorbed by the beam, which will cause some more cracking than in reality.

Also, the load-time curve of the shock absorber will be somewhat different from reality. A slack negative branch of the spring is modelled (upward movement of the beam). This part of the load-deflection curve has a non-zero stiffness to prevent numerical problems.

One more remark about the shock absorber must be made. The load-deflection curve of Fig. 7.7 shows the behaviour of the shock absorber only up to a load of about 400 kN.

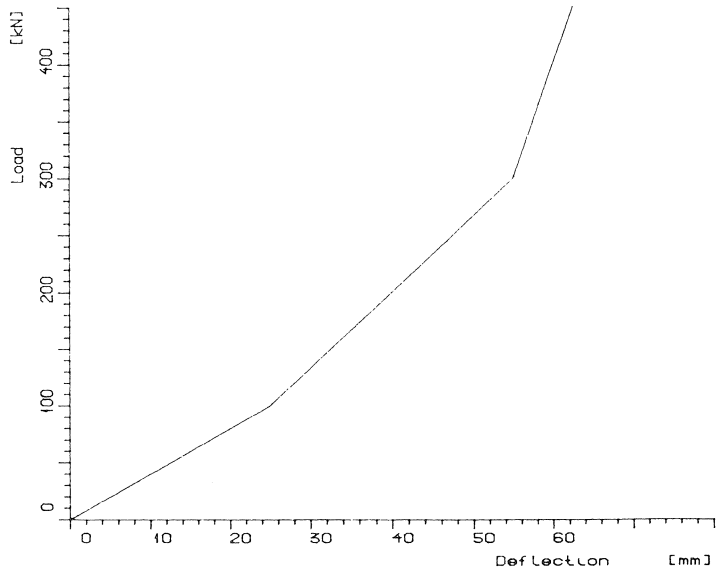


Fig. 7.9. Load-deflection curve of the shock-absorbing element as modelled in the numerical analysis. The negative branch with a small stiffness that is modelled for numerical reasons is not shown.

The load-time curve of Fig. 7.4 shows that the forces in the buffer in the actual test increase to 720 kN. Owing to lack of information on the loading-region between 400 and 720 kN it is assumed that the third branch extends into this region as well. This necessary assumption may influence the compatibility between the analytical results and the measurements during the test.

### 7.3.3 Material parameters

Ammann et al. 1982 do not give all the material properties of beam B1 which are needed for the analysis, and some had to be derived with the aid of known design formulas. From the compressive strength of the concrete the tensile strength was calculated as follows:

$$f_{ct} = \left(f_0 + \frac{f_{cc}}{20}\right) \text{N/mm}^2 \tag{7.1}$$

in which $f_0 = 1$ N/mm$^2$.
The material response is different under dynamic conditions (e.g. Van der Veen and Blaauwendraad 1983, CUR 1982 and Müller et al. 1983), and in order to calculate the material parameters the strain rates in the material must be known. Strain rates of $10^{-6}$ to $10^{-5}$ s$^{-1}$ can still be regarded as static loading. At these rates no increase in strength of stiffness are to be expected.
From a preliminary linear-elastic calculation strain-rates of $2.5 \times 10^{-3}$ to $25 \times 10^{-3}$ s$^{-1}$ were expected in the present case (1000 to 10000 times higher than a "static" loading). From CUR (1982) it emerges that at constant strain rates of this order the tensile strength of concrete is about 1.5 times higher than in a static case. But from the same report it appears that under load repetition the tensile strength decreases again: from $0.8f_t$ with $N = 100$ to $0.5f_t$ with $N = 2 \times 10^6$. Because the first stress wave in the beam will be of great importance to the crack formation in the beam a tensile strength of 1.5 times the static strength is used in this calculation, i.e.:

$$f_{ct,dyn} = 1.5 f_{ct,stat} \tag{7.2}$$

From Van der Veen and Blaauwendraad (1983) it can be learned that at these strain rates hardly any increase in compressive strength or Young's modulus can be expected. The same authors show that an increase in the yield stress of the reinforcing steel can be expected at a higher loading rate:

$$\frac{f_{sy,dyn}}{f_{sy,stat}} = 1 + \left(\frac{\dot{\varepsilon}_s}{40}\right)^{1/5} \tag{7.3}$$

In this formula $\dot{\varepsilon}_s$ is the time-derivative of the steel strain in s$^{-1}$. More recent investigations show the influence of dynamic loading on the yield stress of reinforcing steel to be much lower: the factor "40" in (7.3) should in fact be considerably higher.
No influence on Young's modulus of the reinforcing steel is mentioned by Van der Veen and Blaauwendraad (1983).

Based on the above considerations relating to material properties under dynamic loading, and the material models as explained in the introductory chapter, the following material properties are adopted:

*Concrete*
$E_c = 39750$ N/mm$^2$
$\nu = 0.2$
$f_{ct} = 4.8$ N/mm$^2$
$f_{cc} = 43.8$ N/mm$^2$
$\varrho = 2470$ kg/m$^3$
tension cut-off 1
$\varepsilon_{us} = 0.0027$
$\beta = 0.2$

*Reinforcing steel*
$E_s = 210000$ N/mm$^2$
$f_{sy} = 650$ N/mm$^2$

The value of $\varepsilon_{us}$ is calculated with the tension stiffening concept based on the static yield stress of the reinforcing steel. No bond-slip is modelled, and "perfect bond" is assumed. The material properties are not varied in the analysis.

### 7.3.4 Velocity field

In the test the beam is supported by a hinge at one end. The other end is kept 3.75 m above the shock absorber. Next, this end falls onto the shock absorber.
The calculation starts at the instant when the beam strikes the shock absorber. At that instant the time is set to zero ($t = 0$ s). Consequently at $t = 0$ s the beam is "loaded" with a velocity field. The calculation (manually performed) of this vertical velocity field results in a triangular field:

$$\dot{w}_0(x) = \frac{(l - x)}{l} \sqrt{3gH} \tag{7.4}$$

in which

$\dot{w}_0(x)$ = initial velocity at point $x$
$x$ = ordinate along the bar axis (measured from the shock absorber)
$l$ = length of the beam between hinge and shock absorber (7.85 m)
$g$ = acceleration of gravity (9.81 m/s$^2$)
$H$ = drop height (3.75 m)

The horizontal velocities and the rotations at $t = 0$ s are neglected as well as the initial deformations and the initial stresses in the beam.

### 7.3.5 Type of numerical time-integration method

A choice must be made between implicit and explicit numerical time-integration methods. Dealing with an implicit method in every time step a set of equations must be evaluated by decomposition of matrices. The form of the equations depends on the

type of implicit method used. In an explicit method the equations can be solved directly, but explicit methods are numerically less stable than implicit ones. All explicit methods and some implicit methods are conditionally stable (i.e. the time step is limited by numerical stability); other implicit methods are unconditionally stable.
In structural dynamic calculations, in which the loading does not contain the highest frequency components, mostly implicit numerical time-integration methods are used. In this analysis the Newmark implicit method is chosen, which is an unconditionally stable method (provided that the proper time-integration parameters are used; see Bathe (1982)).

### 7.3.6 Lumped or consistent mass matrices

Another choice is between the use of lumped and consistent mass matrices. Experience shows that there is less integration inaccuracy in the combination implicit method /consistent mass matrix than in the combination implicit method/ lumped mass matrix. Therefore a consistent mass matrix has been chosen.

### 7.3.7 Magnitude of the time step

From experience it can be stated that dynamic wave propagation (including the shear deformation) can be satisfactorily simulated with plane stress elements, provided that the elements are "small enough", a condition which seems to be satisfied in this case. If a conditionally stable time-integration method were used (which is not the case), the magnitude of the time step would have to be smaller than the critical time step. Belytschko and Hughes (1983) (page 102) show how the critical time step should be calculated in some very simple cases. With the parameters chosen in this analysis this should lead to a critical time step of about $5 \times 10^{-6}$ s. By calculating with a time step smaller than the critical time step, waves in the smallest elements can also be well distributed in conditionally stable time-integration methods.
Because an unconditionally stable time-integration method is chosen (see 7.3.5), this very strict rule does not have to be obeyed to obtain a numerically stable process. In this case the choice of the magnitude of the time step is not completely free, however, but is governed by rule-of-thumb (see Bathe (1982)) by means of which it is endeavoured to incorporate an adequate frequency range in the analysis. The time step must be approximately 20 times smaller than the time step that corresponds to the highest frequency in the loading spectrum.
As indicated by Fig. 7.4, the shock absorber seems to respond with a highest frequency of about 200 Hz, and from Fig. 7.6 the beam seems to respond with a frequency of about 3 Hz. In most cases the frequencies involved will not be known and will have to be estimated. For a more detailed analysis of the frequencies of the beam and the shock absorber see Section 7.4. Based on the frequency of 200 Hz, the time step must be smaller than:

$$t = \frac{1}{20 \cdot 200} = .00025 \text{ s} \tag{7.5}$$

As appears from Fig. 7.5, it seems interesting to continue the analysis at least up to 0.164 s. With a time step of (e.g.) $10^{-4}$ s this means that more than 1600 time steps have to be applied which was at first considered to be practicable in the context of this example.
Later on it appeared that this magnitude of the time step ($10^{-4}$ s) would require too much (elapsed) time for completing the analysis; so the time step was increased to $10^{-3}$ s (coping with frequencies up to only 50 Hz, not enough to simulate Fig. 7.4 very well).

### 7.3.8 Analyses performed

In this example three different analyses were performed:
1. linear-elastic dynamic analysis: to check the input and to obtain an idea of the strain rates that occur in the experiment;
2. calculation of eigenfrequencies: to obtain an idea of the frequencies that can play a role in this example;
3. non-linear dynamic analysis: the results of this (main) part of the example are compared with the results of the experiment in Zurich.

## 7.4 *Results*

### 7.4.1 Linear-elastic dynamic analysis

By performing a linear-elastic dynamic analysis the input data could be checked. The linear-elastic deflection curves were qualitatively the same as the deflection curves from the experiment (Fig. 7.5). The point of maximum deflection shifted from the shock absorber to the middle of the beam. The deflections were smaller, of course, because the beam was not allowed to crack. Evaluation of the shear force in the beam near the hinge gave an idea of the stress and strain rates that occur in the beam. These stress and strain rates were used for determining the dynamic material properties for the non-linear dynamic analysis (see Section 7.3.3).

### 7.4.2 Eigenfrequencies

The eigenfrequencies are calculated in two situations: the unloaded (linear-elastic) beam and the cracked beam at $t = .150$ s. In both situations 10 eigenfrequencies were calculated. The results are assembled in Table 7.1.
As expected, the lowest eigenfrequency of the beam is even lower than 10 Hz and the cracked beam is less stiff than the linear-elastic beam (which means lower eigenfrequencies). As mentioned earlier, in the main calculation only frequencies less than 50 Hz can be simulated.

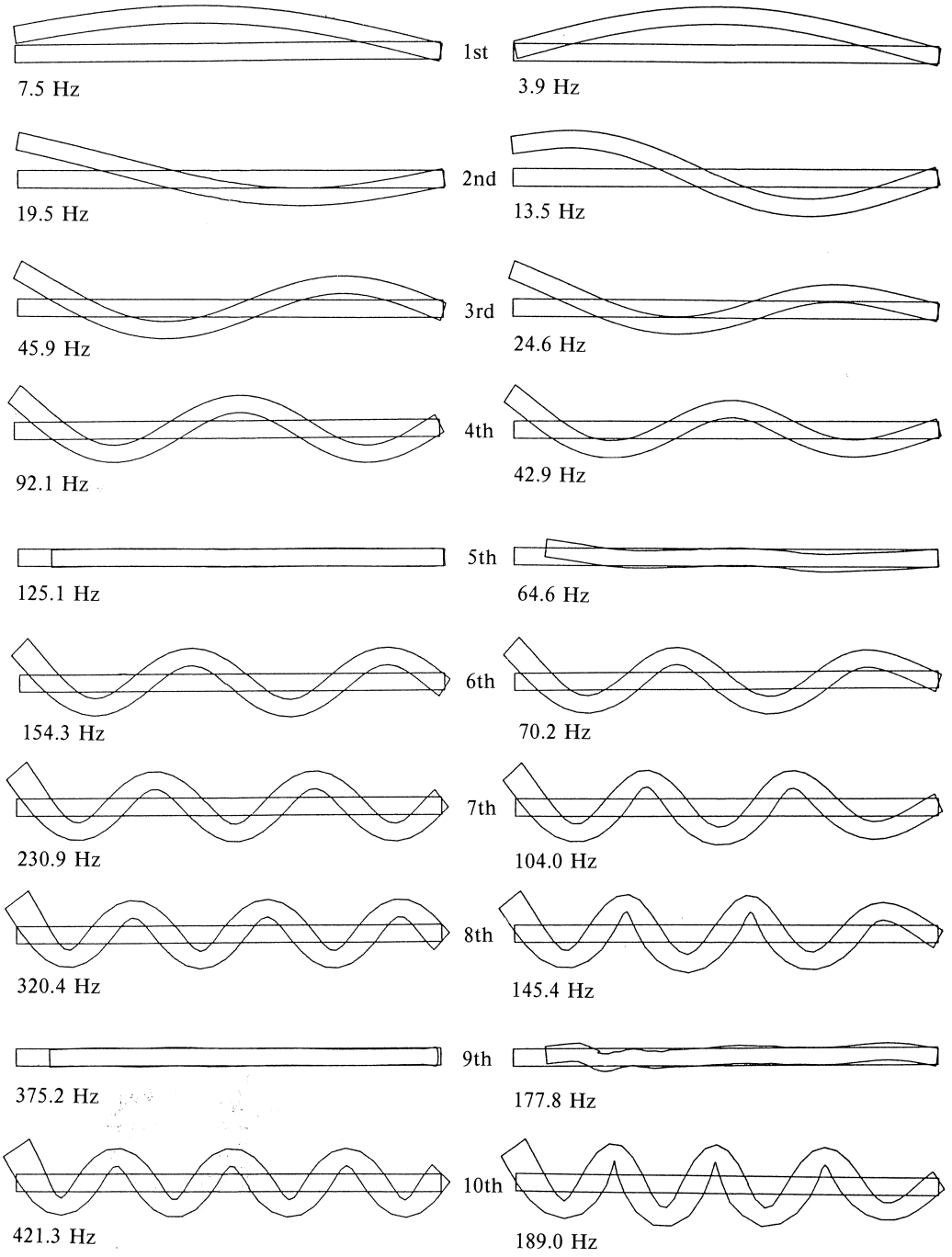


Fig. 7.10a. The first 10 eigendeformations of the linear-elastic beam.

Fig. 7.10b. The first 10 eigendeformations of the cracked beam at $t = 0.150$ s.

In the test the first eigenfrequency was measured too. For the uncracked beam the first eigenfrequency was 8.14 Hz and for the cracked beam 3.75 Hz[1].
Fig. 7.10 gives the shapes of the eigendeformations corresponding to the ten lowest eigenfrequencies, both for the linear-elastic beam and for the (cracked) beam after $t = 0.150$ s. The overall shapes of these eigendeformations are the same for the cracked and the uncracked beam, only the curves of the eigendeformations of the cracked beam are sharper (because it is less stiff).

Table 7.1 Calculated eigenfrequencies at $t = 0$ and 0.150 s

| | eigenfrequencies of the beam in Hz | |
|---|---|---|
| no. | at $t = 0.000$ s (linear) | at $t = 0.150$ s (cracked) |
| 1st | 7.5 | 3.9 |
| 2nd | 19.5 | 13.5 |
| 3rd | 45.9 | 24.6 |
| 4th | 92.1 | 42.9 |
| 5th | 125.1 | 64.6 |
| 6th | 154.3 | 70.2 |
| 7th | 230.9 | 104.0 |
| 8th | 320.4 | 145.4 |
| 9th | 375.2 | 177.8 |
| 10th | 421.3 | 189.0 |

### 7.4.3 Progress of the non-linear dynamic calculation

As mentioned in Section 7.3.5, the analysis was started with time steps of 0.0001 s. For the non-linear phenomena the modified Newton-Raphson method was used. With this method at every iteration a new stiffness matrix is calculated. This worked quite well until time step No. 200 (viz. the energy variation in one time step mostly decreased by a factor of $10^4$ in less than 10 iterations). After step 200 and especially at step 204 to 206 the process diverged, and the specified accuracy was not obtained (viz. $10^4$ in not more than 10 itertions). The energy variation within one time step increased when more iterations were carried out.
This phenomenon is known from static calculations. It occurs when after a descending part of the load-deflection curve this curve increases again. With the modified Newton scheme too small a stiffness is calculated in the descending branch and no equilibrium can be found in the ascending part. The solution is to take the linear stiffness matrix (the stiffness as it was at the beginning of the calculation) and to keep it constant during the entire calculation. A disadvantage of this method is that it converges rather slowly (because the linear stiffness matrix sometimes differs considerably from the moment-

[1] In the experiment in which the eigenfrequencies were determined, probably lower strain rates occurred than in the main experiment and, consequently, other dynamic material properties were involved. This is one of the reasons for the differences between the experimental and the numerical first eigenfrequencies.

ary stiffness of the structure). But divergence problems as described above occur less easily.
This method is applied in this dynamic calculation too. The idea was that also in this calculation the divergence may be caused by a dip in the "load"-deflection curve. In this case the "load" must be explained as a combination of accelerations. So the calculation was restarted at time step 200 with the linear stiffness-matrix. This worked well.The time steps 204 to 206 could be calculated, although the convergence was not very good (a factor of 100 in the decrease of the energy variation within one time step was not reached in 10 integration steps). In the subsequent time steps the convergence became increasingly better.
So this calculation could be continued, and 250 time steps were analyzed.
It appeared, however, that one time step took about 200 CPU s (on the current hardware configuration). Including the drawing of some diagrams every 50 time steps, each day only 50 time steps could be calculated. So the complete analysis of at least 1600 time steps would have taken more than a month. A major part of the numerical facilities of the Institute would have been occupied by this analysis for a whole month. So it was decided to increase the magnitude of the time steps to $10^{-3}$ s, though knowing that the highest frequency that is satisfactorily calculated with this time step would drop to 50 Hz.
To increase the magnitude of the time step in the actual version of DIANA the calculation had to be restarted at $t = 0$ s. An implicit advantage of this is that the results of the two calculations can be compared. It appeared that (in the first 0.025 s) the deflection curves at comparable time steps showed only minor differences. However, the crack patterns showed one striking difference. The analysis with the small time steps revealed some (not opened) cracks at the upper edge at the hinged end of the beam. The first crack arose at 0.015 s at approximately two metres from the hinge. At 0.025 s all these cracks "closed" again. None of them reached the maximum crack strain $\varepsilon_{us}$, and none of them increased further than about one third of the depth of the beam. In the crack patterns of the calculation with the larger time steps these cracks were not observed.
The analysis with larger time steps was first started with the (faster) Newton-modified iterative scheme. However, already at time step No. 12 the analysis diverged, and the calculation was restarted with the constant (linear) stiffness-matrix. No differences in results between both (non-linear) iteration methods were observed.
In this report only results of this last analysis with time steps of $10^{-3}$ s and the constant (linear) stiffness matrix method are presented.

### 7.4.4 Response of the shock absorber

The calculations of the shock absorber are shown in Fig. 7.11. Note that the scale on the horizontal axis is $10^{-1}$ s, just as in Fig. 7.4, which shows the response of the shock absorber in the experiment. Fig. 7.11 has been corrected for the incomprehensible zero response during the first 0.01 s as presented in Fig. 7.4. Having done so, the two diagrams can be compared. As expected, the response in the numerical analysis is

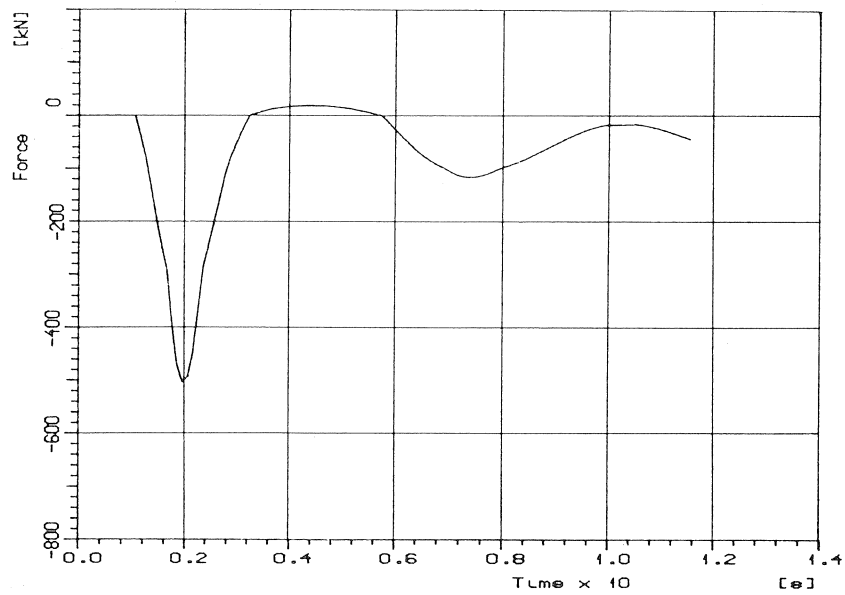


Fig. 7.11. Force-time relationship of the shock-absorbing element as calculated in the numerical analysis. It is corrected for the incomprehensible zero response during the first 0.01 s as is shown in Fig. 7.4 to make the two diagrams comparable.

"smoother" than in reality. This is due to the larger time step, which smoothes out the higher frequencies in the analyses.
Where in reality the maximum force in the shock absorber is about 720 kN, in the analysis it is about 500 kN. One of the possible reasons for this is the unknown behaviour of the shock absorber at forces higher than 400 kN. It is quite possible that the assumed behaviour is not in accordance with reality (see paragraph 7.3.2).
Because of an incorrect unloading path in the model of the shock absorber (again see Section 7.3.2) the descending branch of the diagram between 0.02 and 0.03 s is calculated not steep enough.

### 7.4.5 Deflection of the beam

Fig. 7.13 shows the deflection curves during the first 150 time steps (= 0.150 s). Every 0.010 s one line is drawn. This diagram can be compared with Fig. 7.5, which gives the same curves for the experiment (but at different times and intervals). There is a very good qualitative agreement between these two figures. The point of maximum curvature shifts from the shock absorber to the middle of the beam. In the test a maximum deflection of 0.69 m is reached at $t = 0.164$ s at 4.0 m from the shock absorber; in the calculation the maximum deflection is 0.57 m which is reached at $t = 0.149$ s at 3.6 m from the shock absorber.
For three points of the beam the deflection-time characteristic is given in Fig. 7.13 at

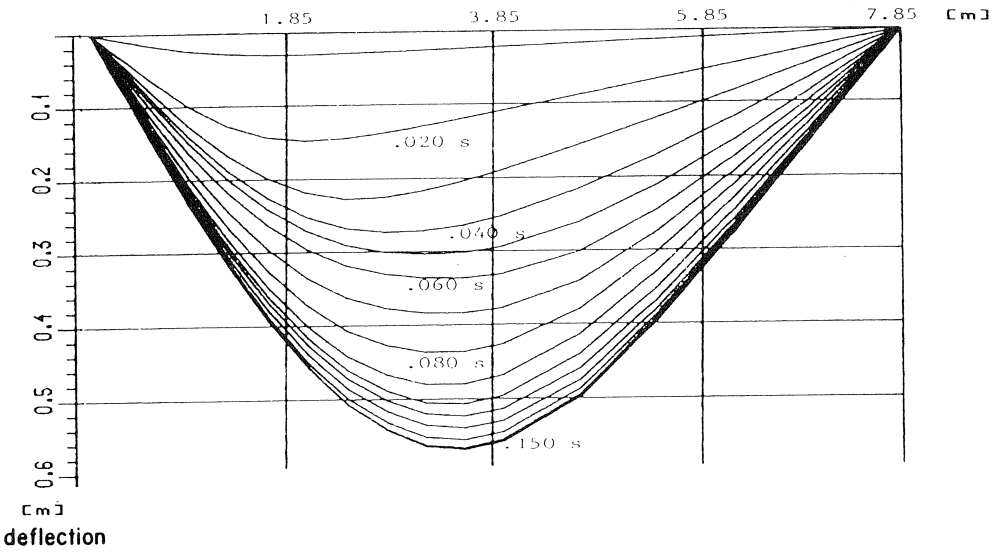


Fig. 7.12. Deflected shapes obtained from the analysis. Comparison with Fig. 7.5 shows that the calculation gives less deflection than the experiment.

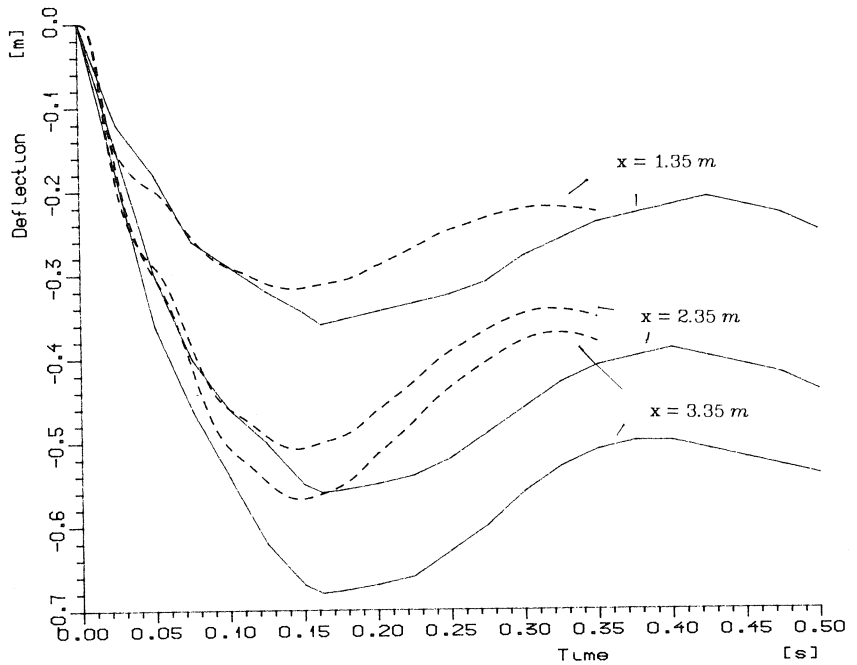


Fig. 7.13. Deflection-time relationship for three points along the beam at 1.35, 2.35 and 3.35 m from the shock absorber. The continuous lines give the results from the experiment (see also Fig. 7.6) and the broken lines give the results of the numerical analysis.

1.35, at 2.35 and at 3.35 m from the shock absorber. The solid lines give the test results and are derived from Fig. 7.6, while the broken lines give the results from the calculation for the same points. The points of maximum deflection are located at $t = 0.163$ s in the experiment, whereas in the calculation they are found at about $t = 0.150$ s, mainly because the maximum deflections are smaller. In fact the complete diagram shows some less deflection for the calculation and a little shorter vibration (higher frequency).

### 7.4.6 Steel stresses

The stresses in the bottom reinforcement were calculated (see Fig. 7.14). The reinforcement is first loaded near the shock absorber: at 1.5 m from the shock absorber at $t \approx 0.005$ s. The reinforcement near the hinge is loaded only later: at 6.5 m from the shock absorber at $t \approx 0.035$ s. This result is as expected.
The steel stresses become negative after about 0.20 s. This is due to the decreasing deflection after 0.15 s. In the experiment, this change of polarity occurred later, because - as discussed before - the decreasing deflection started later than in the numerical analysis.

### 7.4.7 Crack pattern

At time step No. 4 (0.004 s) the first cracks were formed at the lower edge of the beam at a distance of approximately 1 m from the shock absorber. These are typical flexural

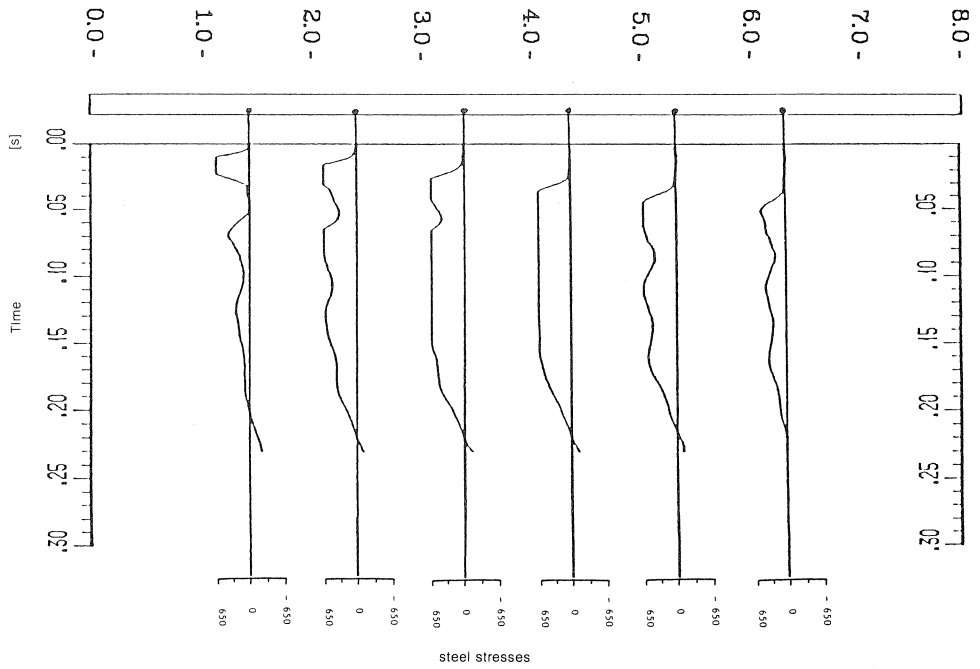


Fig. 7.14. Steel stresses obtained from the numerical analysis.

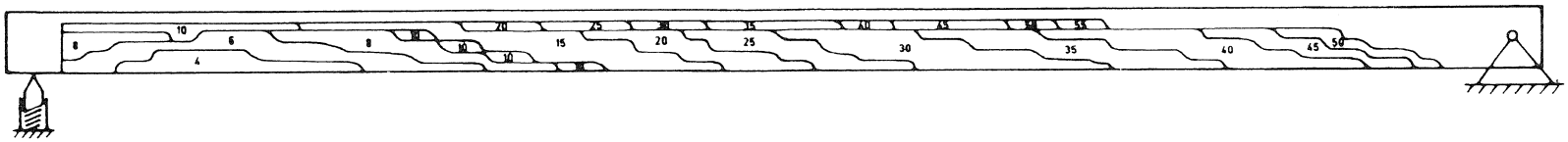

Fig. 7.15. Progress with time of the formation of flexural "cracks" ($\varepsilon = \varepsilon_{ct} = 0.00012$).

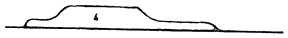


Flexural crack region at time step No. 4

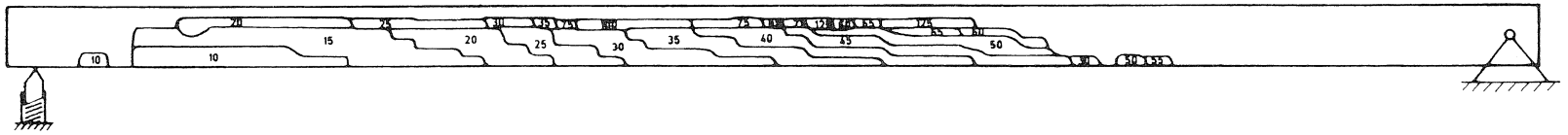

Fig. 7.16. Progress with time of the formation of flexural 'cracks' ($\varepsilon = \varepsilon_{us} = 0.0027$).

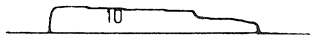


Region with open flexural cracks at time step No. 10

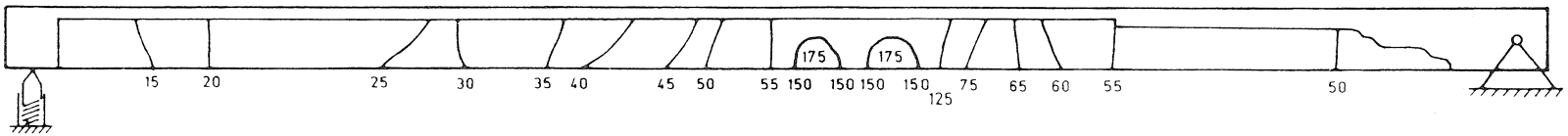


Fig. 7.17. Progress with time of the front of crack-strain decrease ($\varepsilon < 0$).


Location of the front of crack-strain decrease at time step No. 35

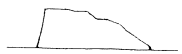

Flexural crack region

cracks. In the following time steps the flexural crack region expanded. This is shown in Fig. 7.15, where the contours are given that enclose at a certain time step all the integration points that are cracked ($\varepsilon > \varepsilon_{ct}$, see Fig. 0.4). The velocity of this expansion in the horizontal direction is about 150 m/s (for comparison: the so-called linear-elastic bar-wave velocity is about 4000 m/s).
No cracks occurred in the four elements over the shock absorber because they were kept linearly-elastic (see Section 7.3.1).
In the first instance, the lower two-thirds of the beam cracked (which implies that cracks arose in the four lower integration points). Five to fifteen time steps later the fifth integration point cracks too. The upper one-sixth of the beam exhibits splitting cracks because of the strong concentration of compressive stresses.
Fig. 7.18 shows some of the calculated crack patterns. At different time steps the integration points are shown where $\varepsilon > \varepsilon_{ct}$ (the crack directions are also indicated).
In Fig. 7.16 the contours are given for the open cracks ($\varepsilon > \varepsilon_{us}$, see Fig. 0.3). The first cracks opened at $t = 0.010$ s. The opening of the cracks spread over the beam in about the same sequence in which they arose. Only the velocity in the axial direction is somewhat lower: $\approx 110$ m/s. As an example, Fig. 7.19 shows the open cracks at some later time steps.

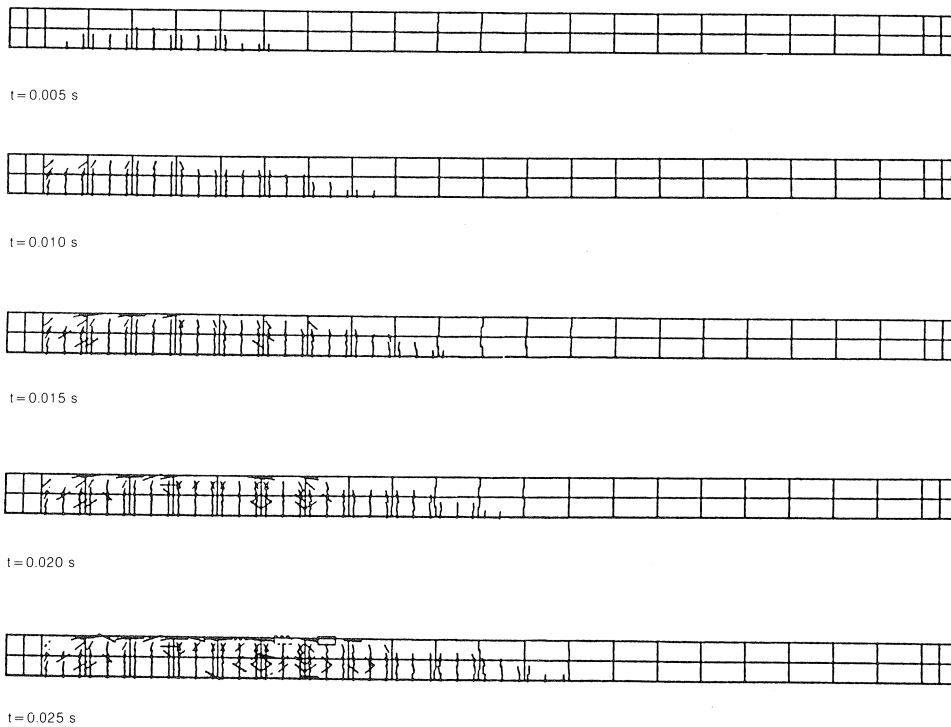


Fig. 7.18. Plots of all "cracks" at several time steps (i.e. all "cracks" with $\varepsilon > \varepsilon_{ct}$).

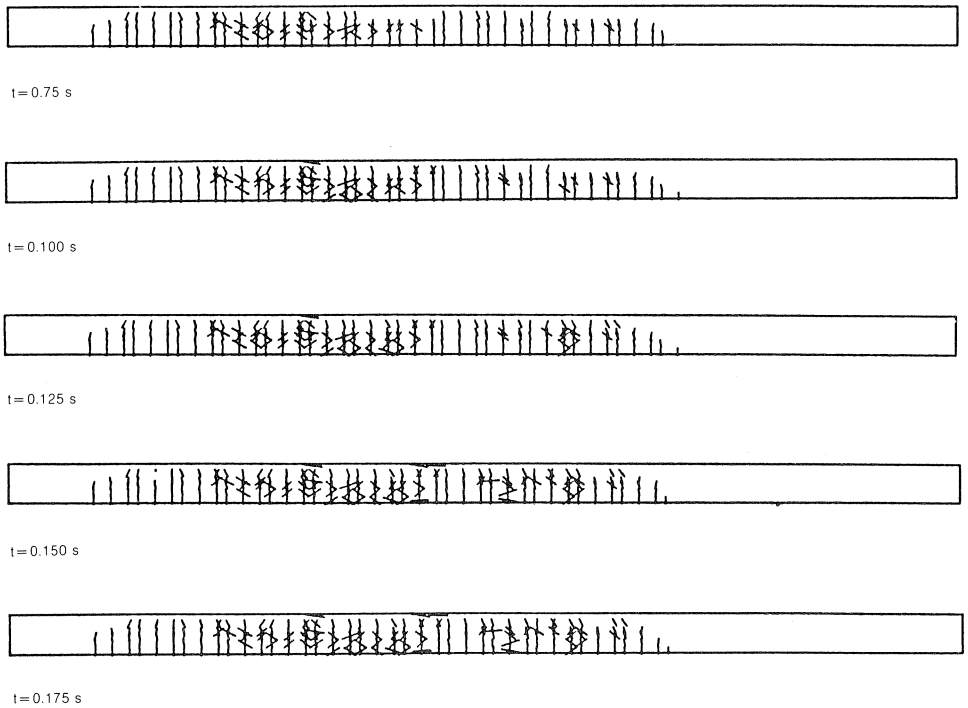


Fig. 7.19. All cracks with crack strain $\varepsilon > \varepsilon_u$ at several time steps. See also Fig. 7.16.

At a certain time step the crack strain of all the cracks decreased (Fig. 7.17), and near the shock absorber this occurred at $t = 0.015$ s. This is probably due to the fact that the point of maximum curvature shifts from here to the middle of the beam.
From $t = 0.050$ s cracks near the hinge also showed a decreasing strain. The last cracks with a negative strain rate are located slightly to the right of the middle of the beam, and the decrease in their crack strain started between time steps 150 and 175. This is in agreement with the fact that the beam moves upwards again after time step 150.
In general, the cracking of the beam is very complex. Existing cracks close temporarily when another crack is formed close by or when a second crack at the same point, but in another direction, develops. In the compressive region, at the upper edge of the beam, splitting cracks in the second (axial) and sometimes in the third (out-of-plane) direction were observed.
The description of the crack behaviour of the beam as given above is intended as an overview of the main features of this behaviour.

### 7.4.8 Velocity field

As described in Section 7.3.4, the analysis is started with a triangular velocity field as an approximation of the real situation of the beam as it hits the shock absorber. Of course, this velocity field changes with time. Fig. 7.20 and Fig. 7.21 give an idea of the develop-

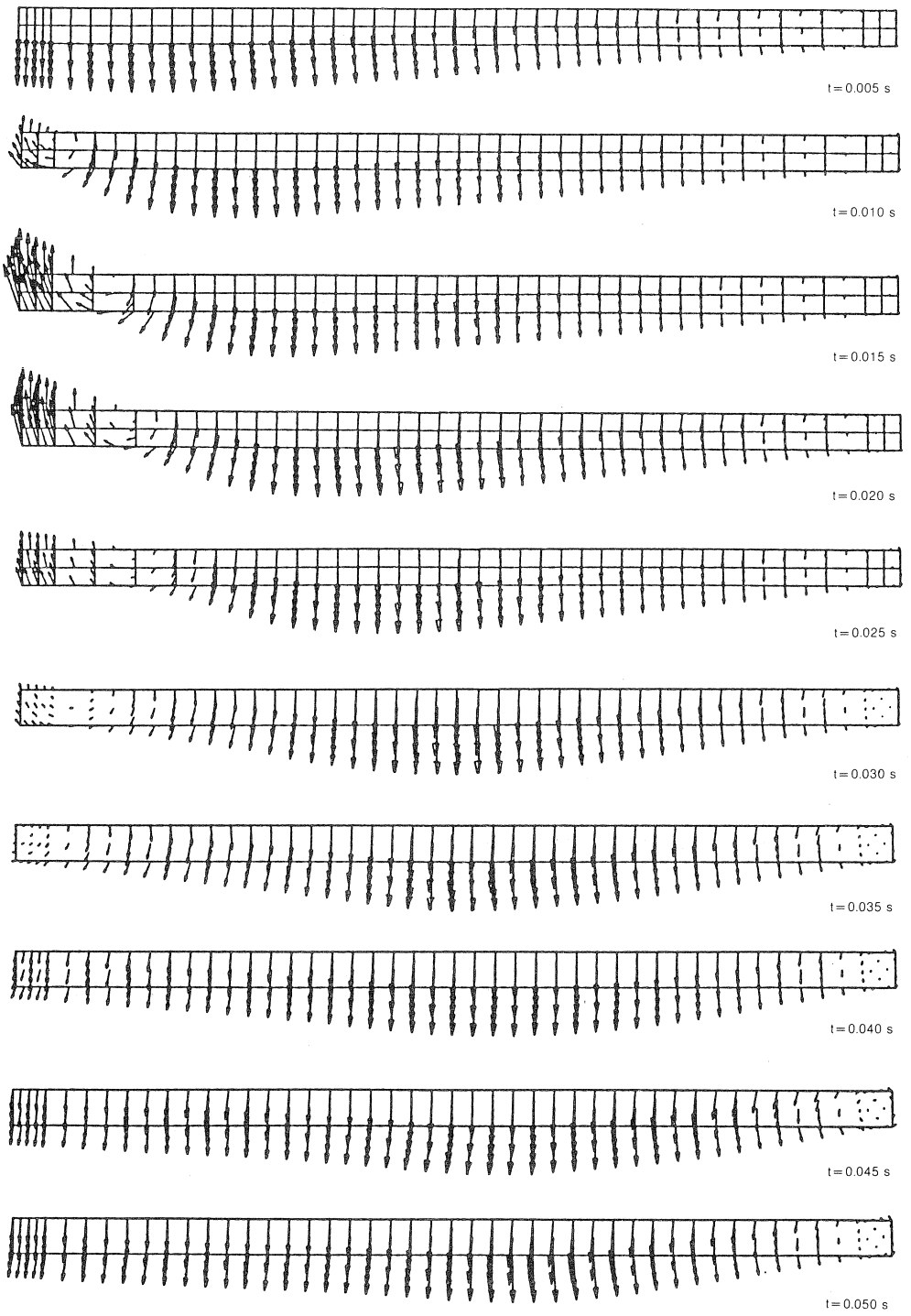


Fig. 7.20. Velocity field during the first 0.050 s as calculated.

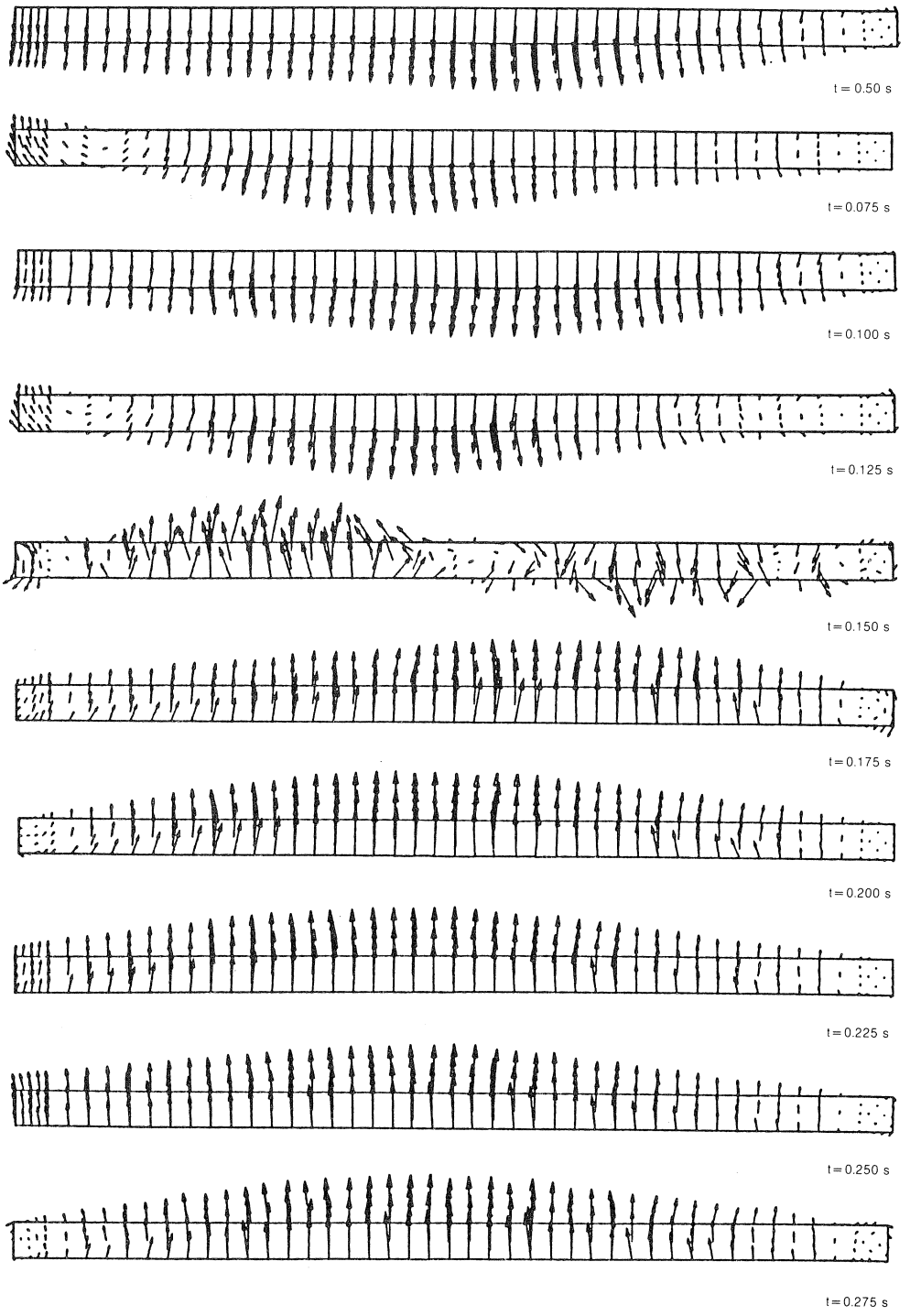


Fig. 7.21. Velocity field from $t = 0.050$ s to $t = 0.275$ s as calculated.

ment of the velocity field. The velocity field at each time step is individually scaled in these two diagrams, and only qualitative comparisons can be made between two time steps[1].
During the first 0.050 s the velocity field moves from the shock absorber to the hinge at a velocity of about 85 m/s. Then it seems to reflect against the hinge and returns to the shock absorber.
Next, at $t = 0.150$ s the direction of the velocities changes. At that particular time step the right and the left part of the beam are moving in opposite directions. As mentioned before, at approximately 0.150 s the beam reaches it maximum deflection in the calculation.

### 7.5 *Conclusions*

It has been shown that a non-linear dynamic finite element analysis is possible. Good results can be obtained.
In the analysis the stiffness of the beam was a little overrated, resulting in somewhat smaller deflections and a higher frequency than observed in the experiment. The influence of dynamic loading on the material properties has possibly been overestimated in the input. But in general the numerical results can stand comparison with the experimental results.

- A non-linear dynamic analysis of a beam with a finite element program is perfectly feasible.
- In the analysis as described here the influence of the dynamic loading on the material properties of reinforced concrete is probably overestimated (see 7.3.3). Further research in this field seems necessary.
- Development of a spring element with hysteresis could improve the results of this analysis because a better model for the shock absorber could then be implemented.
- Such an improvement can also be expected from a concrete model with even better unloading behaviour than the model employed in this analysis.

## 8 Dynamic analysis of underwater tunnel for gas explosion

### 8.1 *Introduction*

Road tunnels that pass under waterways are very common in the Netherlands. They are normally designed to resist the loads associated with soil and water pressure. In the event of an internal gas explosion, the tunnel experiences a load reversal for which it may not be adequately reinforced. Thus, the question whether hazardous cargo should be permitted to pass through such tunnels is of some importance. Of primary concern, of course, is the question whether an accidental gas explosion can cause failure of the

[1] The reason of this is that these diagrams are a compilation of different DIANA plots.

tunnel. But even if the answer to this question were to be in the negative, it would still be important to determine whether the tunnel would be damaged to such an extent that its serviceability is impaired.
The development of non-linear finite element software has advanced to such an extent in recent years that it is now possible to provide rational answers to such questions. It is for this reason that this problem has been included in this book of examples. Actually, the purpose of this example analysis is twofold. First, it is intended to demonstrate that an advanced analysis tool such as DIANA is capable of solving nonlinear dynamic analysis problems, for which it is very difficult if not impossible to find reliable answers by any other means. Second, the analytical approach itself serves as an illustration of how a complex analysis problem should be solved. It is a reminder of the fact that such an analysis is by no means a simple affair. It should be performed only by experienced analyst and can consume considerable amounts of man-hours and computer resources. For this reason, such analyses should be performed only in special situations where it can be shown that no simple analysis methods can provide answers with reasonable accuracy.

## 8.2 *Description of the problem*

The Rijkswaterstaat has developed standard tunnel cross-sections that are widely used throughout the Netherlands. Fig. 8.1 shows a typical cross-section. In order to select a specific structure, the 327 m long Vlake Tunnel for the A58 Highway in Zeeland was

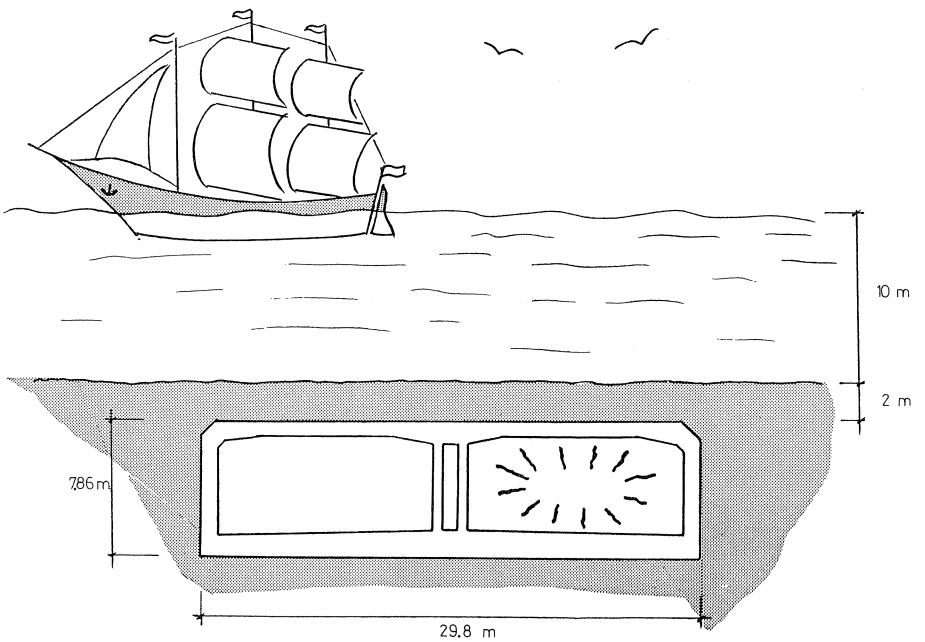


Fig. 8.1. Typical tunnel cross-section.

chosen. It was the purpose of this analysis to predict the response of the tunnel to the pressure load associated with a hypothetical internal gas explosion.
The solution of a problem of this nature requires a careful step-by-step approach, with constant verification of

- the correctness of the program used;
- the correctness of the model chosen;
- the correctness of the results obtained.

In order to achieve these goals, the following analyses were performed:

1. a linear-elastic static frame analysis of the entire tunnel cross-section;
2. a linear static finite element analysis of a segment of the tunnel roof;
3. a non-linear static finite element analysis of the same tunnel roof segment;
4. an eigenvalue analysis of the finite element model;
5. a non-linear dynamic time history analysis of a grossly simplified finite element model;
6. the non-linear dynamic time history analysis of the actual finite element model.

At each step great care had to be taken to verify that the analysis results were reasonable. For this purpose it was very helpful, that a 1 : 5 scale model of this tunnel section had been tested at TNO-IBBC in 1976. The experiment is completely documented in (TNO 1976), which also contains detailed information on dimensions, reinforcement, material properties and service loads on the prototype structure.

### 8.2.1 Description of the structure

Fig. 8.2 shows the detailed dimensions of one-half of the tunnel section, and in Fig. 8.3, the reinforcement is indicated for a 1.5 m wide section of the tunnel.

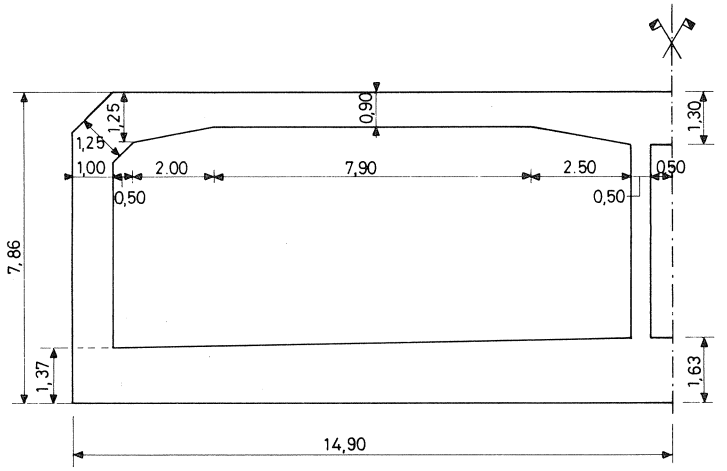


Fig. 8.2. Dimensions of tunnel cross-section.

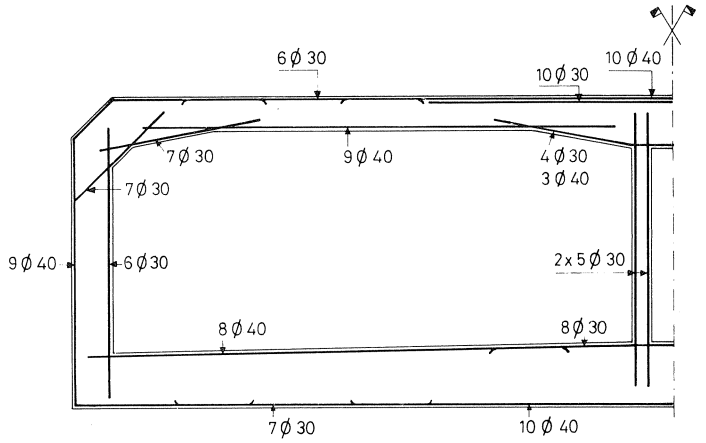


Fig. 8.3. Tunnel reinforcement for a 1.5 m wide section.

### 8.2.2 Material properties

The material properties used in the analysis were based on those reported in the TNO-IBBC report. In the final shock analysis, all the strength parameters were increased by 20% to allow for the strain-rate effect. These increased values are indicated below in parentheses.

*Concrete*
$E_c =$ 22000 N/mm$^2$
$\nu =$ 0.2
$f_{ct} = 2.8$ (3.36) N/mm$^2$
$f_{cc} =$ 25 (30) N/mm$^2$
tension cut-off 1
$\varepsilon_{us} = 0.0010$
$\beta = 0.2$
Note that the Von Mises yield criterion was used in this example, as contrasted with all the other examples, in which the Mohr-Coulomb criterion was adopted.

*Reinforcing steel*
$E_s =$ 210000 N/mm$^2$
$f_{sy} = 440$ (528) N/mm$^2$
For the dynamic analysis, 10% damping was specified for the two frequencies $\omega_1 = 125$ Rad/s and $\omega_2 = 1250$ Rad/s. This is equivalent to the Rayleigh damping parameters $\alpha = 22.7$ and $\beta = 0.000145$.

### 8.2.3 Gravity load data

For determining the dead weight of the tunnel, the weight of the concrete was taken as

2400 kg/m$^3$, which corresponds to a density input value of $2.4 \times 10^{-9}$ Nsec$^2$/mm$^4$ and should be combined with a gravity acceleration of 9810 mm/sec$^2$.
For the soil weight, a 2 m layer of sand weighing 1900 kg/m$^3$ was assumed, and a 10 m depth of water weighing 1000 kg/m$^3$ was included. Soil and water exert a pressure of 0.1353 N/mm on a 1 mm wide section of the tunnel.

### 8.2.4 Gas explosion load data

The determination of dynamic pressure loads generated by internal gas explosions is not easy, because there are few useful experimental data available. The TNO Prins Maurits Laboratory, in cooperation with other organizations in Belgium and The Netherlands, conducted a series of tests on an experimental tunnel near Beveren, Belgium, with internal cross-sectional dimensions of 1.8 m by 1.8 m and a length of 27 m. From these experiments it was possible to identify the following characteristics of a pressure-time history due to an internal gas explosion (Fig. 8.4a):

1. For all practical purposes the shock front is vertical, i.e. the pressure rise from ambient to peak pressure is instantaneous. The measured peak pressure was about 25 bar.
2. The peak pressure decreases parabolically to an overpressure plateau.
3. The overpressure remains approximately constant at the value of 6 to 7 bar. This value can be computed from the gas-air mixture, considering the energy released

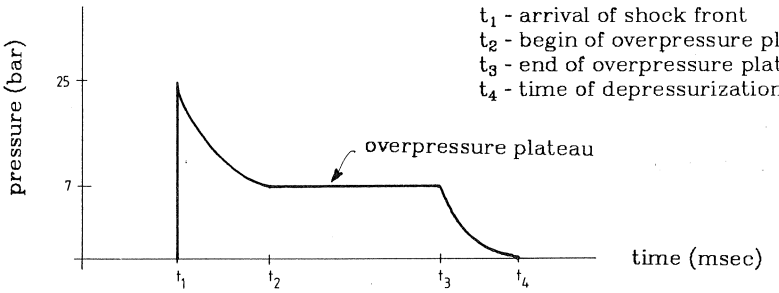


a. Generic pressure time history

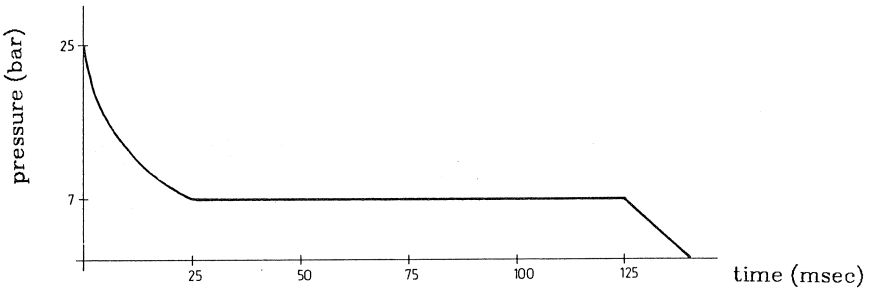


b. Pressure time history used in this analysis

Fig. 8.4. Pressure time history for an internal gas explosion.

during the chemical reaction. The length of the plateau is a function of the time needed to release the overpressure.
4. Once the depressurization of the tunnel starts, the decrease in overpressure again conforms to an approximately parabolic curve.

The scaling of these experimental pressures for tunnels of different dimensions is not straightforward. Concerning the tunnel cross-sectional dimensions it can be argued that the energy released per unit volume is invariant; therefore both the peak pressure and the plateau pressure are approximately independent of the cross-sectional area, assuming the entire cross-section to be filled with combustible gas. Since the shock wave travels at a speed of about 2000 m/s it is logical to assume that the length of the pressure plateau is equal to the time it takes the wave to travel from the point of observation to the nearest tunnel exit and back. Only then can the depressurization start. The experiments revealed the inexplicable phenomenon that also the time from peak pressure (arrival of the shock front) to overpressure plateau is approximately proportional to the distance travelled by the shock front.
In addition to this information, the following assumptions were made in order to arrive at a pressure-time history to be used in this analysis:
1. The Vlake Tunnel of 327 m length was entirely filled with gas.
2. The detonation commences at the centre of the tunnel.
3. The tunnel section to be analyzed is located at the quarter point, i.e. at a distance of about 80 m from the tunnel exit.
4. The shock wave velocity is 2000 m/s.
5. The velocity of the depressurization wave is half that value, i.e. 1000 m/s, because depressurization is associated with fluid flow, a considerably slower process.

Combining this information, one can arrive at the approximate pressure history shown in Fig. 8.4b, which was used in the analysis.
It is to be noted that the peak pressure of 25 bar equals 2.5 N/mm$^2$. Even the pressure plateau of 7 bar or 0.7 N/mm$^2$, applied for the duration of 0.1 s, represents a formidable load which a conventionally reinforced structure is unlikely to survive without severe damage.
Fig. 8.5 summarizes the three load cases relevant to this analysis.

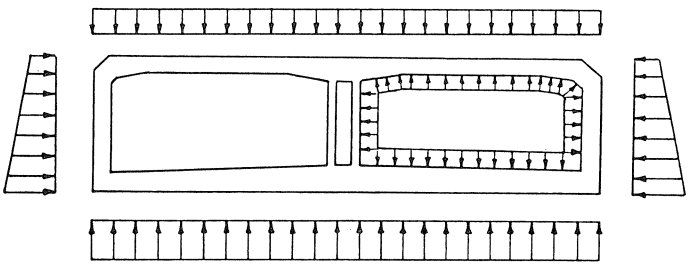

Fig. 8.5. Tunnel load cases: (1) dead weight, (2) sand and water, and (3) internal pressure.

## 8.3 *Modelling of structure and model verification*

As already mentioned in the introduction, the finite element model was developed in stages, and at each stage steps were taken to verify the correctness of the results and to build up confidence in the results of the final dynamic analysis.

### 8.3.1 Frame model analysis

As a first step, a frame model of the entire tunnel section was developed (Fig. 8.6): 34 ordinary beam elements were used to model the section, and rigid links took account of the finite joint sizes. A simple linear static analysis of this model was performed for the load cases: (1) soil and water pressure, and (2) internal pressure. Qualitative bending moments are shown in Fig. 8.7 and indicate that the moment distribution in the tunnel roof is very similar in both cases. Thus, it is possible to model only one quarter of the entire roof slab by finite elements and to apply boundary conditions which are applicable to both load cases.

### 8.3.2 Linear-elastic static analysis of finite element model

The finite element model used for this analysis and the subsequent analyses is presented in Fig. 8.8. For comparison with the frame element model results, 45 eight-noded plane stress elements of the type CQ16 M were used for the concrete, and the reinforcement was modelled by 34 bar elements as shown. The model represents a 1500 mm wide segment of the tunnel. Third-order integration was used for both plane stress and bar elements. The model has 172 nodes with a total of 344 potential degrees of freedom (Fig. 8.9).

This analysis was performed primarily for calibration purposes to obtain linear elastic

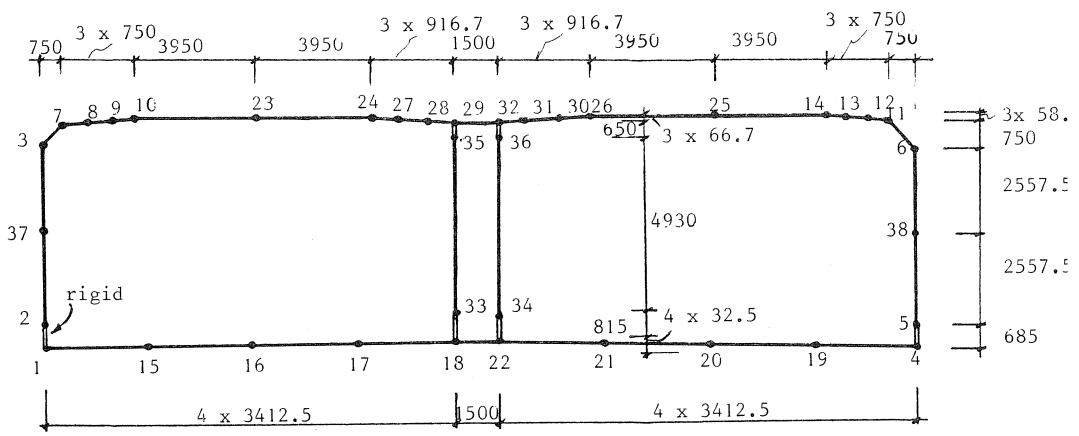


Fig. 8.6. Frame element model (dimensions in mm).

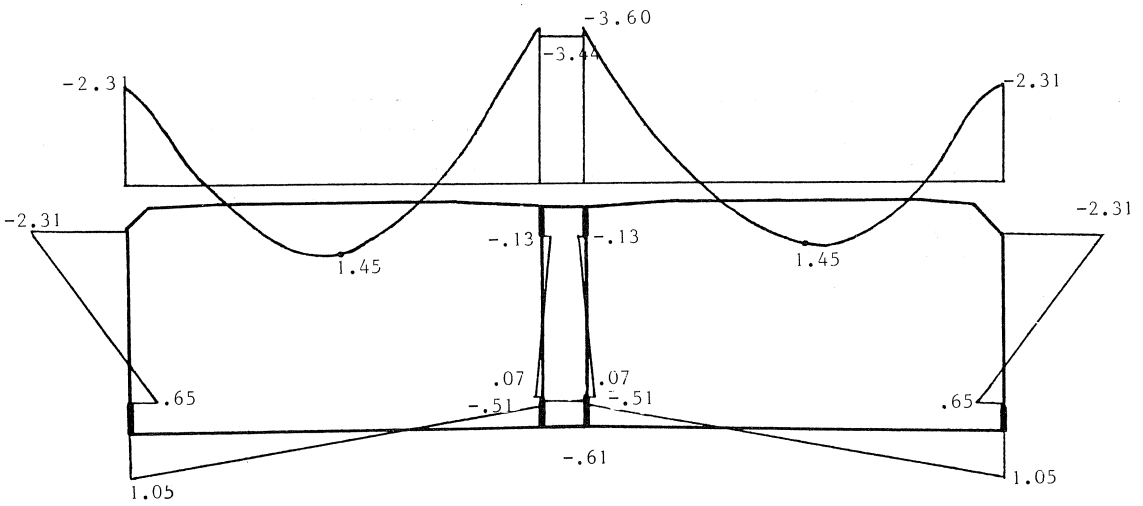


a. Bending moments for sand and water

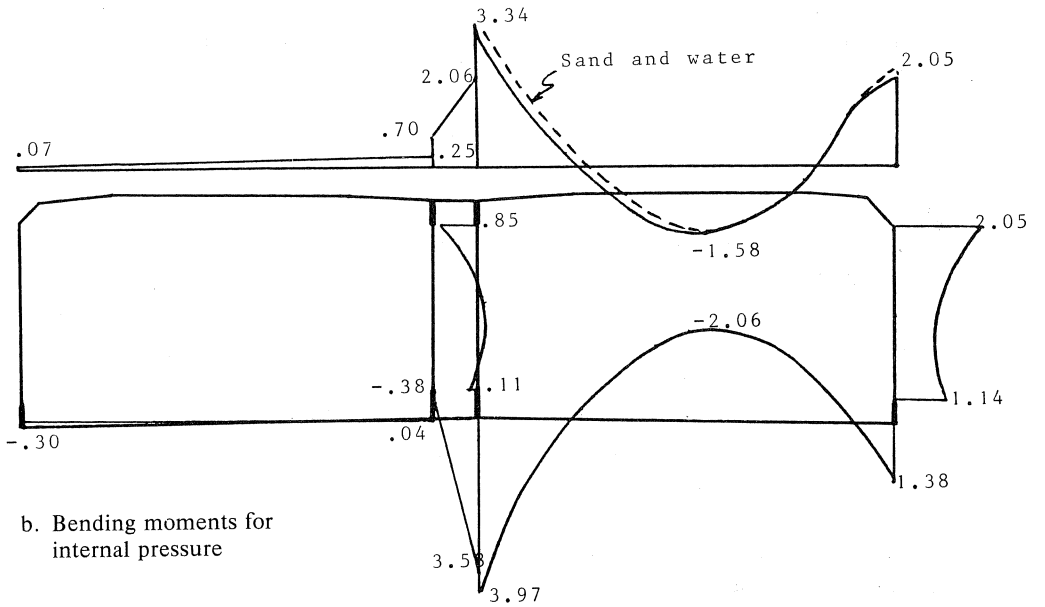


b. Bending moments for internal pressure

Fig. 8.7. Bending moments obtained with frame element model.

results comparable with those obtained with the frame model. Difference in the results were due to the following factors:

1. The right-hand face of the finite element model was fixed against rotation, whereas the frame analysis indicated that due to the flexibility of the outer walls the points of maximum positive moment (and the point of zero rotation) is shifted a certain amount towards those walls. To correct the finite element model, the midspan rotation of the frame model was prescribed as a rotation of the right-hand face of the finite element model.

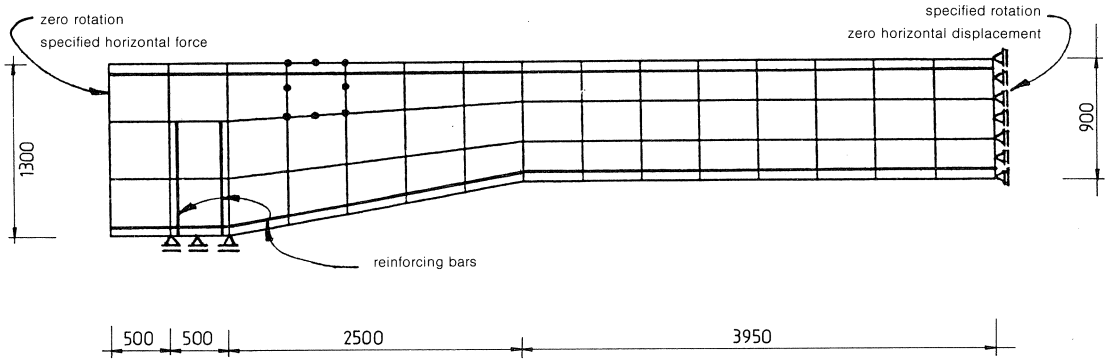


Fig. 8.8. Finite element model of tunnel roof (dimensions in mm).

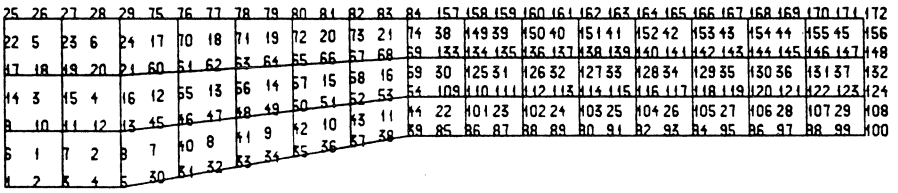

Fig. 8.9. Nodal point and element numbers.

2. The axial deformations of the vertical walls were included in the frame element model but not in the finite element model.
3. The effect of steel reinforcement on the roof stiffness was explicitly accounted for in the finite element model, whereas in the frame element model only gross moments of inertia were used.
4. The representation of the haunched segment of the tunnel roof by a series of prismatic beams introduces a considerable error, which can be reduced by increasing the number of beam elements.

On taking due account of these four factors, both moments and displacements obtained by the two models agreed to within 15%.

### 8.3.3 Nonlinear static finite element analysis

This preliminary analysis was performed because experimental data were available for comparison which could serve as an additional check of the finite element model. In the experiment, the 1 : 5 scale model of a 1.5 m wide tunnel section was subjected to a complex loading history. The service loading pattern to be simulated is shown in Fig. 8.10, and the experimental set-up in Fig. 8.11. The load level was increased in stages, in multiples of the service load level. At each stage, the load would be held constant for about 40 minutes to permit creep deformations to take place. Thereafter, the deforma-

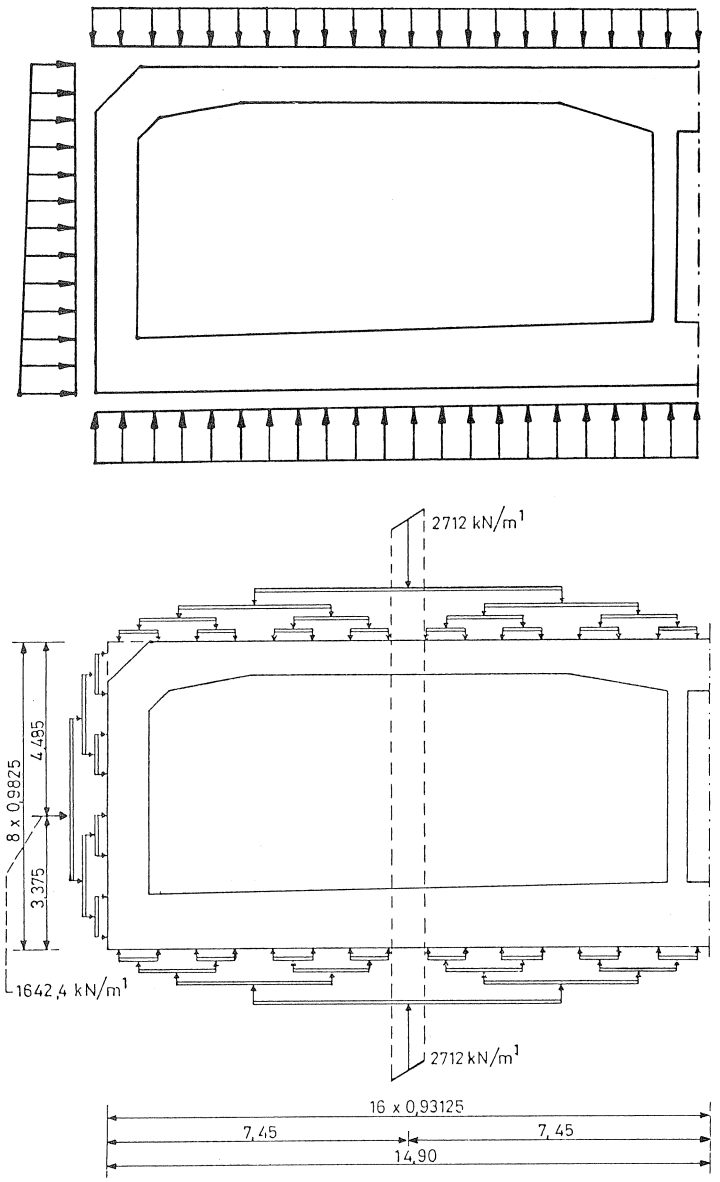


Fig. 8.10. Service loading pattern simulated in experiment.

tions were held constant for another 80 minutes for taking the measurements. After this, the load would be reduced by about 90% and increased again to reach the previous displacement level. 10000 load cycles were thus applied at 4 seconds per cycle. The five load levels equal to 1.0, 1.2, 1.4, 1.6 and 1.7 times the service load can be seen in Fig. 8.12. At the last load level, only 8700 load-cycles were applied because the specimen showed signs of failure.

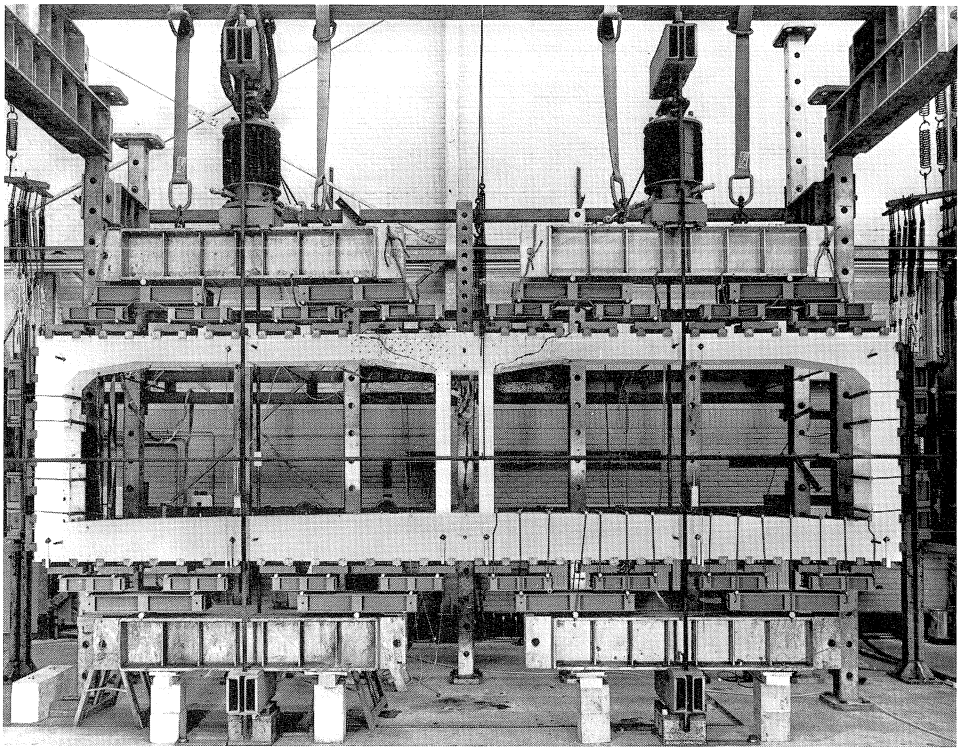

Fig. 8.11. Experimental set-up.

Before making a meaningful comparison between analytical and experimental results, a number of factors had to be taken into account. First, in the experiment, the displacement $\delta$ referred to in Fig. 8.12 constitute the sum of roof and floor slab displacements. From the linear elastic analysis of the frame element model it was found that the bottom slab contributes 17% to $\delta$, while the axial deformation of the vertical wall and the rotation of the fixed end contribute another 11%. Thus only 72% of the experimental displacements should be compared with the analytical results.

The boundary conditions for the finite element analysis were determined from the results of a linear elastic analysis of the frame element model for 1.0 times the service load. These were as follows:

1. The right-hand face of the model was fixed against horizontal displacements.
2. The right-hand face was subjected to a rotation of 0.000158 by prescribing appropriate horizontal displacements for the affected nodes.
3. The left-hand face was fixed against rotation but free to move horizontally to prevent unrealistic arch action in the roof slab. This condition was implemented by use of the tying option.
4. An axial compressive force of 818 kN was applied to the left-hand face, this force being caused by the horizontal pressure applied to the outside walls.

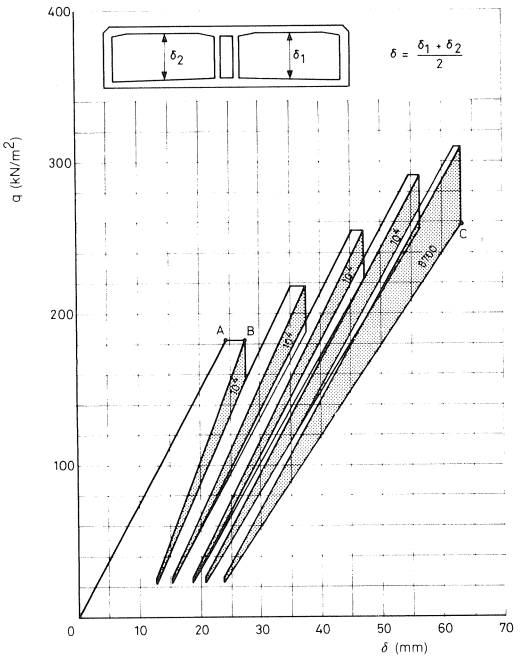


Fig. 8.12. Load history in the experiment.

In the analysis, cracking started at 0.5 times the service load. After that, load increments of 0.05 were applied up to 2.5 times the service load. Up to 15 modified Newton iterations were allowed to give convergence of the results to an energy tolerance of 0.001. Experimental and analytical load-deflection information is given in Fig. 8.13. Most striking in this comparison is the large discrepancy in stiffness between theory and experiment. A number of factors are responsible for this:

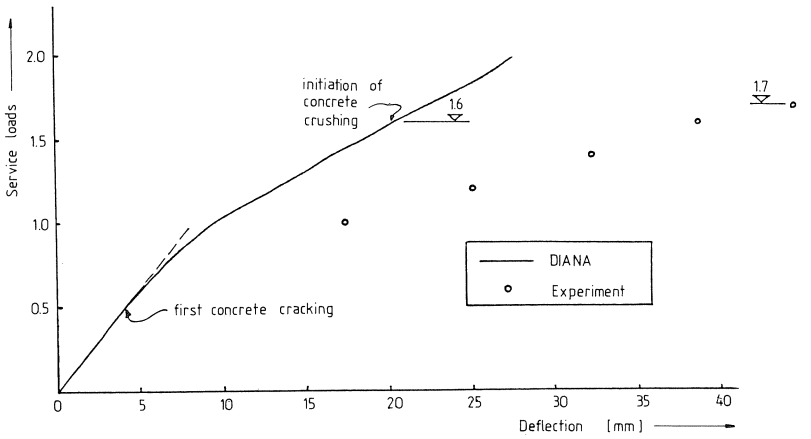


Fig. 8.13. Experimental and analytical load-deflection information.

1. The experimental data points were obtained from Fig. 8.12, adjusted with the 0.72 factor mentioned earlier. This diagram is a rather incomplete documentation of load-deflection behaviour, as it does not indicate, for example, the change in stiffness due to concrete cracking.
2. The large number of load cycles in the experiment caused damage, which could not be reproduced by the monotonic load application used in the analysis.
3. The analysis did not attempt to reproduce the creep deformations that took place in the experiment.
4. It can be expected that the moment redistribution due to cracking affects the results in a way that was difficult to reproduce analytically, since the boundary conditions were based on the moment distributions of the cracked structure.
5. From the documentation of the experiment it was difficult to determine to what degree of accuracy the laws of similitude have been satisfied.

Although the stiffness of the tunnel roof was apparently not simulated too well in the analysis, both the extent and nature of cracking and the failure load level were reproduced rather well. Figs. 8.14 and 8.15 show comparisons between experimental and analytical crack patterns at 1.0 and 1.7 times the service load respectively. The shear cracks observed in the experiment are clearly visible in the analysis results as well. It is interesting to note the horizontal splitting cracks over the support, caused by the large horizontal thrust. Failure was eventually coupled with crushing in the highly stressed

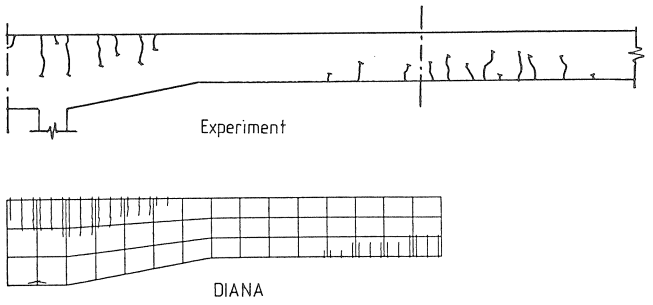


Fig. 8.14. Cracking at 1.0 times the service load.

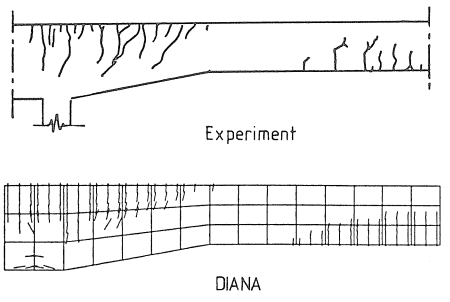


Fig. 8.15. Cracking at 1.7 times the service load.

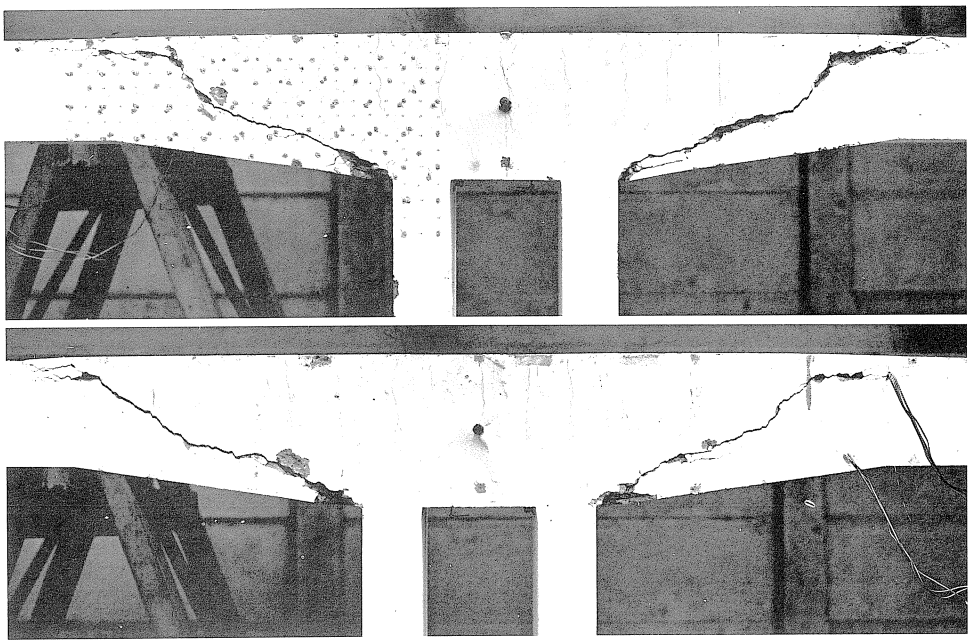

Fig. 8.16. View of the test specimen after failure.

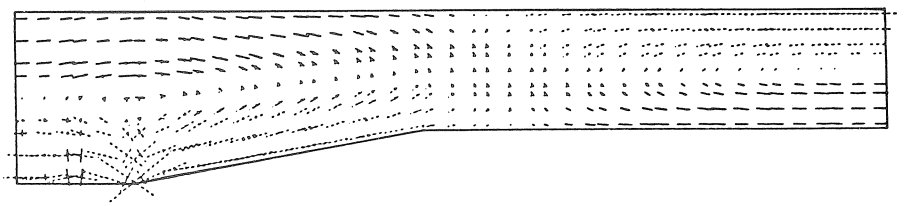

Fig. 8.17. Principal stresses at 1.0 times the service load.

corner, as can be seen both in Fig. 8.16, which is a photo of the test specimen after failure, and in Fig. 8.17, which illustrates the severe stress concentration at the corner point near the support.
From this analysis it can be concluded that DIANA is capable of simulating the response of this structure through the various cracking stages up to failure. Both the program and the model can therefore be expected to provide useful results in a dynamic analysis.

### 8.3.4 Eigenvalue analysis

In order to compute the mode shapes and frequencies of the finite element model of Fig. 8.6, it was necessary to model the inertia of the soil and water over the tunnel roof. Rather than undertaking an elaborate structure-fluid interaction analysis, it was

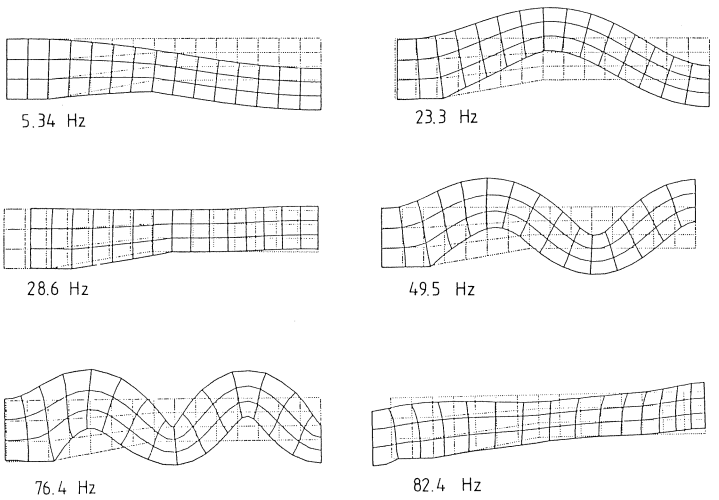


Fig. 8.18. First six modes and frequencies of finite element model.

decided to simply account for the mass of the 2 m soil and 10 m of water by concentrating it as lumped masses at the nodes along the upper boundary of the model. For the response of the structure to the initial shock of the blast load this approximation was felt to be permissible. The first six computed frequencies and mode shapes are summarized in Fig. 8.18.

For a "manual" check of the fundamental frequency we may assume $L = 6910$ mm (span between the inflection points), $I = 9.1 \times 10^{10}$ mm$^4$, $E = 22000$ N/mm$^2$ $= 22 \times 10^6$ kg/s$^2$mm, and $m = 3.24 + 20.70 = 23.94$ kg/mm; we thus obtain:

$$\omega = \pi^2 \sqrt{\frac{EI}{mL^4}} = 59.8 \text{ Rad/s} = 9.5 \text{ Hz}$$

The difference between this value and the first frequency computed for the finite element model can be attributed to the effect of the haunches.

### 8.3.5 Nonlinear time history analysis of simplified finite element model

Before performing an expensive nonlinear dynamic analysis with the full finite element model it was decided to perform trial analyses using the grossly simplified finite element model of Fig. 8.19. There were a number of reasons for this:

1. This is a relatively inexpensive way for the novice user to familiarize himself with the program's dynamic analysis options and to set-up the command files for shock analysis initialization and time step integration.
2. In this specific case, the small test problem served to identify a few programming errors and to prompt their correction.

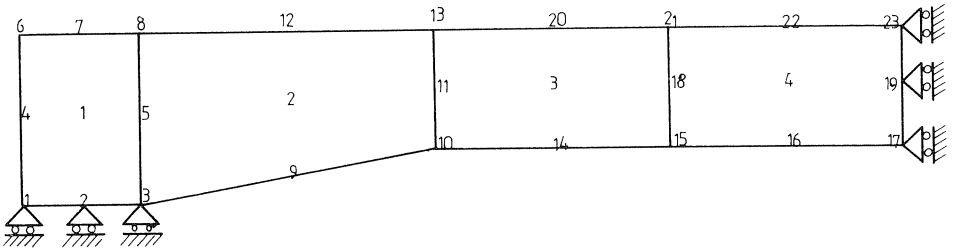


Fig. 8.19. Grossly simplified finite element model.

3. The model, by exhibiting modes and frequencies surprisingly close to those of the large finite element model, was capable of giving a first impression of the structure's dynamic response.
4. Currently, the program has the limitation of being able to combine static and dynamic loads. For this reason, the simplified model was used to assess the impact of applying all gravity loads dynamically.

Fig. 8.20 depicts the time history of the midspan deflection due to a sudden application of all gravity loads. As can be clearly seen, the deflection oscillates around the value of 8.9 mm, which is somewhat larger than the computed static deflection of 6.8 mm,

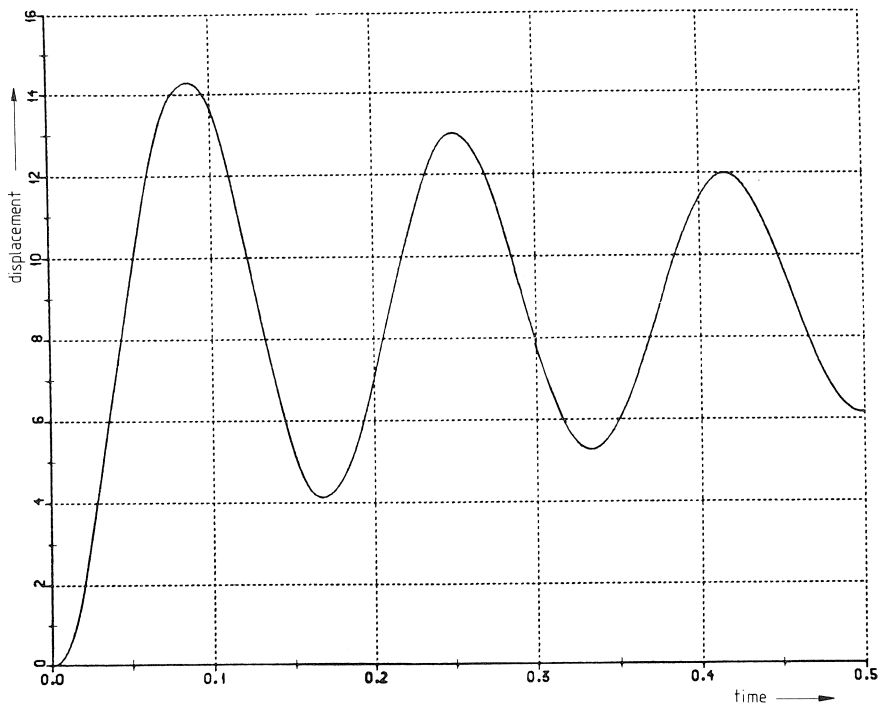


Fig. 8.20. Midspan deflection of simplified model due to dynamically applied gravity loads.

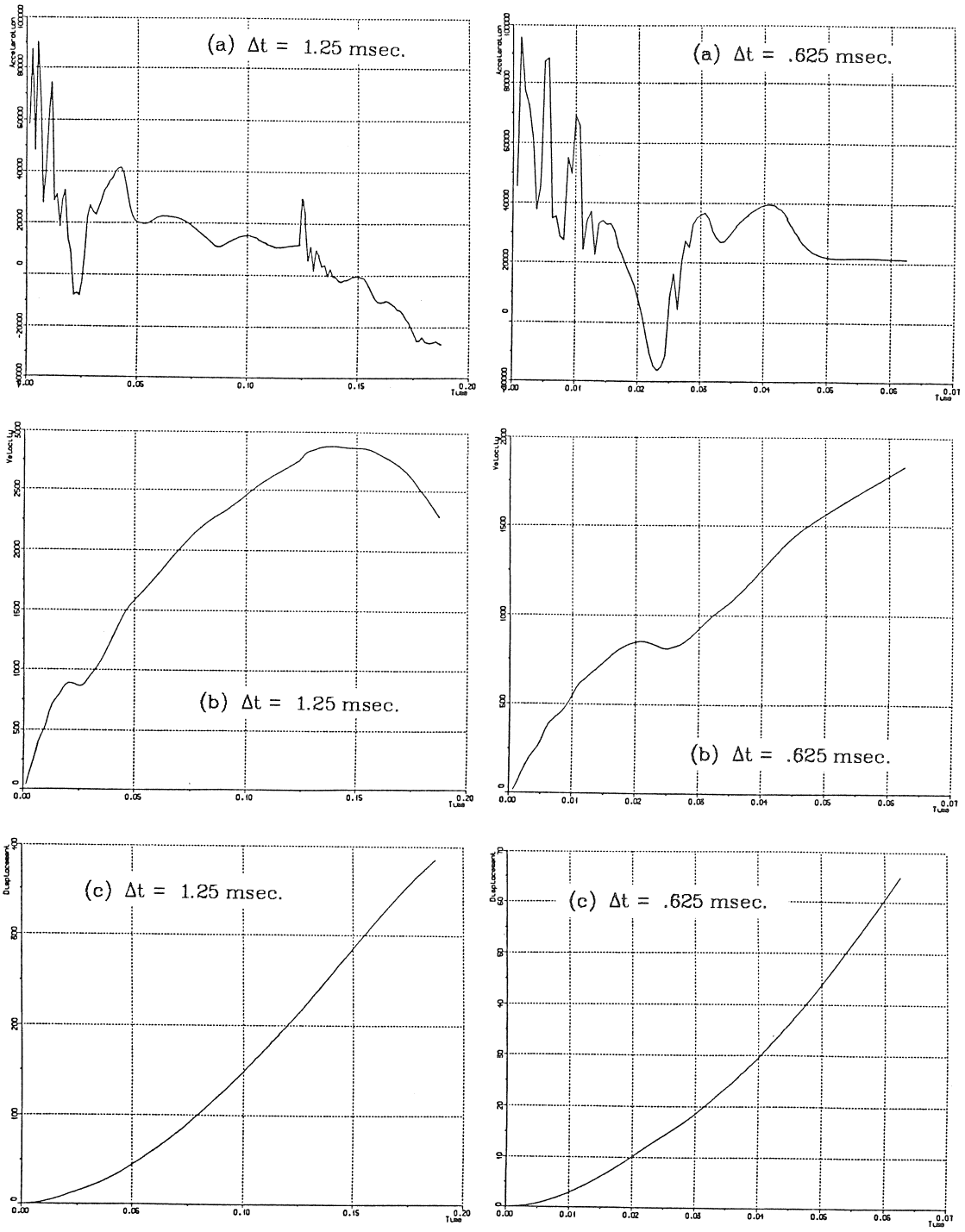


Fig. 8.21. Time history response of the tunnel roof at midspan: (a) acceleration in mm/s$^2$, (b) velocity in mm/s, (c) displacement in mm. Note that the scales for the results with different time steps are not the same.

because the dynamic effect of the load application causes more severe cracking. Also the apparent fundamental period of about 0.36 s is much larger than the 0.15 s computed for the uncracked linear elastic model.
Concerning the program's limitations regarding static and dynamic load combinations, it was felt that the internal pressure load is so much larger than the gravity loads that all loads could well be applied dynamically at the same time.

## 8.4 *Nonlinear time history analysis of finite element model*

All the analyses so far described now had been performed as preparatory studies for the "final" run, namely the time history analysis of the finite element model of Fig. 8.8 for the pressure time history of Fig. 8.4. Prior to this analysis the following model modifications were introduced.

1. The plane stress elements CQ16M were replaced by the plane strain elements CQ16E.
2. In compliance with the plane strain analysis convention, the model thickness was changed from 1500 mm to 1 mm. All masses, loads, etc. were adjusted accordingly.
3. In the longitudinal direction of the tunnel, reinforcing bars were assumed with areas 20% of the transverse steel areas.

The final run involved 150 time steps of $\Delta t = 1.25$ ms. To evaluate the effect of the time step size, a second run with 100 time steps $\Delta t = 0.625$ ms was carried out. The acceleration, velocity and displacement time histories of the roof midspan section are plotted in Fig. 8.21, together with the applied pressure history for reference. From these and the other results, the following observations were made:

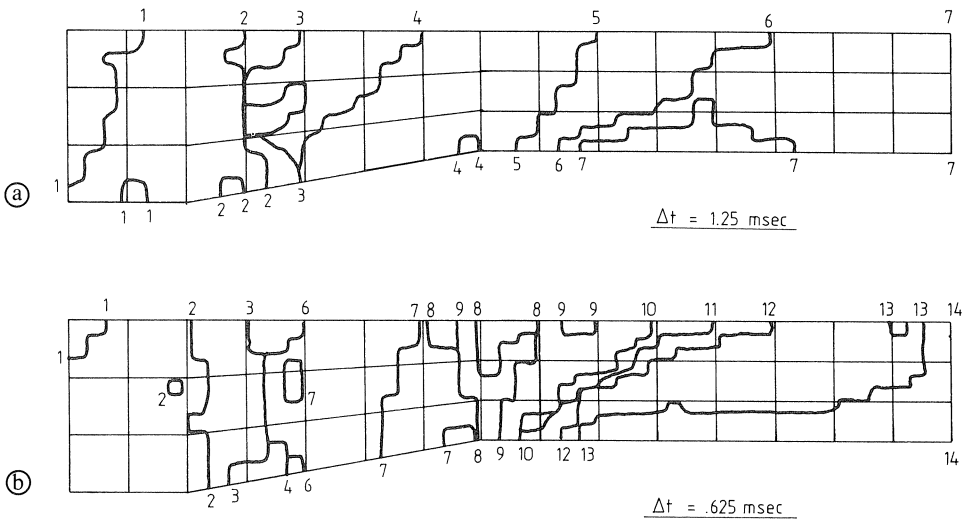


Fig. 8.22. Propagation of the concrete cracking wave front, (a) for the analysis with $\Delta t = 1.25$ ms, and (b) for the analysis with $\Delta t = 0.625$ ms.

1. The first impact experienced by the structure is the axial load applied at the left-hand boundary. This tensile impact wave propagated to the right causing cracking of the concrete at all integration points along its path. Fig. 8.22a shows this "cracking wave front" after the first seven time steps, after which it arrived at the right-hand boundary, long before the roof had any time to respond in bending to the upward pressure. The wave speed is approximately 6450/0.00875 mm/s = 737 m/s.
2. The reduction of the integration time step to 0.625 ms, did not affect the results very much, as can be seen by comparing Figs. 8.22a and b. Only the vertical midspan accelerations showed some changes.
3. Up to 111 integration points cracked during time step 7, yet the solution converged almost at each time step within at least 10 iterations to the specified energy tolerance of 0.001.
4. The first reinforcing bar integration point started to yield in the fourth time step. The concrete cracking wave is followed by a somewhat slower steel yield wave, which reached the midspan section after 22 steps. Fig. 8.23 shows the total number of steel integration points that yield at a certain time. As the total number of steel integration points is 96, this diagram signifies that for the entire duration of the pressure plateau a little less than half of the steel integration points yielded at any point in time.
5. The steel stresses in the two vertical reinforcing bars, which tie the roof slab into the vertical walls are plotted as a function of time in Fig. 8.24. It is interesting to observe that for a while these two bars provide a fixed end moment, but as the vertical pressure tends to lift the roof off its supports, also the tensile stress in the left bar builds up. At time step 150, the steel strain in the right bar has reached the value 0.022. The largest steel strain at this time was computed for the bottom steel over the support (within concrete element 7, see Fig. 8.8) and was equal to 0.083. The top reinforcing bar at midspan has undergone a strain of 0.024 at this time.
6. The concrete stresses were not critical at any time of the analysis. The combination of flexure with axial tension compelled the reinforcing steel to resist most of the load.

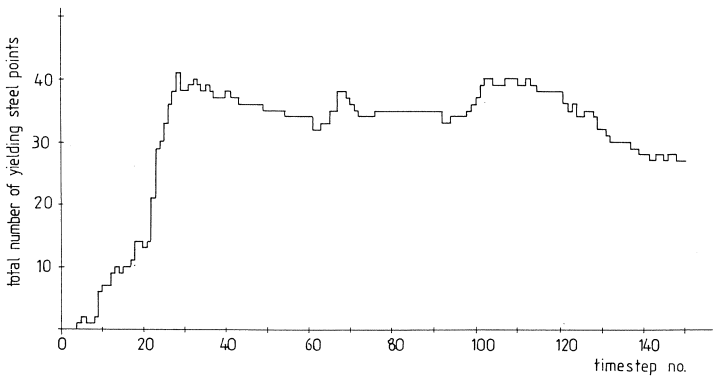


Fig. 8.23. Total number of yielding steel points.

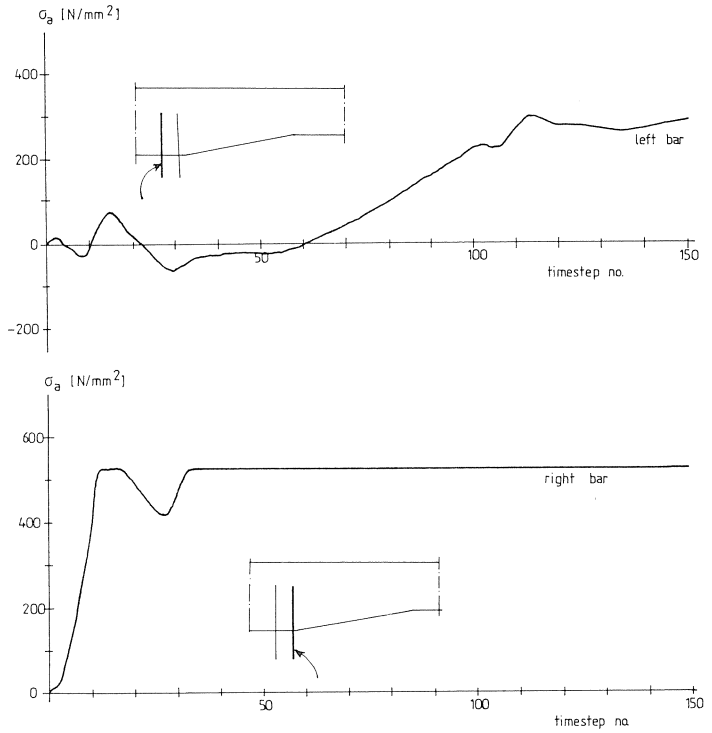


Fig. 8.24. Time histories of stresses in vertical reinforcing bars: (a) left bar, and (b) right bar.

7. The results presented tend to point to the conclusion that the tunnel roof is not likely to survive a gas explosion load of the kind stipulated in Fig. 8.4. The weakest detail appears to be the inadequate quantity of vertical reinforcement which cannot prevent the vertical pressure from lifting the roof slab off its supports. Also the plastic hinge both over the support and at midspan in the roof undergo large rotations, causing a midspan deflection of as much as 38.5 cm after 150 time steps, which can only be interpreted as failure.

## 8.5 *Conclusions*

Considering the various objectives of this analysis, the following conclusions can be drawn:

- A conventionally reinforced underwater tunnel is unlikely to survive an internal gas explosion.
- DIANA is a powerful tool to provide rational solutions for complex nonlinear dynamic analysis problems.
- Such an analysis is a very difficult task, which may take an experienced analyst at least one full month or more and consumes considerable computer resources. These man-hours and computer expenses are needed primarily for the step-by-step development of the finite element model and its verification.

## 9 Concluding remarks

In addition to the concluding remarks made at the end of each example, some general conclusions can be drawn.

A non-linear finite element analysis may be required when complex problems must be solved for which loadings, boundary conditions and geometrical factors cannot be dealt with by using existing analytical procedures. In general a choice has to be made as to whether a model study or a non-linear analysis should be carried out. This choice will largely be influenced by the reliability of the results obtained by either of the methods. As demonstrated, the numerical tool can largely increase the structural insight, and can serve as a research tool or as a means for improving model codes as well. Yet, in general, an analysis is a very difficult task and should be carried out only by an experienced analyst who is familiar with the material models adopted.

The use of a finite element package in its simplest form (i.e. linear-elastic), may already give considerable insight into structural behaviour. In several of the examples, the structural mechanism remained unchanged, irrespective of the development of cracks, and a sound and solid structural design can then be based on a partial analysis. The difficulty is that these cases are not easily predictable, so that always some investigations have to be made. In the more complicated analyses, redistributions or changes of the structural mechanism were observed (e.g. the beam-column connection, example 3, and the analysis of the tunnel section, example 4), and consequently the analysis required more effort.

The performance of the programme seemed rather problem-dependent, which of course puts some restrictions on its predictive powers. In many cases, the lack of predictive power seemed to be induced by a misunderstanding of the material behaviour (of the material concrete), although also in some cases the way in which the structure is divided into "basic building blocks", may be open to some debate.

Table 9.1 CPU times (in seconds) for some of the examples ($P_t$ is the fracture load)

| CPU times | | |
|---|---|---|
| example | $0.75P_t$ | $P_t$ |
| 1 | 30000 | 86000 |
| 2a | 11000 | 29900 |
| 2b | 13000 | 58200 |
| 3 | 9800 | 34200 |
| 5a | 580 | 1500 |
| 5b | 2160 | 29000 |

How far a computation should be carried through is also dependent on the type of problem. When only information concerning the service loads is needed, a tremendous reduction in computation time is obtained. When fracture conditions are also to be investigated, the effort increases considerably, as indicated in Table 9.1 for several of the examples. For an analysis up to 70% of the fracture load, only roughly 30% of the computer time is needed as compared with the fracture analysis.

It should be mentioned that the above times will decrease, depending on developments in computer technology (hardware and software). However, effort needed for interpreting the computational results will remain the same. Some further comments are called for. In example 5b, only 8% of the CPU time needed for analysing the fracture conditions was devoted to analysing the response of the panel on three supports up to 75% of its failure load. In this particular example, the panel had hardly cracked at this level, and by slightly increasing the load, a pronounced plateau was observed in the load-displacement diagram (see Fig. 5.15). The emergence of this plateau coincided with the development of a pronounced shear crack in the panel. The reason for mentioning this example in this place is that in every analysis it is necessary to look out for such structural response. The effort expended should be weighed against the information needed. Safety considerations and structural aspects should be taken into account. Nevertheless, in several of the examples, especially those where no large changes of the structural mechanism occur after 75% of the fracture load, a partial analysis may be sufficient. In those cases, the structural behaviour can be simulated quite accurately with the numerical tool. If more information is needed, the performance of the program is rather problem-dependent, and it seems that lack of knowledge of material properties (of the concrete) is the main source for the observed discrepancies. However, the current (general) structure of the DIANA programme forms a solid basis for future improvements and extensions.

## 10 Notation

The following symbols are used in this report:

| | |
|---|---|
| $c$ | cohesion |
| $E_c$ | Young's modulus of the concrete |
| $E_s$ | Young's modulus of the reinforcing steel |
| $f_{cc}$ | concrete compressive strength |
| $f_{ct}$ | concrete tensile strength |
| $f_{py}$ | yield stress of prestressing steel |
| $f_{sy}$ | yield stress of reinforcing steel |
| $G_f$ | fracture energy |
| $h$ | crack band width |
| $S^r$ | slip modulus, radial direction |
| $S^z$ | slip modulus, axial direction |
| $w$ | crack width |
| $\beta$ | shear retention factor |
| $\gamma$ | shear strain |
| $\varepsilon_{ct}$ | $f_{ct}/E_c$ |
| $\varepsilon_s$ | $f_{sy}/E_s$ |
| $\varepsilon_u$ | ultimate tensile strain ($G_f$-concept) |
| $\varepsilon_{us}$ | ultimate tensile strain (tension stiffening concept) |
| $\varphi$ | friction coefficient |

| | |
|---|---|
| $\varrho$ | density |
| $\sigma_i$ | principal stress ($i = 1,2,3$) |
| $\tau$ | shear stress |
| $\tau_{zu}$ | maximum bond stress |
| $\nu$ | Poisson's ratio |

## 11 References


AMMANN, W., M. MÜHLEMATTER and H. BACHMANN (1982), Versuche an Stahlbeton- und Spannbetonbalken unter stossartiger Beanspruchung. Teil 2: Konzeption und Durchführung der Balkenversuche, Zusammenfassung der Versuchsresultate, Bericht Nr. 7709-2, Institut für Baustatik und Konstruktion ETH Zürich.

AMMANN, W., M. MÜHLEMATTER and H. BACHMANN (1982), Versuchen an Stahlbeton- und Spannbetonbalken unter stossartiger Beanspruchung. Teil 3: Versuchsresultate der Balken P1, P2 und B1 bis B8, Bericht Nr. 7709-3, Institut für Baustatik und Konstruktion ETH Zürich.

AMMANN, W., M. MÜHLEMATTER and H. BACHMANN (1981), Experimental and Numerical Investigations of Reinforced and Prestressed Concrete Beams for Shock Loading, Bericht Nr. 116, Institut für Baustatik und Konstruktion ETH Zürich.

ANDERBERG, Y. and S. THELANDERSSON (1976), Stress and Deformation Characteristics of Concrete at High Temperatures, Part 2: Experimental Investigation and Material Behaviour Model, Lund Institute of Technology, Bulletin 54, Sweden 1976.

ANDERBERG, Y. and N. E. FORSEN (1982), Publication No. 1, Nordic Concrete Research, Oslo, Dec. 1982.

BATHE, K.-J. (1982), Finite Element Procedures in Engineering Analysis, Prentice-Hall, Inc., Englewood Cliffs, New Jersey 07632.

BELYTSCHKO, T. and T. J. R. HUGHES (1983), Computational Methods for Transient Analysis, Vol. 1 in Computational Methods in Mechanics, North-Holland, Amsterdam-New York-Oxford.

CEB (1982), Comité Euro-International du Béton, Design of Concrete Structures for Fire Resistance, Bulletin d'information 145, Paris.

CUR (1969), Loading tests on a full-size suspended beam and a model of this beam for a Metro Viaduct at Rotterdam, Report No. 40, Netherlands Committee for Concrete Research (CUR).

CUR (1982), Concrete under Impact Loading: Tensile Strength and Bond, Report No. 106, Netherlands Committee for Concrete Research (in Dutch).

DE BORST, R., G. M. A. KUSTERS, P. NAUTA and F. C. DE WITTE (1983), DIANA - a comprehensive but flexible finite element system, Finite Element Systems Handbook, 3rd edition, Springer Verlag, Berlin, West Germany.

DE BORST, R. (1986), Non-linear Analysis of Frictional Materials, Dissertation, Delft University of Technology, Delft, The Netherlands.

DE GROOT, A. K., G. M. A. KUSTERS and TH. MONNIER (1981), Numerical Modelling of Bond-Slip Behaviour, HERON, Vol. 26, Special Publication on Concrete Mechanics, No. 1b.

GROOTENBOER, H. J. (1979), Finite element analysis of two-dimensional reinforced concrete structures, taking account of non-linear physical behaviour and the development of discrete cracks, Dissertation, Delft University of Technology, Delft, The Netherlands.

GROOTENBOER, H. J., S. F. C. H. LEIJTEN and J. BLAAUWENDRAAD (1981), Numerical models for reinforced concrete structures in plane stress, HERON, Vol. 26, Special Publication on Concrete Mechanics, No. 1c.

KHOURY, G. A., B. N. GRAINGER and P. J. E. SULLIVAN (1985), Strain of Concrete during First Heating to 600° under load, Magazine of Concrete Research, Vol. 37, No. 133, pp. 195–215.

KRIZ, L. B. and C. H. RATHS (1965), Connections in Precast Concrete Structures - Strength of Corbels, Journal of the Prestressed Concrete Institute, Vol. 10, No. 1, pp. 16–61.

LEONHARDT, F. and R. WALTHER (1966), Wandartige Träger, Deutscher Ausschuss für Stahlbeton, Heft 178, Berlin.

MULLER, F. P., E. KEINTZEL, E. and H. CHARLIER (1983), Dynamische Probleme im Stahlbetonbau. Teil 1: Der Baustoff Stahlbeton under dynamischer Beanspruchung, Deutscher Ausschuss für Stahlbeton, Heft 342, Berlin.

MULLER, T. K. (1984), Design of a storage tank (type C-IS), Graduate thesis, Part I, Delft University of Technology, Delft, The Netherlands (in Dutch).

MULLER, T. K. (1985), Concrete tanks, subjected to fire load, Graduate thesis, Part II, Delft University of Technology, Delft, The Netherlands (in Dutch).

NELISSEN, L. J. M. (1972), Biaxial Testing of Normal Concrete, HERON, Vol. 18, No. 1.

NIEDENHOFF, H. (1963), Untersuchungen über das Tragverhalten von Konsolen und kurzen Kragarmen, Dissertation, Technische Hochschule Karlsruhe.

REICH, E. (1983), Höhe Konsolen, modellstatische Untersuchungen, Bemessungsvorschlag, Werner Verlag, Düsseldorf.

REINHARDT, H. W. (1984), Fracture Mechanics of an Elastic Softening Material like Concrete, HERON, Vol. 29, No. 2.

ROTS, J. G., P. NAUTA, G. M. A. KUSTERS and J. BLAAUWENDRAAD (1985), Smeared Crack Approach and Fracture Localization in Concrete, HERON, Vol. 30, No. 1.

ROTS, J. G. (1985), Bond-slip Simulations using Smeared Cracks and/or Interface Elements, Research Report, Delft University of Technology, Dept. of Civil Engineering.

STROBRAND, J. and J. J. KOLPA (1983), The Behaviour of Reinforced Concrete Column-to-Beam Joints - Part 1: Corner Joints Subjected to Negative Moments, Research Report 5-83-9, Delft University of Technology, Dept. of Civil Engineering.

TNO (1976), Onderzoek aan een model van een tunneldoorsnede (Research into the behaviour of a model of a tunnel section), Research report, IBBC-TNO, No. B-76-197/04.4.1080, June 1976 (in Dutch).

VAN MIER, J. G. M. (1984), Strain-Softening of Concrete under Multiaxial Loading Conditions, Dissertation, Eindhoven University of Technology, Eindhoven, The Netherlands.

VAN DER VEEN, C. and J. BLAAUWENDRAAD (1983), Dynamic elasto-plastic model for reinforced concrete members, HERON, Vol. 28, No. 1.

VERMEER, P. and R. DE BORST (1984), Non-associated Plasticity for Soils, Concrete and Rock, HERON, Vol. 29, No. 3.

WALTER, J. P. (1983), Calculations of Storage Vessels under Extreme Temperature Conditions - Fire and Spill, Proceedings of the Second Int. Conf. on Cryogenic Concrete, October 1983, Amsterdam, The Netherlands.